Studies of inverse-Compton emission in the Crab Nebula and the BL Lac object 1ES 1959+650

Anna O'Faoláin de Bhróithe

The thesis is submitted to University College Dublin
in fulfilment of the requirements for the degree of
Doctor of Philosophy

UCD School of Physics

Head of School: Prof. P. Dunne

Principal Supervisor: Dr. J. Quinn

Doctoral Studies Panel Membership:
Dr. J. Quinn
Dr. S. McBreen
Prof. P. Duffy

February 2014

Contents

List of Acronyms

AGN Active Galactic Nucleus

BH Black Hole

Dec Declination

EBL Extragalactic Background Light

EAS Extensive Air Shower

EC External Compton

FoV Field of View

HBL High-frequency peaked BL Lac objects, synchrotron emission peak in UV - X-ray

HE High Energy, $E > 1\,\mathrm{MeV}$

H.E.S.S. High Energy Stereoscopic System

IACT Imaging Atmospheric Cherenkov Telescope

IBL Intermediate-frequency peaked BL Lac objects, synchrotron emission peak in optical - UV

IC Inverse Compton

IR Infra-red

ISM Interstellar Medium

LAT The Large Area Telescope on board the *Fermi* satellite

LBL Low-frequency peaked BL Lac objects, synchrotron emission peak in IR - optical

LED Light-Emitting Diode

MAGIC Major Atmospheric Gamma-ray Imaging Cherenkov Telescopes

MJD Modified Julian Day

NDF Number of Degrees of Freedom

NS Neutron Star

NSB Night Sky Background

PCA The Proportional Counter Array on board RXTE

PCU A single Proportional Counter Unit of the PCA

PMT Photomultiplier Tube

PWN Pulsar Wind Nebula

RA Right Ascension

ROI Region of Interest

RXTE *Rossi* X-ray Timing Explorer

SED Spectral Energy Distribution

SN Supernova

SSC Synchrotron Self-Compton

UV Ultra-violet

UVOT The Ultra-violet and Optical Telescope on board the *Swift* satellite

VEGAS VERITAS Gamma-Ray Analysis Suite

VERITAS Very Energetic Radiation Imaging Telescope Array System

VHE Very High Energy, $E > 100\,\mathrm{GeV}$

XRT The X-ray Telescope on board the *Swift* satellite

Abstract

This thesis concerns the study of inverse-Compton emission from two astrophysical sources. The first object, 1ES 1959+650, is a nearby active galactic nucleus. This source was observed as part of the VERITAS blazar monitoring programme in the hopes of detecting it in the midst of a dramatic flaring event. Over the course of these monitoring observations which span four years, a significant detection of the source in its low state was accumulated. The spectral energy distribution of this source was analysed from optical to VHE and was modelled with a synchrotron self-Compton model with an additional external Compton component. The parameters obtained cannot be fully explained by first-order Fermi acceleration at parallel shocks, and instead may suggest particle acceleration at oblique subluminal shocks, or that 1ES 1959+650 may consist of an inhomogeneous jet with a fast inner spine and slower-moving outer cocoon.

The second source is the famous Crab Nebula, for years considered the standard candle of X-ray to VHE γ-ray astronomy. VERITAS observed the Crab Nebula during the recent flare of the high-energy synchrotron component of the source in March 2013. No enhanced VHE emission was detected, but the observations facilitated the calculation of upper limits on any extra VHE spectral component emerging during the flare. A wealth of archival VHE Crab Nebula data also exists, spanning many years. An extended VHE data set of the source from 2000 to 2013 was compiled from Whipple 10 m Telescope and VERITAS observations. This data set was searched for short-term flaring activity, but no evidence of this behaviour was found. A slight decrease in the long-term flux of the nebula was detected in the VERITAS data in 2011. This could possibly be correlated with increasing instability of the aerosol content of the local atmosphere around the VERITAS site.

Declaration

I hereby certify that the submitted work is my own work, was completed while registered as a candidate for the degree stated on the Title Page, and I have not obtained a degree elsewhere on the basis of the research presented in this submitted work.

I am a member of the VERITAS collaboration, an international collaboration of ~ 100 scientists. Due to the manpower required to operate a ground-based γ-ray observing facility, responsibility for data-taking is shared by the collaboration. Before the start of each observing season, scientists in the collaboration submit observing proposals for particular astrophysical sources to the VERITAS Time Allocation Committee (TAC). The TAC then review these proposals and decide on an observing plan for the entire season. Each collaboration member is required to spend two weeks per year at the facility to operate the array. Therefore, data is taken throughout the season by the crew that happens to be on shift, and not necessarily by the PIs of the sources that are visible. In the season starting September 2013, I was elected graduate member of the VERITAS TAC and will serve in that position until September 2014.

Many sets of of simulations are necessary to support the different analysis cuts (e.g., for different source spectra and array configurations). The simulations are both time and resource intensive. Therefore, they are run by a community of people in the collaboration with access to the necessary computing resources, and made available for use by the entire collaboration.

In summary, collaborators are relied upon for data-taking and upkeep of the analysis software. However, all the analyses presented in this thesis are my own original work.

Anna O'Faoláin de Bhróithe

Acknowledgements

I would like express my gratitude to everyone who has helped me over the past few years. In particular, I would like to thank my research supervisor, Dr. John Quinn for his support and guidance throughout my doctoral studies.

As part of my research, I spent two extended visits at the Fred Lawrence Whipple Observatory in Arizona. I would like to thank Dr. Trevor Weekes for his ideas, advice, and encouragement. I am deeply grateful to him and his wife, Ann, for their exceptional hospitality. I would also like to mention my friends at the observatory; Pascal, Jack, Robert, Larry, Cesar, Emmet, Danny, Don, Grace, and George. Thanks for all the good times, friendship and support. I really wouldn't have made it without you.

I would like to thank the members of my Doctoral Studies Panel; Dr. John Quinn, Dr. Sheila McBreen and Prof. Peter Duffy. A special mention should also go to my colleagues, past and present, in the high energy astrophysics group; Ralph Bird, Anna Cannon, Eddie Collins-Hughes, Yerbol Khassen, Elisa Pueschel and John Ward. Thanks for all the encouragement.

I would like to acknowledge the Irish Research Council for their financial support of this work via the Embark Scholarship.

Finally, I must thank my best friend and partner, Ger Fitzpatrick, for his unwavering support always, and patient proof-reading of this document.

Chapter 1

Introduction

Very-high-energy (VHE; $E > 100\,\mathrm{GeV}$) γ-ray astronomy is the study of the Universe at the highest energies, probing the most extreme environments in existence. X-rays and γ-rays are absorbed in the Earth's atmosphere, making the direct detection of this type of astronomical radiation impossible from the ground. X-ray to γ-ray energy emission can be directly detected by instruments placed on satellites in orbit above the Earth's atmosphere. However, for higher-energy emission, space-borne experiments become increasingly ineffective due to the intrinsically lower fluxes of astrophysical sources at these energies combined with the limitations on the detector area of an instrument that can be launched into orbit (typically $\sim 1\,\mathrm{m}^2$).

In order to detect VHE γ-rays, large detector areas are required (current instruments have detector areas on the order of $10^5\,\mathrm{m}^2$), and to date, it is only feasible to build and operate these instruments on the ground. While the density of matter in the atmosphere is only about $\sim 1.3\,\mathrm{kg\ m}^{-3}$ at ambient pressure, the integrated matter density along the line of sight from sea level to the upper atmosphere is $\sim 10^4\,\mathrm{kg\ m}^{-2}$ (Schönfelder, 2001). The interaction depth of photons in matter is $300\,\mathrm{kg\ m}^{-2}$, and so it is not possible to directly detect the VHE photons. However, secondary detection methods which use the atmosphere as an integral part of the detection system, acting as a calorimeter, can be employed. VHE γ-rays that are incident on the atmosphere initiate extensive air showers (EAS). These showers contain relativistic charged particles which induce Cherenkov radiation (this phenomenon is discussed in more detail in Chapter 2). Using ground-based observations of these child particles and the resultant Cherenkov radiation, the energy and direction of the incident γ-ray can be deduced.

Two techniques are currently employed to detect the products of this interaction with the atmosphere. One technique involves the detection of the relativistic particles, and the other relies on the detection of the Cherenkov radiation produced within the shower. Particle detectors such as MILAGRO (Sullivan & the MILAGRO Collaboration, 2001), which operated from 2000 to 2008, or the current ARGO-YBJ experiment (Iuppa, 2013), have the advantage of a large duty cycle ($\sim 100\%$) and a field of view (FoV) of $\sim 1-2\,\Omega$. However, due to inefficient rejection of the abundant cosmic ray background, they have limited sensitivity.

The Cherenkov radiation that is generated by EAS can be observed by cameras sensitive in the optical to UV range. These Cherenkov detectors were first conceived as non-imaging detectors (e.g., the Whipple 10 m Telescope $1968-1982$). They soon evolved into imaging systems known as imaging atmospheric Cherenkov telescopes (IACTs, e.g., the Whipple 10 m Telescope post-1982 (Kildea et al., 2007), and current experiments such as VERITAS (Holder et al., 2008), H.E.S.S. (Hinton, 2004), and MAGIC (Aleksić et al., 2012)). The imaging capabilities provide excellent background rejection based on the morphology of the images, as γ-ray-initiated showers produce different types of images in general to showers initiated by background cosmic ray particles.

Current IACTs have a typical FoV of $\sim 3-5^{\circ}$ and a $\sim 15\%$ duty cycle, as the telescopes cannot be operated in daylight or poor weather conditions. IACTs are now the primary method of detecting VHE γ-rays due to their good angular and energy resolution of photons with energies spanning ~ 100 GeV up to a few tens of TeV, combined with their high background rejection capability. Hillas (2013) provides an overview of the field, including the evolution of the techniques used, from its inception in the 1950s to the current era. Paneque (2012) provides a review of some of the highlights from the field in recent years.

1.1 Current status of VHE astronomy

There are currently three major IACT observatories in operation. VERITAS, located at the Fred Lawrence Whipple Observatory in southern Arizona, consists of four telescopes arranged approximately as a square. Each telescope has a reflecting area of $\sim 107\,\mathrm{m}^2$ and a focal plane camera with a FoV of $3^{\circ}\!.5$. H.E.S.S., located in the Khomas Highland of Namibia, had a similar setup (H.E.S.S. I) with four telescopes of reflecting area $\sim 107\,\mathrm{m}^2$ and a 5° FoV camera arranged in a square formation. H.E.S.S. II, the largest IACT built to date, with a reflecting area of $\sim 600\,\mathrm{m}^2$, saw first light in 2012 and operates as part of the full H.E.S.S. array. MAGIC is situated on La Palma, and originally consisted of a single large reflector of area $236\,\mathrm{m}^2$ with

Parameter	VERITAS	H.E.S.S.	MAGIC
Hemisphere	North	South	North
Number of telescopes	4	5	2
Height a.s.l. (m)	~ 1270	~ 1800	~ 2200
Low energy threshold (GeV)	~ 100	~ 100 (expected to decrease with H.E.S.S. II)	~ 50
Sensitivity > 1 TeV (% Crab)	~ 0.7	~ 0.7 (expected to decrease with H.E.S.S. II)	~ 0.8
Energy resolution	$\sim 15\%$	$\sim 15\%$	$\sim 16\%$
Effective area (m^2)	$\sim 10^5$	$\sim 10^5$	$\sim 10^5$
FoV (°)	3.5	5 (H.E.S.S. I) 3.2 (H.E.S.S. II)	3.5
Systematic uncertainty:			
Flux (%)	~ 40	~ 20	~ 19
Spectral index	~ 0.3	~ 0.09	~ 0.15

Table 1.1: Performance parameters of the three major current IACT observatories. Information for this table collated from (Holder et al., 2008; Hinton, 2004; Aharonian et al., 2006; Aleksić et al., 2012; Acharya et al., 2013).

a $3\overset{\circ}{.}5$ FoV camera. A second telescope of the same dimension was added to MAGIC in 2009, allowing the experiment to operate in stereoscopic mode.

These three observatories complement each other by fulfilling different roles. MAGIC observes the northern sky with a low energy threshold of ~ 50 GeV (Aleksić et al., 2012). VERITAS and H.E.S.S. are more sensitive, but have slightly higher energy thresholds, and H.E.S.S. provides coverage of the southern hemisphere. Table 1.1 provides a comparison of the performance parameters of the observatories.

These ground-based observatories are complemented by the Large Area Telescope (LAT) (Atwood et al., 2009) on board the *Fermi* Gamma-ray Space Telescope. While IACTs cover the energy range between ~ 50 GeV and ~ 50 TeV, the LAT is sensitive from ~ 20 MeV to ~ 300 GeV. This overlap in the energy ranges of these instruments provides the potential for seamless coverage of the γ-ray energy spectra of astrophysical sources.

The locations of the IACT experiments provide coverage of both the northern and southern hemispheres of the VHE γ-ray sky. Since the discovery of the first VHE emitter in 1989 (Weekes et al., 1989), the number of VHE γ-ray sources has grown dramatically, increasing more than 10-fold in the last ten years alone. There are currently ~ 150 discrete sources of emission in the VHE γ-ray sky. These are shown in galactic coordinates in Figure 1.1.

Sources of VHE emission can be divided into six main categories. These are pulsar wind nebulae

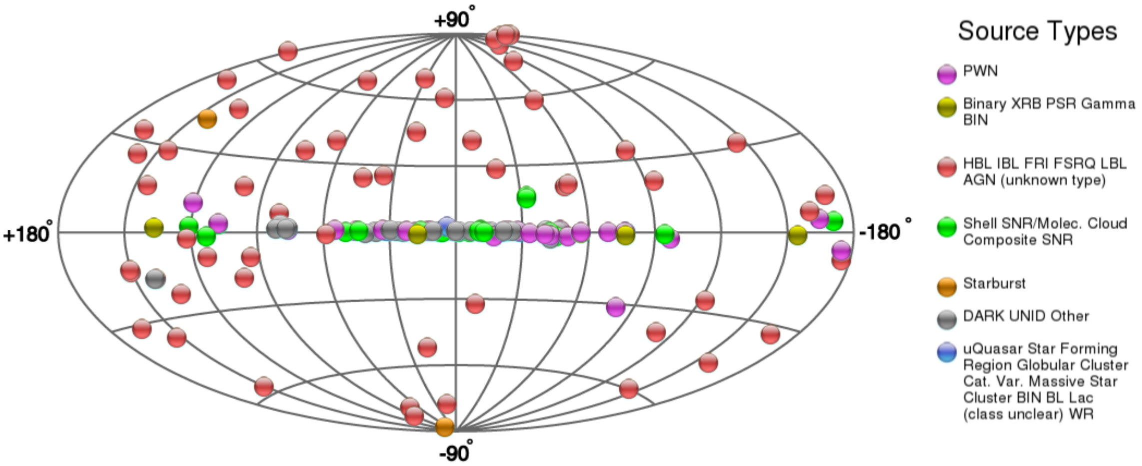

Figure 1.1: Localised sources of VHE γ-ray emission as of February 2014, displayed in galactic coordinates. The different source categories are represented by different colour markers. The majority of categories are confined to the galactic plane, with the exception of the AGN class which is distributed isotropically across the sky. This figure was created from the online catalog TeVCat (Wakely & Horan, 2014).

(PWNe), binary sources, active galactic nuclei (AGN), supernova remnants (SNRs), starburst galaxies, and unidentified sources (sources without counterparts at other wavelengths). These categories cover a wide variety of astronomical objects, from the Geminga PWN in our own galaxy at distance of ~ 0.17 kpc to the AGN PKS 1424+240 located at a redshift of $z > 0.6$, reflecting the power and versatility of ground-based γ-ray astronomy. In all these disperate source classes, non-thermal processes in the source environment produce the VHE emission that is observed from the ground.

The AGN category is the most numerous, accounting for more than a third of all VHE sources. Blazars are the most common member of the AGN category, representing $\sim 90\%$ of the sources in this class. The PWNe source class is the next biggest after AGN, constituting just over a fifth of the total number of sources. This thesis concerns the study of γ-ray emission from 1ES 1959+650, an AGN, and the famous Crab Nebula, a member of the PWNe class.

An overview of blazars is provided in Section 1.2. In Section 1.3, the Crab Nebula, which is still providing surprises and new science in spite of being one of the most studied PWNe, is introduced.

1.2 Blazars

AGN are galaxies that have very energetic central regions that produce more radiation than the rest of the galaxy in its entirety. A super-massive black hole in the range $10^4 - 10^{10}$ solar masses at the centre of the active galaxy is believed to be the central engine of the system (Urry & Padovani, 1995). Matter is pulled towards the black hole, forming an accretion disk which emits radiation at UV energies. The radiation from the disk ionises nearby gas clouds. These clouds emit strong optical and UV lines, and as they move rapidly in the potential of the black hole, the lines are broadened due to the Doppler effect. This is known as the broad line region. The optical and UV radiation is obscured around the equator of the system by a torus of gas and dust that lies beyond the accretion disk and broad line region. Slower moving gas clouds beyond the torus produce narrower emission lines in what is known as the narrow line region. Outflows of energetic particles at the poles of the disk and torus escape and form collimated jets of plasma. This setup is shown in Figure 1.2.

The emission from AGN is dominated by non-thermal radiation, and is generally characterised by rapid and large-amplitude flux variability. AGN have historically been divded into sub-classes based on radio emission properties. Radio loud AGN emit collimated plasma jets, but the majority of AGN do not exhibit such jet features, and are classified as radio quiet. The current paradigm of AGN is a unified scheme in which the differences in the observed properties of AGN are attributed to the orientation of the system relative to the observing angle (Antonucci, 1993; Urry & Padovani, 1995). This scheme is illustrated in Figure 1.2.

To date, only radio loud AGN have been detected at VHE. In the case that the jet emitted by the AGN is closely aligned along our line of sight, the object is called a blazar. Blazars appear bright across the full spectrum from radio to γ-ray energies due to this alignment. They alone account for fully one third of the total number of VHE sources detected to date, and are almost the sole category of extragalactic VHE emission. Their spectral energy distribution (SED) is characterised by a double-peaked structure. The low-energy peak, which can lie anywhere from the radio to X-ray regime, is generally attributed to synchrotron emission from relativistic electrons. The origin of the high-energy peak depends on whether the emission is dominated by leptonic or hadronic processes, however, it is most usually associated with inverse-Compton (IC) emission.

BL Lac objects are a subset of blazars characterised by nonthermal continuum emission without emission lines, and strong, rapid variability. They may be divided into three classes based on the position of the synchrotron peak in frequency space (Padovani & Giommi, 1995). High-frequency peaked BL Lacs (HBLs) exhibit synchrotron peak emission at UV – X-ray frequencies, intermediate-frequency peaked BL Lacs (IBLs) show synchrotron peak emission at optical – UV frequencies, and low-frequency peaked BL Lacs (LBLs) have their synchrotron peak emission in

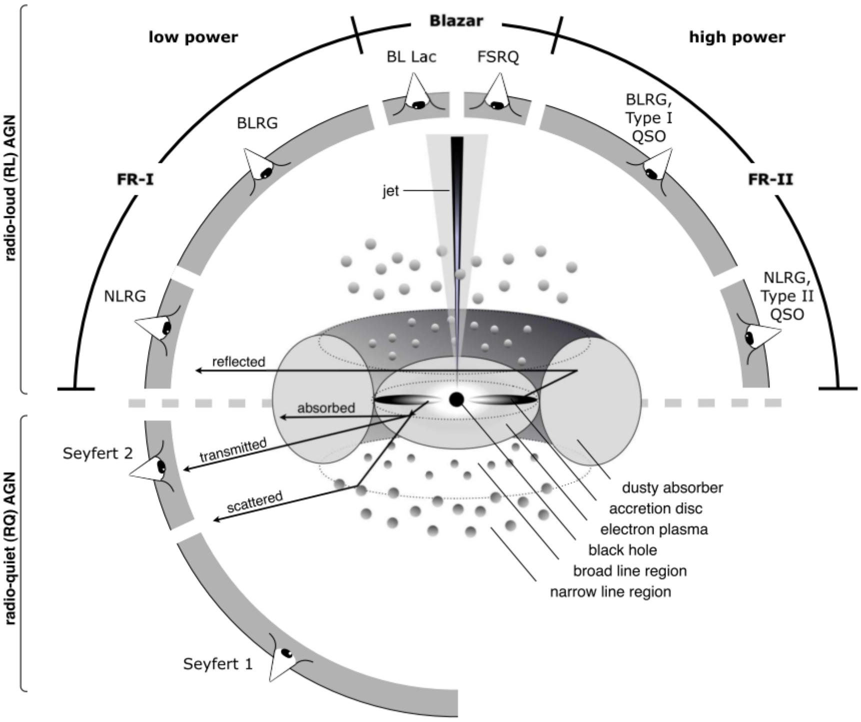

Figure 1.2: Schematic representation of the geometry of an AGN showing the black hole at the centre surrounded by the accretion disk and the dusty torus. The broad line region is depicted with by the smaller blobs close to the black hole, and the narrow line region is marked by the larger blobs further away from the black hole. A single jet emerging from the pole of the accretion disk and torus (i.e., perpendicular to the plane of the disk and torus) is shown. The relationship between AGN class and observing angle is represented on the arc surrounding the AGN. It can be seen from this picture that blazars are observed very closely along the axis of the jet. Figure taken from Beckmann & Shrader (2013).

IR – optical bands.

Figure 1.3 shows a map of the VHE blazars currently detected, with the region of the sky observable by VERITAS ($\gtrsim 55^\circ$ elevation) marked in blue. The majority of these blazars ($\sim 75\%$) are HBLs. This dominance of HBLs over other subclasses is reflected even in the VERITAS-detected subset of blazars, which is listed in Table 1.2.

Blazars with redshifts of $z > 0.5$ have been detected in VHE γ-rays (3C 279 with $z = 0.536$ and PKS 1424+240 with $z > 0.604$). The observation of VHE emission from these very distant sources has been a surprising result, as the high-energy photons are expected to be absorbed through interactions with the low-energy photons of the extragalactic background light (EBL) (Mazin et al., 2009). The VHE γ-rays pair-produce via $\gamma\gamma$ interactions with the EBL photons, a process which is energy-dependent, and increases strongly with redshift. Thus, these detections of distant blazars put strong contraints on the EBL density in the optical to near IR waveband.

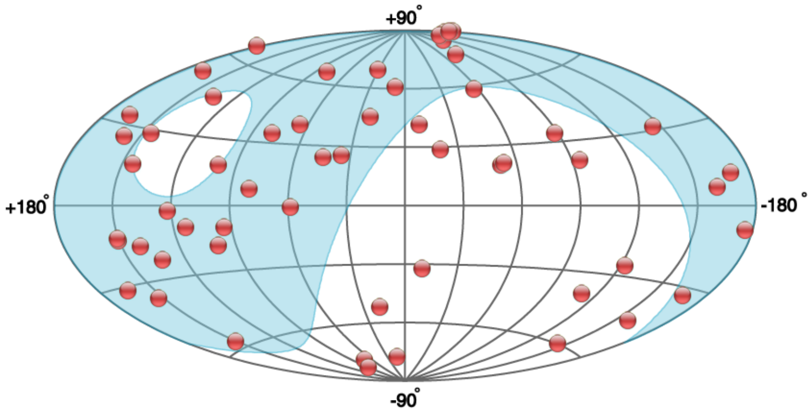

Figure 1.3: A map of the VHE blazars detected to date. Shown in blue is the region of the sky observable above $\sim 55°$ elevation from the northern hemisphere (i.e., VERITAS and MAGIC sites). This figure was generated by TeVCat.

AGN	Type	Redshift (z)
M 87	FR 1	0.004
NGC 1275	FR 1	0.018
Mkn 421	HBL	0.030
Mkn 501	HBL	0.034
1ES 2344+514	HBL	0.044
1ES 1959+650	HBL	0.047
1ES 1727+502	HBL	0.055
BL Lac	LBL	0.069
1ES 1741+196	HBL	0.086
W Comae	IBL	0.102
VER J0521+211	HBL	0.108
RGB J0710+591	HBL	0.125
H 1426+428	HBL	0.129
1ES 0806+524	HBL	0.138
1ES 0229+200	HBL	0.139
1ES 1440+122	HBL	0.163
RX J0648.7+1516	HBL	0.179
1ES 1218+304	HBL	0.182
RBS 0413	HBL	0.190
1ES 1011+496	HBL	0.212
1ES 0414+009	HBL	0.287
1ES 0033+595	HBL	-
B2 1215+30	IBL	-
1ES 0647+250	HBL	-
1ES 0502+675	HBL	-
3C 66A	IBL	$0.33 < z < 0.41$
PG 1553+113	HBL	$0.43 < z < 0.58$
PKS 1424+240	IBL	> 0.604

Table 1.2: The subset of blazars detected by VERITAS. A dash in the third column indicates that the redshift is uncertain.

The VHE emission of blazars is characterised by clear variability, which can in some cases be very extreme. For example, the blazar PKS 2155-304 has exhibited > 2-fold flux increases in < 3 hours (Aharonian et al., 2005), and even minute-scale variations (Aharonian et al., 2007). Such fast variability timescales can be used to constrain the size and location of the emitting region in these blazars.

Simultaneous multiwavelength observations have revealed the complexity of the emission from these sources. In some cases, observations provide evience for a correlation between VHE γ-ray and X-ray emission (Fossati et al., 2008). This lead to the assumption that the VHE emission originates from the same electron population that is accelerated in the jet and produces the synchrotron radiation. However, this correlation has been completely non-existent in other cases, such as the VHE "orphan" flare of 1ES 1959+650 in June 2002 (Krawczynski et al., 2004), when the VHE γ-ray flux increased by a factor of ten without a corresponding increase in the X-ray emission.

In this thesis, the VHE detection of 1ES 1959+650 from 2007 − 2011 is presented. This BL Lac object was originally detected as a source of VHE γ-rays by the Utah Seven Telescope Array (Nishiyama, 1999), and confirmed by the Whipple 10 m Telescope (Holder et al., 2003) during a dramatic flaring episode in 2002. During this flare, and increase in VHE γ-ray flux was detected without a corresponding increase in the X-ray emission, providing the first unambiguous example of an "orphan" γ-ray flare (Krawczynski et al., 2004; Holder et al., 2003; Daniel et al., 2005).

This source was monitored as part of the VERITAS blazar monitoring program in the hopes of observing it in another dramatic outburst. Over seasons of these monitoring observations, a significant detection was accumulated of the source in its non-flaring, low flux state. Contemporaneous multiwavelength observations of the source were analysed to complement the VHE data. A multiwavelength SED from these data is presented in this thesis, and is modelled with a synchrotron self-Compton (SSC) model with the addition of an external Compton (EC) component.

1.3 The Crab Nebula

The Crab Nebula was the first detected VHE γ-ray source (Weekes et al., 1989). It was already considered the "standard candle" calibration source of X-ray astronomy (Toor & Seward, 1974; Kirsch et al., 2005), and so it was adopted as the VHE standard candle too. The energy scale of X-ray instruments can be calibrated against emission lines of radioactive sources, and due to their design, they have a fixed volume which results in a well-known effective area. No such energy or flux calibration tools exists at VHE energies. Therefore, the Crab Nebula became the only calibration source of VHE astronomy, with other calibration methods relying on the measurement of background cosmic rays or muons.

In 2011, variability of the X-ray and γ-ray emission of the Crab Nebula was announced. Wilson-Hodge et al. (2011) reported a decline of $\sim 7\%$ in the nebula in the $15 - 50$ kev band since 2008 observed by *Fermi*-GBM and independently confirmed by *Swift*-BAT, RXTE-PCA and INTEGRAL-IBIS. A similar decline was also seen in the $\sim 3 - 15$ keV band with RXTE-PCA, and in from 50 to 100 keV with *Fermi*-GBM, *Swift*-BAT and INTEGRAL-IBIS.

In the same month, Tavani et al. (2011) reported the detection of strong γ-ray flares in the range $0.1 - 10$ GeV with AGILE in October 2007 and September 2010. This was corroborated by Abdo et al. (2011), who reported > 100 MeV flares detected by *Fermi*-LAT in February 2009 and September 2010, the latter being the same flare as seen by AGILE.

The presence of such variability at VHE energies would have far-reaching implications for the use of the Crab Nebula as a VHE calibration source. However, both MAGIC and VERITAS reported no flux enhancement or spectral change during the flare in September 2010 (Mariotti, 2010; Ong, 2010). Interestingly, ARGO-YBJ reported a flux about 3−4 times higher than the average emission at a median energy of ~ 1 TeV for the same event from a preliminary analysis of their data (Vernetto, 2010).

Recently, ARGO-YBJ data from the last five years has been reanalysed to study the variability of the Crab Nebula in the $0.5 - 20$ TeV energy range. The long-term light curve is consistent with a uniform flux with a probability of 0.11 (Vernetto, 2013), but a very tenuous correlation with the corresponding *Fermi*-LAT light curve is also reported. Neglecting the significance of the result, and assuming that the correlation is in fact real, this implies the same behaviour of the gamma-ray emission at energies ~ 100 MeV and ~ 1 TeV.

Given the ample evidence for high-energy variability of the Crab Nebula, a ToO programme was accepted by VERITAS to observe the nebula in the event of another flare. This programme was triggered in March 2013, and VERITAS obtained the most comprehensive VHE coverage to date of a Crab Nebula flare. These flare observations and their implications are studied in this thesis. In addition, the archival VHE data on the Crab Nebula from the Whipple 10 m Telescope and VERITAS are also retrospectively searched for the presence of any VHE enhancement that could be associated with a flaring episode.

1.4 Thesis overview

This thesis concerns the study of inverse-Compton emission from two astrophysical sources. The first object, the BL Lac object 1ES 1959+650, is a nearby AGN. It exhibited a dramated orphan VHE flare in 2002, but here it is detected in a low VHE flux state. The second object is the famous Crab Nebula, for years considered the standard candle of X-ray to VHE γ-ray astronomy. Now is an opportune time to conclude an in-depth study of this source at VHE energies, in light of the recent developments in understanding its true behaviour.

The instrumentation used in the analysis presented in this thesis is described in Chapter 2. An overview of the analysis techniques for the various instruments is given in Chapter 3. The current theoretical understanding of the two astrophysical sources studied is addressed in Chapter 4.

Chapter 5 presents the multiwavelength analysis of the Blazar 1ES 1959+650. This source was observed as part of the VERITAS blazar monitoring programme in the hopes of detecting it in the midst of a dramatic flaring event. Over the course of these monitoring observations which span 4 years, a significant detection of the source in its low state was accumulated. The spectral energy distribution of this source was analysed from optical to VHE and was modelled with a SSC+EC model. The parameters obtained cannot be fully explained by first-order Fermi acceleration at parallel shocks, and instead may suggest particle acceleration at oblique subluminal shocks, or that 1ES 1959+650 may consist of an inhomogeneous jet with a fast inner spine and slower-moving outer cocoon. The work presented in this chapter was published in the Astrophysical Journal (Aliu et al., 2013).

Chapter 6 describes the analysis of VERITAS data taken during the recent synchrotron flare of the Crab Nebula in March 2013. A ToO programme, of which the author was PI, was in place for VERITAS to observe the nebula if it entered a flaring synchrotron state. VERITAS observed the Crab Nebula on 10 nights during the two-week flare. No enhanced VHE emission was detected, but the observations facilitated the calculation of upper limits on any extra VHE spectral component emerging during the flare. The work presented in this Chapter was published in the Astrophysical Journal Letters (Aliu et al., 2014).

Chapter 7 reports on a search for short-term variability in the Crab Nebula using archival VHE data. Data from the Whipple 10 m Telescope from 2000 − 2010 was analysed and searched. No significant flaring activity was identified in these 10 years of data. VERITAS observations of the Crab Nebula since the beginning of operations of the full four-telescope telescope array were also analysed. The resulting light curves show no evidence for short-term flares. However, a slight decrease in the long-term flux of the Nebula was detected. This is could possibly be correlated with increasing instability of the aerosol content of the local atmosphere around the VERITAS site.

1.5 Bibliography

Abdo, A. A., Ackermann, M., Ajello, M., et al., 2011; 'Gamma-ray flares from the Crab Nebula.' *Science (New York, N.Y.)*, vol. 331(6018):739

Acharya, B., Actis, M., Aghajani, T., et al., 2013; 'Introducing the CTA concept'. *Astroparticle Physics*, vol. 43:3

Aharonian, F., Akhperjanian, A. G., Bazer-Bachi, A. R., et al., 2005; 'Multi-wavelength observations of PKS 2155-304 with HESS'. *Astronomy and Astrophysics*, vol. 442(3):895

—, 2006; 'Observations of the Crab nebula with HESS'. *Astronomy and Astrophysics*, vol. 457(3):899

—, 2007; 'An Exceptional Very High Energy Gamma-Ray Flare of PKS 2155-304'. *The Astrophysical Journal*, vol. 664(2):L71

Aleksić, J., Alvarez, E., Antonelli, L., et al., 2012; 'Performance of the MAGIC stereo system obtained with Crab Nebula data'. *Astroparticle Physics*, vol. 35(7):435

Aliu, E., Archambault, S., Arlen, T., et al., 2013; 'Multiwavelength Observations and Modeling of 1ES 1959+650 in a Low Flux State'. *The Astrophysical Journal*, vol. 775:3

Aliu, E., Archambault, S., Aune, T., et al., 2014; 'A search for enhanced very-high-energy gamma-ray emission from the March 2013 Crab Nebula flare'. *The Astrophysical Journal*, vol. 781(1):L11

Antonucci, R., 1993; 'Unified Models for Active Galactic Nucle and Quasars'. *Annual Review of Astronomy and Astrophysics*, vol. 31(1):473

Atwood, W. B., Abdo, A. A., Ackermann, M., et al., 2009; 'THE LARGE AREA TELESCOPE ON THE FERMI GAMMA-RAY SPACE TELESCOPE MISSION'. *The Astrophysical Journal*, vol. 697(2):1071

Beckmann, V., Shrader, C. R., 2013; 'The AGN phenomenon: open issues'. In '"An INTEGRAL view of the high-energy sky (the first 10 years)" 9th INTEGRAL Workshop and celebration of the 10th anniversary of the launch', Bibliotheque Nationale de France, Paris, France

Daniel, M. K., Badran, H. M., Bond, I. H., et al., 2005; ‘Spectrum of Very High Energy Gamma-Rays from the blazar 1ES 1959+650 during Flaring Activity in 2002’. *The Astrophysical Journal*, vol. 621(1):181

Fossati, G., Buckley, J. H., Bond, I. H., et al., 2008; ‘Multiwavelength Observations of Markarian 421 in 2001 March: An Unprecedented View on the XRay/TeV Correlated Variability’. *The Astrophysical Journal*, vol. 677(2):906

Hillas, A., 2013; ‘Evolution of ground-based gamma-ray astronomy from the early days to the Cherenkov Telescope Arrays’. *Astroparticle Physics*, vol. 43:19

Hinton, J., 2004; ‘The status of the HESS project’. *New Astronomy Reviews*, vol. 48(5-6):331

Holder, J., Acciari, V. A., Aliu, E., et al., 2008; ‘Status of the VERITAS Observatory.’ *Proceedings of the 4th International Meeting on High Energy Gamma-Ray Astronomy*, vol. 1085(1):657

Holder, J., Bond, I. H., Boyle, P. J., et al., 2003; ‘Detection of TeV Gamma Rays from the BL Lacertae Object 1ES 1959+650 with the Whipple 10 Meter Telescope’. *The Astrophysical Journal Letters*, vol. 583(1):L9

Iuppa, R., 2013; ‘Results from the ARGO-YBJ experiment’. *Journal of Instrumentation*, vol. 8(08):T08002

Kildea, J., Atkins, R. W., Badran, H. M., et al., 2007; ‘The Whipple Observatory 10 m gamma-ray telescope, 1997 - 2006’. *Astroparticle Physics*, vol. 28(2):182

Kirsch, M. G., Briel, U. G., Burrows, D. N., et al., 2005; ‘Crab: the standard X-ray candle with all (modern) X-ray satellites’. In ‘Society of Photo-Optical Instrumentation Engineers (SPIE) Conference Series’, , (ed. Siegmund, O. H. W.), vol. 5898 of *Society of Photo-Optical Instrumentation Engineers (SPIE) Conference Series*, 22–33

Krawczynski, H., Hughes, S. B., Horan, D., et al., 2004; ‘Multiwavelength Observations of Strong Flares from the TeV Blazar 1ES 1959+650’. *The Astrophysical Journal*, vol. 601(1):151

Mariotti, M., 2010; ‘No significant enhancement in the VHE gamma-ray flux of the Crab Nebula measured by MAGIC in September 2010’. *The Astronomer’s Telegram*, vol. 2967

Mazin, D., Bastieri, D., Rando, R., 2009; ‘Constraints on Extragalactic Background Light from Cherenkov telescopes: status and perspectives for the next 5 years’. In ‘AIP Conference Proceedings’, 111–120. AIP

Nishiyama, T., 1999; 'Detection of a new TeV gamma-ray source of BL Lac object 1ES 1959+650'. In 'Proceedings of the 26th International Cosmic Ray Conference', , (eds. Dingus, B. L., Kieda, D. B., Salamon, M. H.), vol. 3 of *International Cosmic Ray Conference*, 370. Salt Lake City, USA

Ong, R. A., 2010; 'Search for an Enhanced TeV Gamma-Ray Flux from the Crab Nebula with VERITAS'. *The Astronomer's Telegram*, vol. 2968

Padovani, P., Giommi, P., 1995; 'The connection between x-ray- and radio-selected BL Lacertae objects'. *The Astrophysical Journal*, vol. 444:567

Paneque, D., 2012; 'Experimental Gamma-Ray Astronomy'. *Journal of Physics: Conference Series*, vol. 375(5):052020

Schönfelder, V. (Ed.) , 2001; *The Universe in Gamma Rays*. Springer-Verlag

Sullivan, G., the MILAGRO Collaboration, 2001; 'Status of the MILAGRO gamma ray observatory'. In 'Proceedings of the 27th International Cosmic Ray Conference', Hamburg, Germany

Tavani, M., Bulgarelli, A., Vittorini, V., et al., 2011; 'Discovery of powerful gamma-ray flares from the Crab Nebula.' *Science (New York, N.Y.)*, vol. 331(6018):736

Toor, A., Seward, F. D., 1974; 'The Crab Nebula as a calibration source for X-ray astronomy'. *The Astronomical Journal*, vol. 79:995

Urry, C. M., Padovani, P., 1995; 'Unified Schemes for Radio-Loud Active Galactic Nuclei'. *Publications of the Astronomical Society of the Pacific*, vol. 107:803

Vernetto, S., 2010; 'Enhanced TeV gamma ray flux from the Crab Nebula observed'. *The Astronomer's Telegram*, vol. 2921

—, 2013; 'Study of the Crab Nebula TeV emission variability during five years with ARGO-YBJ'. In 'Proceedings of the 33rd International Cosmic Ray Conference', 4. Rio de Janeiro, Brazil

Wakely, S., Horan, D., 2014; 'http://tevcat.uchicago.edu'

Weekes, T. C., Cawley, M. F., Fegan, D. J., et al., 1989; 'Observation of TeV gamma rays from the Crab nebula using the atmospheric Cerenkov imaging technique'. *The Astrophysical Journal*, vol. 342:379

Wilson-Hodge, C. A., Cherry, M. L., Case, G. L., et al., 2011; 'WHEN A STANDARD CANDLE FLICKERS'. *The Astrophysical Journal Letters*, vol. 727(2):L40

CHAPTER 2

Instruments

This chapter gives an overview of the observatories whose data was used in this thesis. Some observatories, such as the Whipple 10 m Telescope and VERITAS, are ground-based experiments, while others are satellites in orbit about the Earth. The data from the VERITAS and Whipple experiments is only available to members of the respective collaborations. The data are analysed using software suites internal to the collaboration. In contrast, the data from the γ-ray and X-ray instruments used in this work are completely public. These data were reduced and analysed using the appropriate publicly available tools. The data analysis procedures are described in Chapter 3.

2.1 Ground-based γ-ray detectors

The Earth's atmosphere is opaque to photons with energies greater than the visible waveband. In general, this means that if they are to be observed, the detector should be placed above the atmosphere. Due to the low flux of VHE photons, such detectors would require detector areas much greater than is practical to construct and launch into orbit. However, a secondary detection method can be employed to observe VHE photons using ground-based instruments.

VHE photons initiate EAS when they interact with the atmosphere. The high-energy photon produces an electron-positron pair. On average, the energy of the photon is shared equally between the electron and positron. These then undergo bremsstrahlung in the field of an atomic nucleus and radiate γ-rays, which can pair produce again if they have sufficient energy ($\gtrsim 1\,$MeV). In this manner, the number of particles in the cascade multiplies, with the energy of the original γ-ray being distributed among the secondary particles. The shower continues to grow until ionization losses (which dominate at low energies) exceed bremsstrahlung losses (which dominate at high energies). This occurs at the *critical energy* E_c where both are equal ($E_c \simeq 84$ MeV for air). This determines the shower maximum, and after this point, the shower becomes attenuated as increasingly more particles fall below the energy threshold for further particle production.

The variation of the number of particles with atmospheric depth (or radiation length) is referred to as the longitudinal shower development. The radiation length for photons and electrons in air is $\chi_0 \simeq 37$ g cm^{-2}, so the full depth of the atmosphere corresponds to ~ 27 radiation lengths. The mean free path of a photon in air is $(9/7)\chi_0 \simeq 47.5$ g cm^{-2}. Figure 2.1 illustrates the longitudinal development of showers in the atmosphere.

Hadrons incident on the atmosphere also produce EAS, but the showers propagate in a much more complex fashion. Pair production and bremsstrahlung still play a role, but hadronic particle production via the strong and weak force also contribute. Hadrons are much more numerous than γ-rays, and so form a large part of the background measured by ground-based γ-ray detectors. However, there are some general distinguishing differences between γ-ray-initiated (electromagnetic) and hadron-initiated (hadronic) showers. Hadronic showers have a much broader lateral extension than the more compact electromagnetic showers. Hadronic showers are also less regular and exhibit larger asymmetry in their development in comparison to electromagnetic showers. Finally, the interaction depth of hadrons in the atmosphere is 2 − 3 times that of a photon, which means that hadrons penetrate deeper into the atmosphere than γ-rays. Figure 2.1 shows a 100 GeV γ-ray-initiated shower compared to a hadron-initiated shower of the same energy. The differences in lateral spread and symmetry for the different shower types are clearly visible.

These differences in the electromagnetic and hadronic showers are apparent in the shape and time structure of the Cherenkov light that reaches the ground. The showers develop almost at light speed, resulting in very short flashes of Cherenkov light. For an electromagnetic shower, the photons typically arrive at the ground within an interval of 2 − 5 ns, whereas hadronic showers exhibit a broader spread of arrival times in the range 10 − 15 ns. The light distribution from hadronic showers is far more heterogeneous and asymmetric than that of electromagnetic showers. These differing properties can be exploited to discriminate between the electromagnetic showers and their hadronic background, and are utilised in the IACT analysis chains described in Chapter 3.

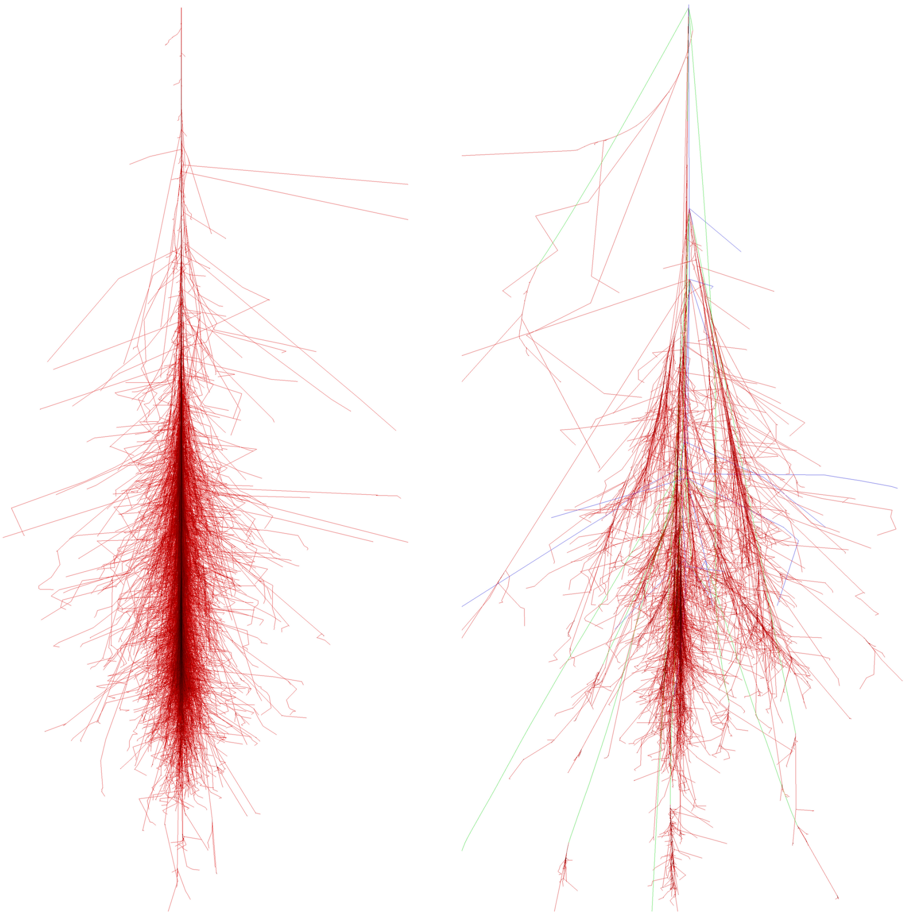

Figure 2.1: Simulations of EAS initiated by a 100 GeV γ-ray (left) and a 100 GeV proton (right), both normally incident on the atmosphere. These images show the longitudinal development of the showers over ~ 30 km. The coloured lines correspond to the particle tracks, where red represents electron, positrons and photons, green represents muons and blue represents hadrons. Images taken from Schmidt (2014). It can be seen from this figure that γ-ray-initiated showers essentially resemble a glowing column of light in the sky. Accordingly, they are detected as ellipses from the ground.

Cherenkov emission from EAS

Relativistic charged particles in EAS travel faster than the phase velocity of light in the atmosphere, i.e.,

$$\beta n > 1, \tag{2.1.1}$$

where $\beta = v/c$ is the velocity of the particle, and n is the refractive index of the atmosphere. In this situation, Cherenkov radiation is emitted (Jelley, 1958). This effectively imposes a lower limit on the energy of particles that can create Cherenkov photons. This minimum energy is given by

$$E_{\text{min}} = mc^2 \left(\frac{n}{\sqrt{n^2 - 1}} - 1 \right), \tag{2.1.2}$$

where m is the mass of the particle. Due to this dependence on the particle mass, lighter particles are more effective at producing Cherenkov emission. An electron at sea level, for example, must have an energy $\gtrsim 21$ MeV in order to produce Cherenkov radiation (Schönfelder, 2001).

The Cherenkov photons are emitted in a cone about the direction of the particle velocity, the opening angle θ of which is given by

$$\cos\theta = \frac{1}{\beta n}. \tag{2.1.3}$$

Thus, the overall Cherenkov radiation in EAS is emitted along the shower direction and results in a light pool on the ground. This Cherenkov light may be detected from anywhere within the boundary of the light pool by specifically designed Imaging Atmospheric Cherenkov Telescopes (IACTs). Two IACTs, the Whipple 10 m Telescope and its successor, VERITAS, are discussed below.

Background for electromagnetic EAS

The main challenge for ground-based detectors is to distinguish γ-ray showers from background events. Hadrons, cosmic electrons, muons and the NSB are the main sources of background for IACTs (Fegan, 1997).

Hadrons Hadronic showers provide the dominant background contribution, being more numerous than γ-rays by a factor of $\sim 10^3$. In general, these EAS are bigger and more irregular than electromagnetic showers, and so they can be rejected based on the shape of the Cherenkov image. This is a fundamental tool used in the analysis chains of the Whipple telescope and VERITAS, described in Chapter 3. Hadronic showers can also be rejected on the basis of their arrival direction. They arrive isotropically at the Earth due to the fact that they are deflected in the interstellar magnetic field, and therefore they can easily be distinguished from a discrete γ-ray source.

Electrons Images of showers initiated by cosmic electrons are indistinguishable from γ-ray-initiated showers, as they cause the same type of electromagnetic EAS in the atmosphere. Rejection of these particles can only be achieved based on their arrival direction.

Muons These are high-energy secondary particles produced with the EAS itself. Due to the small light pool of a single muon, only those passing very close to the telescopes (within metres) can be detected. This is in contrast to γ-ray shower light pools, which can have footprints with diameters on the order of hundreds of metres. Muons were particularly problematic for single-telescope setups, but for an array of telescopes, images of the same muon in multiple telescopes cannot occur, provided the telescopes are sufficiently far apart. Therefore, a simple requirement that the light pool is detected in more than one telescope drastically reduces the contamination from local muons. Muon events are still occasionally recorded if there is a simultaneous trigger in a second telescope. These remaining events can be efficiently rejected using stereoscopic event reconstruction.

NSB The night sky background is a catch-all phrase which covers a selection of various optical background sources. The most obvious contributors are starlight, moonlight and man-made light pollution. In addition to these, the optical emission from atoms and molecules in the upper atmosphere (air-glow) also contributes. The intensity of this component increases at lower elevations above the horizon. A further component arises due to zodiacal light. This is sunlight that is scattered by dust near the ecliptic, and is most prominent just after sunset and before sunrise when the sun is near the horizon. The NSB imposes limits on the minimum intensity of Cherenkov light that can be detected by IACTs. Due to its random nature, fast electronics and clever trigger systems can suppress the amount of NSB fluctuations recorded by IACTs.

2.1.1 Whipple 10 m telescope

The Whipple 10 m Telescope was the first large purpose-built telescope for atmospheric Cherenkov astronomy. It was completed in 1968, and operated as an IACT from 1982 – 2011. It was situated at the Fred Lawrence Whipple Observatory on Mt. Hopkins in southern Arizona at an altitude of 2.3 km above sea level (Kildea et al., 2007).

The telescope was of Davies-Cotton design, consisting of an optical support structure (OSS), a large curved reflecting surface, and a camera at the focal plane to record the γ-ray images. The OSS was a steel system providing a spherical surface on which to mount the reflector, with opening diameter 10 m and radius of curvature 7.3 m. The reflector was composed of 248 tessellated hexagonal mirrors with a radius of curvature twice that of the OSS. This provided a total reflecting are of $\sim 75\,\mathrm{m}^2$. The focal point camera was improved many times over the lifetime of the telescope, but the last camera in operation consisted of 379 photomultiplier tube (PMT) pixels, and had a field of view (FoV) of $\sim 2.6^\circ$ with an individual pixel diameter of $0\overset{\circ}{.}117$. Figure 2.2 shows the telescope at stow position.

A schematic of the Davies-Cotton reflector design is shown in Figure 2.3. This design is optimised to produce no global spherical aberration on the optic axis, and for smaller aberrations off-axis compared to a parabolic design. However, a draw-back of the Davies-Cotton configuration is that the structure is anisochronous. Incoming rays striking the reflector at different distances

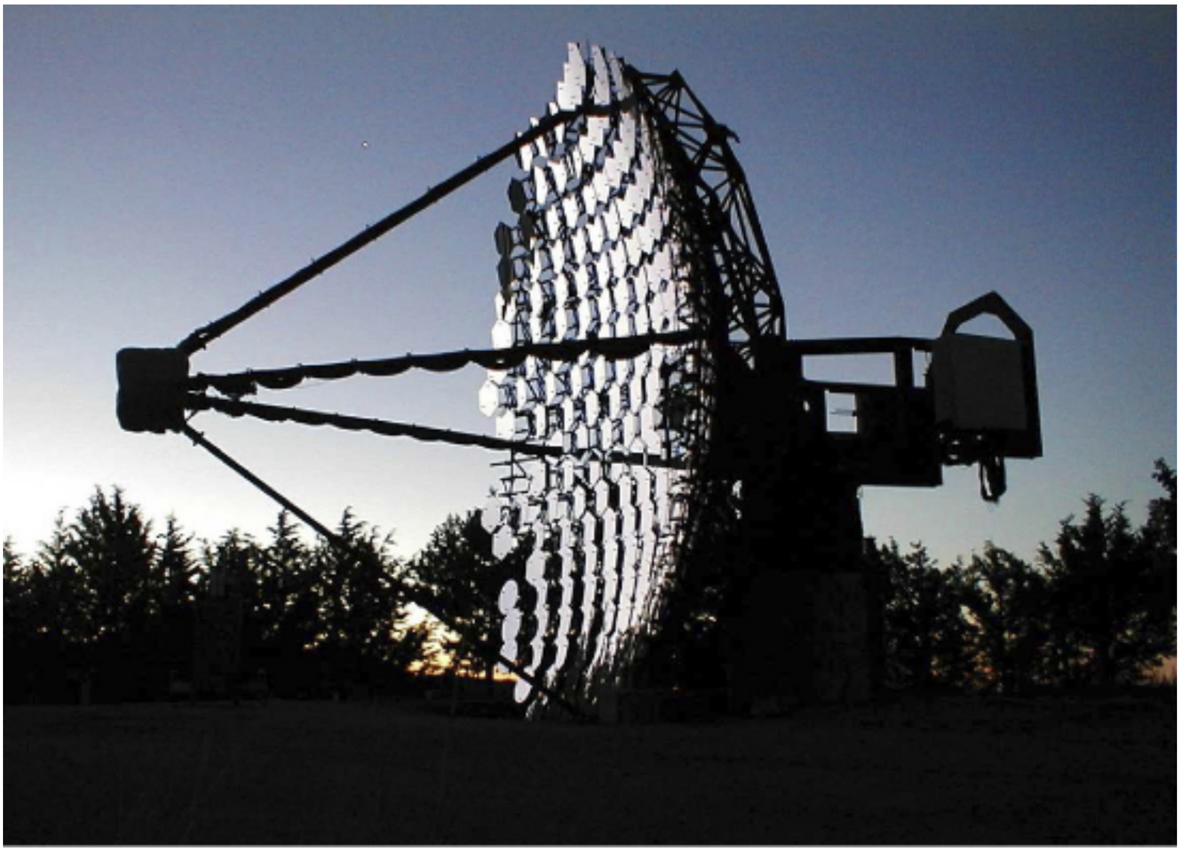

Figure 2.2: The Whipple 10 m Telescope on Mt. Hopkins in southern Arizona, picture from Kildea et al. (2007). The telescope is shown at stow position, and the tessellated mirrors of the reflector can be clearly seen from this angle.

from the optic axis have different transit times to the focal plane. For the Whipple telescope, this spread of times was ~ 6.5 ns.

The flash of Cherenkov light from EAS is lasts only ~2 – 5 ns, and so a camera built to detect such light must have a very fast response time. PMTs were chosen as the most suitable sensors due to their typical response time of $\sim 1 - 2$ ns and relatively low noise. Light concentrating cones were also installed in front of the PMTs to improve the light collection efficiency of the camera. The cones helped reflect photons that would otherwise be lost in the inter-pixel spacing onto the sensitive area of the PMTs. They also provided some protection against night sky background (NSB) light, and the telescope's environment. Typical improvements in efficiency of $\sim 30\% - 40\%$ were achieved by the cones.

2.1.2 VERITAS

The Very Energetic Radiation Imaging Telescope Array System (VERITAS) (Holder et al., 2008) is located at the base camp (~ 1.27 km above sea level) of the Fred Lawrence Whipple Observatory on Mt. Hopkins, and is the successor of the Whipple 10 m Telescope. It is a stereoscopic

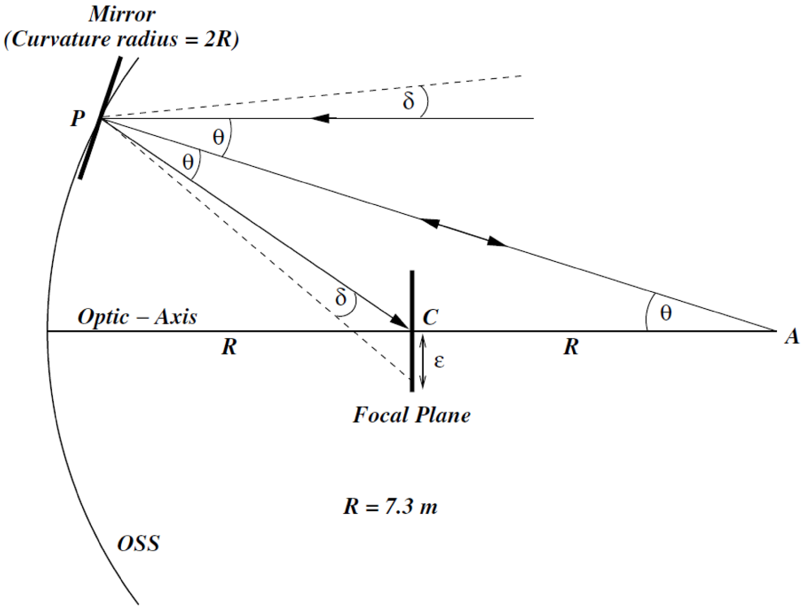

Figure 2.3: Schematic of the Davies-Cotton reflector design (Kildea et al., 2007). Light arriving parallel to the optic axis is focused in the centre of the focal plane. Light arriving off-axis at an angle δ is displaced on the focal plane.

imaging array consisting of four 12 m diameter telescopes, the design of which is based on that of the Whipple telescope.

Physical design Each individual telescope is of Davies-Cotton design, with a 12 m diameter reflector of focal length 12 m composed of 350 tessellated hexagonal mirror facets, giving a total reflecting area of $\sim 107\,\mathrm{m}^2$. Increasing the $f/$number of the VERITAS telescopes compared to the Whipple 10 m Telescope reduces the spread of light ray arrival times to ~ 4 ns (Cogan, 2005). A 499-pixel PMT camera is located at the focal plane. A plate of light concentrating cones is placed in front of the PMTs, again reducing the dead space between pixels. Each camera has a $3\overset{\circ}{.}5$ FoV, composed of pixels of diameter $\sim 0\overset{\circ}{.}15$. The array operates in the energy range $\sim 0.1 - 50$ TeV, with an energy resolution of $\sim 15\%$ at high energies.

Trigger system VERITAS employs a three-tier trigger system to reduce the rate of background events recorded (Weinstein, 2008). The first tier of the system, L1, operates at the single pixel level. Each pixel is routed directly to a custom-built programmable constant fraction discriminator (CFD). This produces a 10 ns output pulse once the discriminator threshold has been exceeded. When the CFD triggers, the pulse is sent to the second tier, L2. This tier acts as a pattern trigger at the individual telescope level. The L2 system requires L1 triggers from three adjacent pixels within a coincidence window of ~ 6 ns to trigger in the standard setup. This preferentially selects compact images and reduces the rate of triggers due to random fluctuations of the NSB. The final tier, L3, is an array-wide trigger that receives information from L2 system. It primarily rejects local muons by requiring the presence of an L2 trigger from multiple telescopes in the array within a coincidence window of 50 ns.

Data acquisition system A multi-stage data acquisition chain continuously digitises the analogue PMT signals, constructs telescope events, and compiles information from each telescope into array-wide data (Hays, 2008). At the heart of this system are custom 500 MSPS flash analogue to digital converters (FADCs), which sample the PMT pulse every 2 ns. FADCs are more advantageous than simple charge integrating ADCs as they allow the application of some signal processing. For example, the charge integration window can be dynamically placed in the analysis, improving the signal-to-noise ratio of individual PMTs, leading to a reduction in the energy threshold of the entire system (Cogan, 2008).

The digitised PMT signal is stored in a ring buffer until an L3 trigger is received. When this trigger arrives, the system reads out a section of the buffer, typically 24 samples (48 ns), for each PMT signal. The data from the FADCs are sent to the *Event Builder* which combines the signals into telescope-level events. These events are then sent to the *Harvester* which combines all the telescope-level information together with supplementary information from the L3 system such as event number and a GPS time stamp. In addition to the triggering, readouts of the FADC memory buffers are requested by the array trigger periodically during observations, and are used to asses the baseline values, known as the “pedestals”. These pedestal events are included as normal events in the data, and are distinguished simply by an event type code.

Atmospheric monitoring VERITAS, in contrast to the Whipple 10 m Telescope, has a wide variety of atmospheric monitoring equipment on site that operates in parallel with the array. Three far infrared pyrometers (FIRs) measure the sky temperature during observations to monitor for clouds, which are observed as an increase in temperature. Two of these FIRs are mounted on the OSSs of different telescopes, in order to monitor the sky in the direction that the telescopes are pointing. The third FIR always points at zenith, thus monitoring conditions directly overhead. An optical CCD all-sky-monitor supplies a live feed of the entire sky to the control room, allowing clouds or anomalous sources of light that may affect the array’s behaviour, such as airplanes for example, to be noted. A humidity sensor and anemometer continuously monitor ambient weather conditions at the site. In 2012, a LIDAR system was installed at the site. This measures the distribution and concentration of scattering agents such as dust, haze, fog, or clouds in the atmosphere by emitting short pulses of laser light and detecting the back-scattered light from these pulses as function of time. The measurements made by these instruments provide an accurate monitor of the external conditions affecting the data quality for a particular observation.

Performance VERITAS entered full four-telescope array operation in 2007, and through a number of alterations to the array configuration since then, its sensitivity has been improved over the last six years. Figure 2.4 shows the V4 and V5 configurations of VERITAS, before and after the relocation of T1 in summer 2009. This change put the array in a more uniform quadrilateral formation, with similar distance ($\sim 100\,\mathrm{m}$) between adjacent telescopes. This configuration provides improved background rejection capabilities, increasing the overall sensitivity of VERITAS by $\sim 30\%$. As a result, the time required to detect a source of 1% Crab Nebula flux at the $5\,\sigma$ level decreased from 48 hours to 30 hours (Perkins et al., 2009). In summer 2012, the cameras of VERITAS were overhauled, and the pixels were replaced with new high quantum efficiency PMTs with the aim of improving the sensitivity of the array at lower energies. This constitutes the V6 configuration, and remains the current status of VERITAS.

Figure 2.5 shows a comparison of the effective areas of VERITAS in the V5 and V6 configurations. The effective area is improved at low energies for the V6 array, which was the intended result of the camera upgrade. The effective area still plateaus at $\sim 10^5\,\mathrm{m}^2$ above $\sim 300\,\mathrm{GeV}$. Figure 2.6 shows the sensitivity of VERITAS in the V5 and V6 configurations. The increase in effective area for V6 is also apparent in the sensitivity curve, which extends to lower energies than that of the V5 array.

2.2 Satellite detectors

Due to the absorption of X-ray to γ-ray energy photons by the Earth's atmosphere, instruments designed to directly detect such energies must be placed on satellites. In this thesis, the data from three space-based observatories was used. Details of the relevant scientific instruments on board these satellites are given in the following sections.

2.2.1 Fermi Gamma-ray Space Telescope

The *Fermi* Gamma-ray Space Telescope was launched into a low-earth orbit in June 2008. The mission consists of two instruments; the Large Area Telescope (LAT) (Atwood et al., 2009) which uses a pair-production detection mechanism, and the Gamma-ray Burst Monitor (GBM) (Meegan et al., 2009) which comprises 14 scintillation detectors. The primary observation mode of *Fermi* is sky-survey mode, in which the satellite rocks about the zenith. Coupled with the $2.4\,\Omega$ FoV of the LAT, this motion maximises the LAT's sky-coverage while maintaining near-uniform

Figure 2.4: The top panel shows the V4 configuration of VERITAS, prior to the relocation of T1. The V5 configuration is shown in the bottom panel for comparison, where the array forms a more uniform quadrilateral. This configuration provides improved background rejection capabilities, increasing the overall sensitivity of VERITAS by $\sim 30\%$. The time required to detect a source of 1% Crab Nebula flux at the $5\,\sigma$ level decreased from 48 hours to 30 hours.

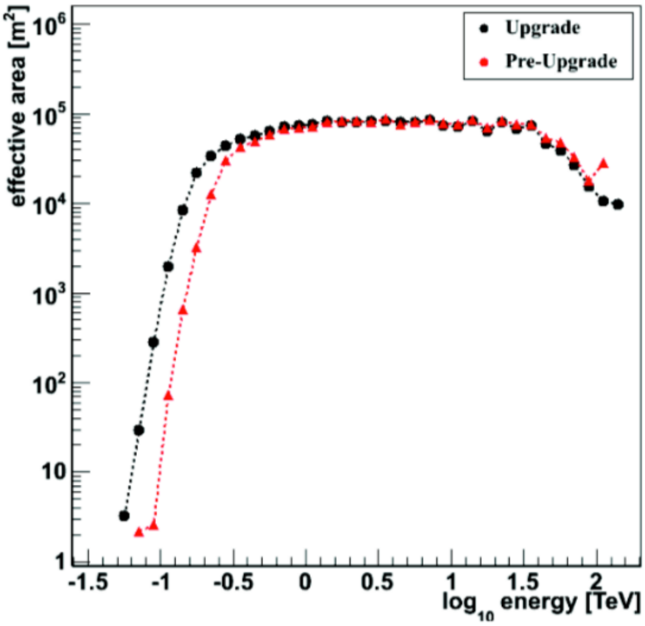

Figure 2.5: Comparison of simulated VERITAS effective areas for the V5 (red) and V6 (black) configurations as a function of primary γ-ray energy. Figure taken from Kieda & The VERITAS Collaboration (2013).

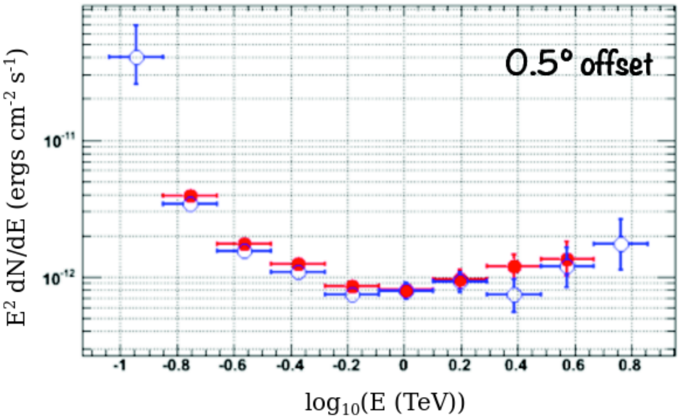

Figure 2.6: Sensitivity of VERITAS in the V5 configuration (red) and the V6 configuration (blue) for the standard wobble offset of half a degree. This sensitivity curve is calculated from observations of the Crab Nebula.

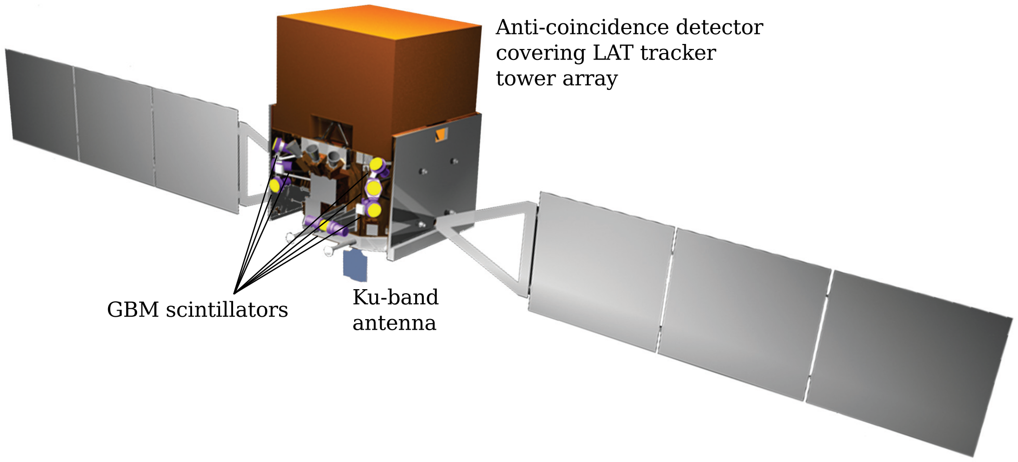

Figure 2.7: The *Fermi* satellite, showing the LAT covered by the anti-coincidence detector, and half of the GBM scintillators. (Image credit: NASA/GLAST/Sonoma State University/Aurore Simonnet.)

exposure. The position of the detectors on the spacecraft body is shown in Figure 2.7. LAT data was analysed in this dissertation to provide a complete picture of the high-energy spectrum of an AGN (Chapter 5).

LAT The LAT is a pair production telescope, sensitive above $\sim 20\,\mathrm{MeV}$, and is the primary instrument on board the *Fermi* satellite. It consists of three main components; the converter, the tracker and the calorimeter. The converter comprises 16 layers of tungsten in which incident photons pair produce. The converter is interwoven with single-sided silicon strip detectors that constitute the tracker, allowing the measurement of the positions of the charged particles in each layer. The calorimeter is positioned beneath the converter/tracker, and measure the energy of the particle shower which results from the electron/positron pair. For the effective rejection of

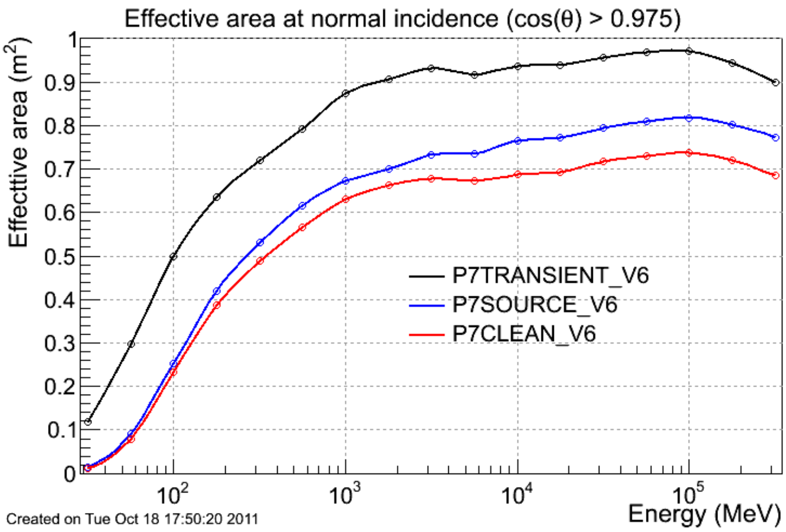

Figure 2.8: Effective area of the LAT to photons at normal incidence as a function of photon energy for the *P7_V6* instrument response functions. The blue curve corresponds specifically to the response functions used in the LAT analysis presented in this thesis. Figure from Rando et al. (2011).

cosmic rays, the system is covered with an anti-coincidence shield.

The effective area of the LAT using the *P7_V6* instrument response functions (the *P7SOURCE_V6* functions are used in the LAT analysis presented in this thesis) is shown in Figure 2.8. At $\sim 300\,$GeV, the effective area of the LAT is $\sim 0.8\,$m^2. This is vastly smaller than the effective area of VERITAS at the same energy ($\sim 10^5\,$m^2).

The differential sensitivity of the LAT is shown in Figure 2.9. The VERITAS and LAT energy ranges overlap from ~ 100 to $300\,$GeV. At $\sim 100\,$GeV, the LAT is slightly more sensitive than VERITAS, but at $\sim 200\,$GeV, VERITAS is more sensitive than the LAT by about an order of magnitude.

2.2.2 Rossi X-ray Timing Explorer

The *Rossi* X-ray Timing Explorer (RXTE) operated from a low-earth circular orbit from December 1995 to January 2012. It carried three instruments on board; the Proportional Counter Array (PCA), the High-Energy X-ray Timing Experiment (HEXTE), and the All-Sky Monitor (ASM) (Bradt et al., 1993). The large effective area and broad-band sensitivity of its three instruments made it particularly useful for measuring the timescales of intensity variations of sources, and also for determining broad-band spectra from high-energy sources. PCA and HEXTE together constituted a single, powerful telescope, the large area and low background of which provided good sensitivity to weak sources. The ASM scanned most of the sky every 1.5 hours

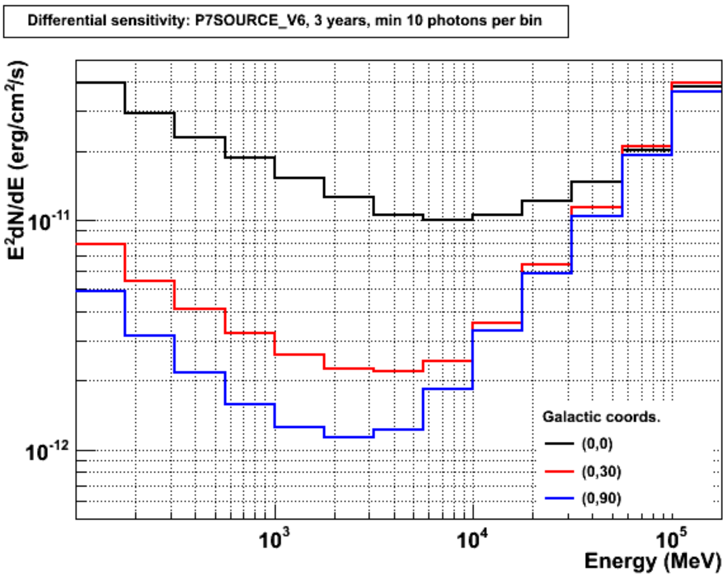

Figure 2.9: The differential sensitivity of the LAT for three years using the *P7SOURCE_V6* instrument response functions. It is calculated assuming a point source with a power-law spectrum of index -2. The curves correspond to three different locations, ranging from the galactic centre (black) to the pole (blue). Contamination from the multitude of galactic sources causes a drastic reduction in sensitivity for sources in the galactic plane. Figure from Rando et al. (2011).

to monitor the intensity and spectra of the brightest ~ 75 sources in the sky. Figure 2.10 shows the different instruments on the RXTE satellite. In this dissertation, PCA data was analysed to provide the X-ray component of a multiwavelength spectrum of an AGN (Chapter 5).

PCA The PCA on board RXTE consisted of five large, nearly identical, detectors known as Proportional Counter Units (PCUs). Each PCU had three xenon gas-filled signal detection layers, with anti-coincidence side and rear chambers, and a propane top layer. PCA was sensitive over the energy range $2 - 60\,$keV with an energy resolution of 18% at $6\,$keV. The X-ray shielded hexagonal tubular collimators provided a 1° full-width half-maximum FoV.

2.2.3 Swift

Swift is a multiwavelength observatory that was launched into a low-earth circular orbit in November 2004. Its primary scientific objectives relate to gamma-ray burst astronomy (Gehrels et al., 2004), but the satellite also provides rapid follow-up observations of all types of high-energy transients. *Swift* consists of three instruments; the Burst Alert Telescope (BAT) (Barthelmy et al., 2005) which identifies gamma-ray bursts and determines their location to within a few arcseconds, the Ultra-Violet/Optical Telescope (UVOT) (Roming et al., 2005) which has a limiting sensitivity of 24th magnitude in 10^3 seconds and $0.3''$ position accuracy, and the X-ray

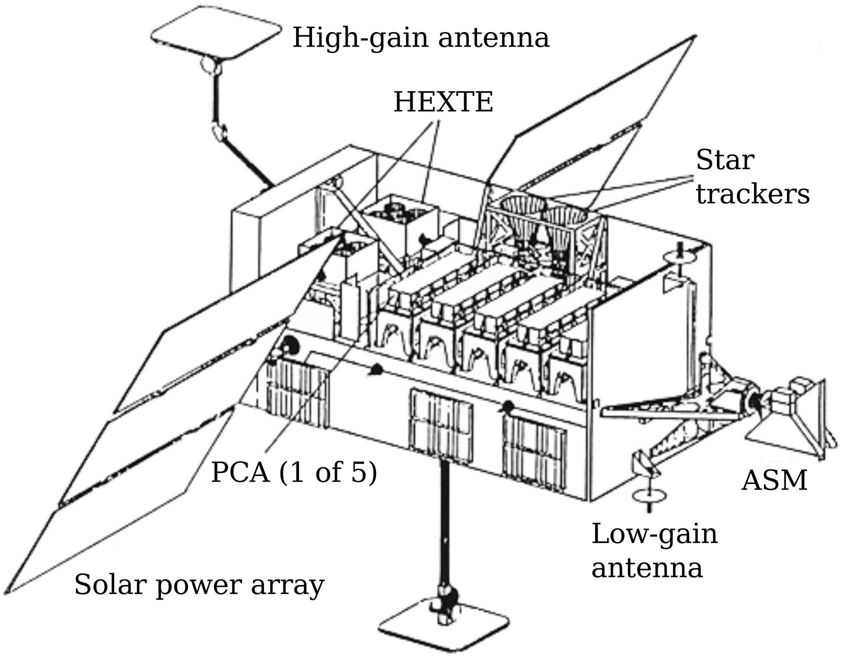

Figure 2.10: Diagram of the RXTE spacecraft, showing the arrangement of the different instruments on board (Bradt et al., 1993).

Telescope (XRT) (Burrows et al., 2005). Figure 2.11 shows the configuration of the instruments on the spacecraft. In this dissertation, XRT data was used to compliment other multiwavelength observations of an AGN (Chapter 5).

XRT The XRT on board *Swift* is a grazing incidence telescope (Wolter type 1) with a FoV of $23.6' \times 23.6'$ and an energy range of $0.2 - 10\,\mathrm{keV}$. It has an effective area of $> 120\,\mathrm{cm}^2$ at $1.5\,\mathrm{keV}$ and an angular resolution of $18''$. It has a detection sensitivity of 2×10^{-14} ergs cm^{-2} s^{-1} in 10^4 seconds. The XRT operates in an auto-exposure mode, adjusting the CCD readout mode automatically based on the source brightness to maximise the science return of the observation.

2.3 Bibliography

Atwood, W. B., Abdo, A. A., Ackermann, M., et al., 2009; 'THE LARGE AREA TELESCOPE ON THE FERMI GAMMA-RAY SPACE TELESCOPE MISSION'. *The Astrophysical Journal*, vol. 697(2):1071

Barthelmy, S. D., Barbier, L. M., Cummings, J. R., et al., 2005; 'The Burst Alert Telescope

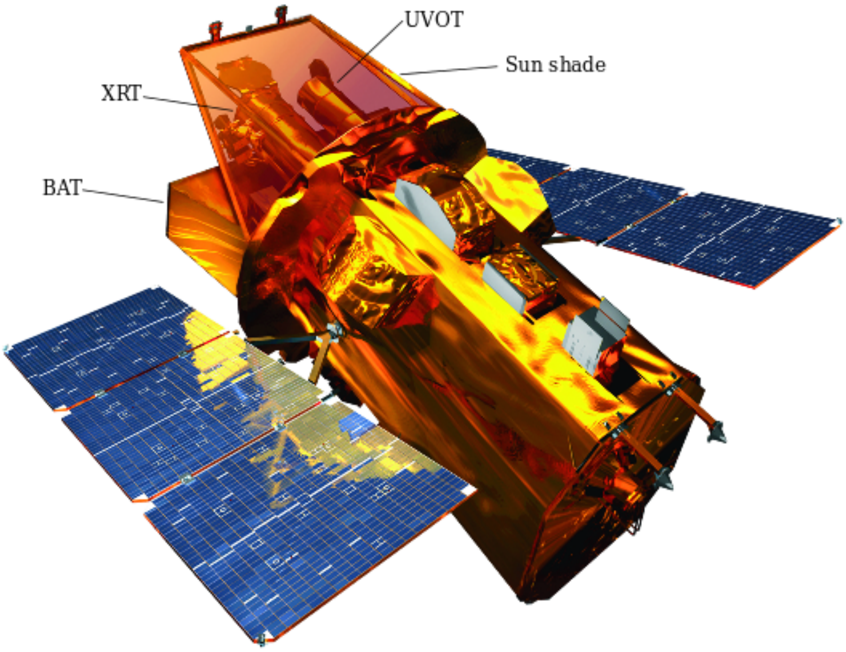

Figure 2.11: Physical configuration of instruments on board the *Swift* satellite. (Image credit: NASA E/PO, Sonoma State University (GSFC & Sonoma State University, 2012).)

(BAT) on the SWIFT Midex Mission'. *Space Science Reviews*, vol. 120(3-4):143

Bradt, H. V., Rothschild, R. E., Swank, J. H., 1993; 'X-ray timing explorer mission'. *Astronomy and Astrophysics Supplementary Series*, vol. 97:355

Burrows, D. N., Hill, J. E., Nousek, J. A., et al., 2005; 'The Swift X-Ray Telescope'. *Space Science Review*, vol. 120:165

Cogan, P., 2005; 'An Overview of the Veritas Prototype Telescope and Camera'. *Astrophysics and Space Science*, vol. 297(1-4):275

—, 2008; 'Analysis of Flash ADC data with VERITAS'. In 'Proceedings of the 30th International Cosmic Ray Conference', vol. 3, 1369. Universidad Nacional Autónoma de México, Merida, Mexico

Fegan, D. J., 1997; 'Gamma/hadron separation at TeV energies'. *Journal of Physics G: Nuclear and Particle Physics*, vol. 23(9):1013

Gehrels, N., Chincarini, G., Giommi, P., et al., 2004; 'The Swift GammaRay Burst Mission'. *The Astrophysical Journal*, vol. 611(2):1005

GSFC, Sonoma State University, 2012; 'Swift multimedia gallery'. http://swift.sonoma.edu/resources/multimedia/images/index.html

Hays, E., 2008; 'VERITAS Data Acquisition'. In 'Proceedings of the 30th International Cosmic Ray Conference', vol. 3, 1543. Universidad Nacional Autónoma de México, Merida, Mexico

Holder, J., Acciari, V. A., Aliu, E., et al., 2008; 'Status of the VERITAS Observatory.' *Proceedings of the 4th International Meeting on High Energy Gamma-Ray Astronomy*, vol. 1085(1):657

Jelley, J. V., 1958; *Cerenkov radiation and its applications*. Pergamon Press, London

Kieda, D. B., The VERITAS Collaboration, 2013; 'The Gamma Ray Detection sensitivity of the upgraded VERITAS Observatory'. In 'Proceedings of the 33rd International Cosmic Ray Conference', 4. Rio de Janeiro, Brazil

Kildea, J., Atkins, R. W., Badran, H. M., et al., 2007; 'The Whipple Observatory 10 m gamma-ray telescope, 1997 - 2006'. *Astroparticle Physics*, vol. 28(2):182

Meegan, C., Lichti, G., Bhat, P. N., et al., 2009; 'THE FERMI GAMMA-RAY BURST MONITOR'. *The Astrophysical Journal*, vol. 702(1):791

Perkins, J. S., Maier, G., The VERITAS Collaboration, 2009; 'VERITAS Telescope 1 Relocation: Details and Improvements'. In 'Proceedings of the Fermi Symposium',

Rando, R., Charles, E., Digel, S. W., et al., 2011; 'Fermi LAT Performance'. `http://www.slac.stanford.edu/exp/glast/groups/canda/archive/pass7v6/lat\_Performance.htm`

Roming, P. W. A., Kennedy, T. E., Mason, K. O., et al., 2005; 'The Swift Ultra-Violet/Optical Telescope'. *Space Science Reviews*, vol. 120(3-4):95

Schmidt, F., 2014; 'Corsika shower images'. `http://www.ast.leeds.ac.uk/~fs/showerimages.html`

Schönfelder, V. (Ed.) , 2001; *The Universe in Gamma Rays*. Springer-Verlag

Weinstein, A., 2008; 'The VERITAS Trigger System'. In 'Proceedings of the 30th International Cosmic Ray Conference', vol. 3, 1539. Universidad Nacional Autónoma de México, Merida, Mexico

CHAPTER 3

Data analysis

VHE γ-ray data from VERITAS and the Whipple 10 m Telescope constitute the basis of all the work presented in this dissertation. Chapter 5 presents a multiwavelength blazar study in which data from other instruments such as X-ray and γ-ray satellites were also analysed to compliment the VHE γ-ray data. In Chapter 7, a Bayesian block algorithm is used to identify and characterise variability in a long-term study of the VHE emission from the Crab Nebula.

This chapter describes the analysis chains for VERITAS and the Whipple 10 m Telescope in some detail, and also provides an overview of the analysis techniques for the supporting data presented. A detailed description of the Bayesian block algorithm is also given here.

3.1 Whipple 10 m Telescope analysis chain

The Cherenkov light from EAS is detected as an ellipse for electromagnetic showers, and as less regular shapes for hadronic showers. As a result, the γ-ray-initiated EAS can be distinguished from isotropic background particle-initiated showers by examining the shape of the images produced (Hillas, 1985). The parameters describing the ellipse are divided into two classes. Shape parameters characterise the size of the ellipse (and whether the image is, in fact, elliptical) and orientation parameters describe the alignment of the image in the camera. Table 3.1 outlines these parameters which are also illustrated schematically in Figure 3.1.

The analysis of the air shower images is essentially a two-step process. In the first step, the images are processed to remove hardware and Night Sky Background (NSB) effects. This type

Shape parameters	Description
`size`	Total integrated light content of the image in ADC counts.
`length`	The RMS spread of light along the major axis of the ellipse.
`width`	The RMS spread of light along the minor axis of the ellipse.
Orientation parameters	Description
`distance`	The distance from the centroid of the image to the centre of the field of view of the camera (which is aligned with the source).
`miss`	The perpendicular distance between the major axis of the image and the centre of the field of view of the camera.
α	The angle between the major axis of the image and the distance line drawn from the centre of the camera to the centroid of the image.
Extra parameters	Description
`azwidth`	The RMS spread of light perpendicular to the distance line. This is both a shape and orientation parameter.

Table 3.1: Overview of the original ellipse parameters of a γ-ray image.

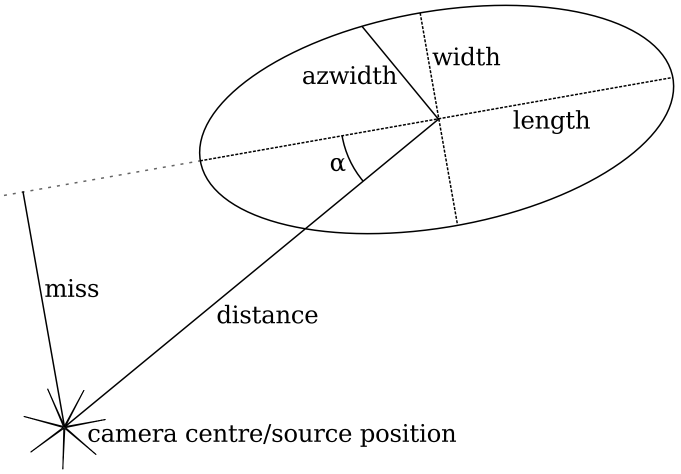

Figure 3.1: Schematic representation of the ellipse parameters for describing γ-ray images.

of processing, or conditioning, consists of pedestal subtraction, suppression of noise-dominated pixels, and camera flat-fielding. In the second step, the images are fit and the γ-ray images are selected based on parameter cuts.

Pedestals The analog-to-digital (ADC) pedestals and their RMS deviations are calculated directly from the data. The pedestal itself is an artificial negative offset that is added to the analog PMT signal. The telescope was triggered artificially at regular intervals (1 Hz) during observing runs to accumulate pedestal events for each observing region to allow this direct calculation. The charge in each PMT is obtained by subtracting the pedestal value for that pixel from the total charge.

Sky noise Two thresholds are defined for selecting pixels that contribute to the image of the Cherenkov light and rejecting those due to background fluctuations. The picture threshold is the multiple of the RMS pedestal deviation that a pixel must exceed to be considered part of the image. The boundary threshold is the multiple which pixels adjacent to picture pixels must exceed to remain in the image as part of the boundary. The picture and boundary pixels alone make up the image, and all other pixels are set to zero. The picture and boundary thresholds are set to 4.25 and 2.25 respectively in the analysis presented in Chapter 7.

Flat-fielding The recorded pixel signals are scaled by their relative gains prior to the image analysis to account for efficiency differences in the PMTs. Relative gain information was collected in nightly calibration runs taken with a nitrogen flash lamp uniformly illuminating the PMTs with a ~ 750 Hz pulse train of very short duration blue flashes (Kildea et al., 2007).

Parameterisation Conditioned data are analysed using a second-moment parameterisation technique. This characterises the shape and orientation of each image in the camera as illustrated in Figure 3.1.

Event selection Selection criteria that the exploit the differences in the images of γ-rays and background cosmic rays are used to extract the γ-ray events while suppressing the cosmic ray background. The set of parameter cuts that achieve this are motivated by simulations but optimised on a real data set. Historically, observations of the Crab Nebula have been used for this optimisation.

These steps constitute the "Supercuts" image analysis procedure presented in Punch et al. (1991); Reynolds et al. (1993). This remained the standard analysis chain for Whipple 10 m Telescope data for the rest of its lifetime. This multiparameter γ-ray image selection process was developed to provide a more efficient treatment of events than what had previously been used. In the Supercuts analysis, the `azwidth` cut was discarded in favour of a simple `width` cut to allow complete separation of the shape and orientation elements. The shape and orientation parameters for image selection are optimised on a subset of real data rather than being predetermined by shower simulations.

The remaining background consists of cosmic ray events that are difficult to distinguish from γ-ray events. This background cannot be further reduced, and so must be estimated. For each source observation, a corresponding blank sky observation of the same duration is taken. This is performed at comparable azimuth and zenith angles to the source observation. This is referred

Parameter	Value
`size1` (dc)	30
`size2` (dc)	30
`size3` (dc)	0
`length` (°)	$0.13 - 0.25$
`width` (°)	$0.05 - 0.12$
`distance` (°)	$0.4 - 1.0$
`length/size`	$< 4 \times 10^{-4}$
α (°)	< 15

Table 3.2: Cut parameters used in the analysis of Whipple 10 m Telescope data in this dissertation. The *Supercuts 2000* cut levels were appropriate for all seasons of data. In this table, the parameters `size1`, `size2`, and `size3` refer to the signal size in the pixel containing the highest, second highest, and third highest signal in an image respectively.

to as *paired mode* observations as it involves pairing observations of the source (the ON region) with observations of an appropriate background (the OFF region).

The Whipple 10 m Telescope analysis presented in Chapter 7 covers 10 years of observations, from 2000 − 2010. The cut levels known as *Supercuts 2000* (Petry, 2001) were used for the analysis of this data set. These cuts were developed on the basis of Crab Nebula observations during the 1999 − 2000 observing season. In addition to the parameters already mentioned, a selection based on the compound parameter `length/size` was introduced to reduce the background of local single muon events. Table 3.2 shows the *Supercuts 2000* cut levels.

3.2 The VERITAS data analysis

Advanced analysis techniques such as maximum likelihood methods for spectral analysis and boosted decision trees for γ/hadron separation are currently in development. However, the analysis of VERITAS data presented in this thesis follows a very similar methodology to the analysis of Whipple 10 m Telescope data. The main difference is that VERITAS can employ a stereoscopic reconstruction of events by using the data recorded in all four telescopes of the array for a single event. This has the advantage of improving background rejection, particularly of local atmospheric muons. The shower direction reconstruction is also improved. Regardless, the image conditioning performed on VERITAS data remains akin to that performed on Whipple data.

Pedestals The telescopes are externally triggered at regular intervals to accumulate a set of pedestal events for each observation. These events are used as the baseline measurement of the behaviour of each PMT in the absence of Cherenkov light. The charge in each pixel is determined in the analysis by subtracting the pedestal value for the pixel from the total charge recorded by that pixel.

Flat-fielding The pixel signals are scaled by a correction for their relative gains prior to image analysis to account for variations in PMT behaviour in the camera. The relative gain information is collected nightly in short calibration runs taken with a pulsed UV LED uniformly illuminating the camera (Hanna et al., 2010).

Sky noise Once the pixel charges have been calculated, noise pixels are removed from each image. Picture and boundary thresholds are defined as in the Whipple analysis and used to select pixels that contribute to the image of the shower. For the VERITAS analysis the picture and boundary thresholds are chosen to be 5 and 2.5 respectively. If a picture pixel does not have any neighbours that survive the cleaning process, this pixel is also removed from the image.

Parameterisation Conditioned images are analysed in terms of the `size`, `length`, `width` and `distance` parameters shown in Figure 3.1.

Event pre-selection Some selection criteria are applied to the images before stereoscopic reconstruction is undertaken. These cuts include requiring a minimum number of image and boundary pixels, a minimum `size` value, and a maximum `distance` value.

Event reconstruction The reconstruction of the direction of an event is based on Algorithm 1 in Hofmann et al. (1999). The images from all telescopes with data for a particular event are superimposed in a common coordinate system, the camera plane. The intersection point of the major axes of all the ellipses is the shower direction in the camera plane. The intersection of all pairs of major axes are weighted by the angle between the axes, the `size` of the images, and the `width/length` ratio of each image to give more weight to brighter, more elongated image pairs in the calculation. The location of the shower core is computed (Aharonian et al., 1997), as this allows determination of the impact parameter - the distance between the shower core and a given telescope. The height of the shower maximum H_{max} is also calculated at this point. The shower maximum is defined as when the EAS contains the maximum number of Cherenkov-emitting particles, and its height contains certain information about the nature of the primary particle that initiated the shower. It is therefore useful for suppressing background cosmic ray events.

Energy reconstruction The number of Cherenkov photons in a γ-ray initiated EAS is proportional to the energy of the γ-ray. This means that the energy of the γ-ray can be related to the `size` of the images of an event. The `size`, in turn, is dependent on the azimuth angle and zenith angle of the observation, impact parameter of the shower and the NSB level. Monte Carlo simulations of γ-rays covering this large parameter space are performed in advance, and their results stored in lookup tables. The lookup tables for the appropriate observing parameters are consulted for each event to estimate the energy of the primary γ-ray.

γ-ray selection Once all the reconstruction is complete, γ-ray events are extracted while suppressing the cosmic ray background by cutting on the image shape and the arrival direction of the events. The stereoscopic image shape is parameterised in terms of *mean scaled width* (MSW) and *mean scaled length* (MSL) parameters (Konopelko et al., 1999). These are the average of the `widths` and `lengths` of the γ-ray ellipses in each telescope scaled by an expected value based on Monte Carlo simulations. A cut on the arrival direction θ is also applied, where θ is the angle on the sky between the source position and the reconstructed shower direction.

There is still a background of γ-ray like cosmic ray events that cannot be eliminated, and so must be estimated. Two models are generally employed for this purpose, the reflected regions model (Aharonian et al., 2001) and the ring background model (Berge et al., 2007). Figure 3.2 shows a schematic representation of both methods of background estimation. The statistical significance S of a source can then be calculated by comparing the number of events in the source selection region N_{on} with the number of events in the background region N_{off}. The significance is calculated using Equation 17 in Li & Ma (1983):

$$S = \sqrt{2}\left\{N_{\text{on}} \ln\left[\left(\frac{1+\alpha}{\alpha}\right)\left(\frac{N_{\text{on}}}{N_{\text{on}}+N_{\text{off}}}\right)\right] + N_{\text{off}} \ln\left[(1+\alpha)\left(\frac{N_{\text{off}}}{N_{\text{on}}+N_{\text{off}}}\right)\right]\right\}^{\frac{1}{2}}, \quad (3.2.1)$$

where α is the ratio between the areas of the source selection region and the background selection region.

VERITAS has been operated in three different configurations since 2007. The Old Array configuration refers to the initial 4-telescope setup. The New Array configuration refers to the array after the relocation of T1 in the summer of 2009. The Upgraded Array configuration refers to VERITAS as it is now, following the camera upgrade in summer 2012. Cut levels are optimised for a range of different source spectra (soft, medium, hard and loose) and the different array configurations. Table 3.3 shows the cut levels used in this dissertation. In general, medium cuts were used, but loose cuts were employed in Chapter 6.

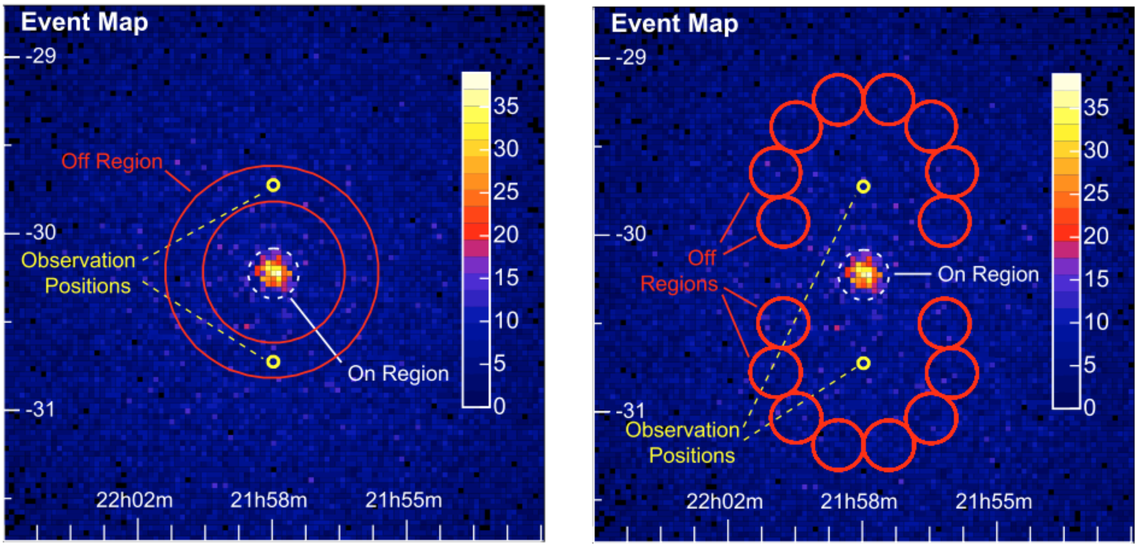

Figure 3.2: Schematic representation of the the ring background model (left) and the reflected regions model (right), taken from Berge et al. (2007). In the ring background model, an annulus with inner radius larger than the source selection region and centred on the source position is used to extract an estimate of the background. The reflected regions model is used for *wobble mode* observations, the normal mode of operation for VERITAS. In this observing mode, the source position is offset from the centre of the FoV of the telescope by a set amount. In this case, regions offset from the centre of the FoV and displaced from the source selection region can be used to determine the background.

Parameter	Old Array (medium)	New Array (medium)	Upgraded Array (medium)	Upgraded Array (loose)
`size`	> 400	> 400	> 700	> 400
`distance` (°)	< 1.43	< 1.43	< 1.43	< 1.43
`NTubes`	> 5	> 5	> 5	> 5
MSW	$0.05 - 1.1$	$0.05 - 1.1$	$0.05 - 1.1$	$0.05 - 1.15$
MSL	$0.05 - 1.3$	$0.05 - 1.3$	$0.05 - 1.3$	$0.05 - 1.4$
$H_{\text{max}}(km)$	> 7	> 7	> 7	> 7
θ (°)	< 0.1	< 0.1	< 0.1	< 0.17

Table 3.3: Cut parameters used for the VERITAS analyses presented in this dissertation.

The Monte Carlo simulations used to determine the instrument response functions of VERITAS consist of modelling the EAS development in the atmosphere, including the emission of Cherenkov photons, and then modelling the detector response to these Cherenkov photons. Once complete, the simulations are analysed in the same manner as real data to obtain the instrument response functions necessary for flux reconstruction. From these simulations, the overall systematic uncertainty on the flux is estimated as $\sim 40\%$, and the systematic uncertainty on the spectral index as ~ 0.3.

3.3 Fermi-LAT data analysis

The *Fermi*-LAT data presented in Chapter 5 was analysed using an unbinned likelihood analysis. This is the preferred method of analysing LAT data except in the instance of long time bins, bright background sources, or long-term spectral or spatial analyses. In these cases, a binned analysis would be recommended instead.

The LAT analysis of a known source is essentially a four-step process (FSSC, 2013; Abdo et al., 2009). First the data must be selected. A substantial spatial region around the source being analysed must be used due to the overlapping point spread functions of nearby sources. Next, a model of the region of interest must be created. This model includes the position of the source to be analysed, the positions of nearby sources, a model of the diffuse emission, the functional form of the spectra of the sources present, and the values of the spectral parameters. In the third step, quantities such as the livetime and exposure, that are used as part of the likelihood calculation, can be precomputed. It is not strictly necessary that this is done in advance, but as the likelihood is computed many times during the fitting process, having these numbers already available greatly speeds up the process. Finally, in the last step, the fit is actually performed. The spectral parameters of the sources included in the model must be fit simultaneously. The likelihood is repeatedly calculated for different trial parameter sets until a value sufficiently close to the maximum is found.

The likelihood L is the product of the probabilities of observing the detected counts in each bin. The probability of detecting n_i counts in the i^{th} bin is given by

$$p_i = m_i^{n_i} \exp\left(-m_i\right) / n_i! \tag{3.3.1}$$

where m_i is the expected number of counts in the i^{th} bin. It is a function of the source model, and so will be different for different models. In the unbinned analysis, where the bin sizes are infinitesimally small, n_i becomes either 0 or 1. In this case, L has the form

$$L = \exp\left(-N_{\text{exp}}\right) \prod_i m_i, \tag{3.3.2}$$

where N_{exp} is the sum of m_i, the total number of counts that the source model predicts should have been detected.

The Test Statistic TS is used as a measure of the strength of a detection. It is defined as

$$TS = -2 \ln \left(\frac{L_{\text{max,0}}}{L_{\text{max,1}}} \right), \tag{3.3.3}$$

where $L_{\text{max,0}}$ is the maximum likelihood value for the null hypothesis model (i.e., no source is present) and $L_{\text{max,1}}$ is the maximum likelihood value for a model including an additional source at the specified location. A larger TS indicates that the null hypothesis is incorrect, and can be quantified. The detection significance in terms of σ is approximately equal to $\sqrt{TS}$.

In the *Fermi*-LAT analysis undertaken in this dissertation, *ScienceTools-v9r23p1* was used with the *P7SOURCE_V6* instrument response functions. The source under investigation is a known source. Events were extracted from a region of interest (ROI) of radius 10° centered on the source coordinates. Events from the *diffuse class* with zenith angle $< 100^\circ$ and energy in the range $0.3 - 100\,\mathrm{GeV}$ were selected. *Diffuse class* events suffer least from residual contamination from charged-particle backgrounds. Data taken when the rocking angle of the spacecraft was greater than 52° were discarded to avoid contamination from photons from the Earth's limb.

A background model including all γ-ray sources from the *Fermi*-LAT second source catalog (2FGL) (Nolan et al., 2012) within 12° of interest was created. Remaining excesses in the ROI were modeled as point sources with simple power law spectra. The spectral parameters of sources within the ROI were left free during the minimisation process. The galactic and extragalactic diffuse γ-ray emission as well as the residual instrumental background were included using the recommended model files *gal_2yearp7v6_v0* and *iso_p7v6clean*.

3.4 X-ray analysis

Data from two X-ray instruments were analysed for this dissertation. While the data selection and reduction procedure was different for both telescopes, both analysis packages are part of HEASoft, which encompasses FTools and XANADU (i.e., XSPEC, XIMAGE, etc.). HEASoft version 6.11.1 and XSPEC version 12.7 were used throughout this work.

3.4.1 RXTE PCA data analysis

Data from RXTE PCA is available in a number of different configurations. Each configuration offers some advantage, but *Standard-2 mode* data is automatically used for all observations as it provides all the key information for accurate spectral analysis (RXTE Guest Observer Facility, 2006).

The data is first selected. Good Time Intervals (GTI) are created and applied to the data. GTI exclude periods where the data may be unreliable due to Earth occultation, SAA passage, electron contamination or space craft slewing. The PCUs recording data during the observations must also be identified and selected. Two sets of PCU selections are recommended, one containing all the layers of PCUs that were on during the observations, and one containing just the top layer. Using data from all PCUs provides a better signal-to-noise, but top-layer only data provides more accurate spectral information.

A spectrum and light curve can be extracted from the time intervals of interest in the data. The resultant spectrum is binned by channel (there are 129 channels in *Standard-2 mode* data). If the count rate per PCU exceeds 1000 counts per second, the deadtime of the instrument exceeds 1% and a correction must be applied. To do so, the exposure is adjusted by the amount

$$DCOR = \frac{1}{1 - DTF} \tag{3.4.1}$$

where DTF is the fraction of time spent not collecting data due to deadtime.

Background data files are then created based on models formulated by the PCA instrument team. Background spectra are extracted from these files using the same selections as used for the source data. Finally, the appropriate response matrices are generated. The spectrum can then be analysed and fit in XSPEC by providing the source spectrum file, background spectrum file and response file. There is no usable data below 2 keV, so these should always be excluded, and at high energies, the source spectrum meets the background. Thus, when the spectrum is loaded in XSPEC, the command `‘ignore 0.0-3.0 10.0-**’` is used to ignore channels outside the energy range of interest for this analysis.

3.4.2 Swift XRT data analysis

Swift XRT collects data by cycling through a number of different readout modes during observations of a source. The sequence and exposure time of the modes are automatically scheduled on board based on source brightness (Burrows et al., 2005; Capalbi et al., 2005). Data taken in *photon counting mode* are analysed for the work presented in this dissertation. This mode represents the more traditional operation of an X-ray CCD camera of all the readout modes, providing 2-D position and spectroscopic information.

Data are first processed up to calibrated event lists and images using the script `xrtpipeline` (Page & UK Swift Science Data Centre, 2011). This calibrates the data and then applies screening criteria for the selection of GTI. Images of the source can then be extracted. The images are viewed in *ds9*, and source and background regions are selected and saved for use when extracting spectra and light curves.

Initially, a circular selection region centred on the source is used. A spectrum is then extracted for this region. If the count rate of this spectrum exceeds ~ 0.5 counts per second, the data is likely to suffer from pile-up and an annular source selection region should be used instead. This essentially discards the pixels suffering from pile-up from the analysis. The inner radius of the annulus is chosen by plotting the PSF extracted directly from the image and comparing this to the known XRT PSF which is described by a King function:

$$\mathsf{PSF}(r) = \left[1 + \left(\frac{r}{r_c}^2\right)\right]^{-\beta}, \tag{3.4.2}$$

where $r_c \simeq 5.8$ and $\beta \simeq 1.55$ (Moretti et al., 2005). The point at which the data and the model diverge is set as the inner radius of the annulus. In *photon counting mode*, a larger background region allows for a better estimate of the background, so a large circular region offset from the source is used.

Once the source and background selection regions are finalised, spectra and light curves can be extracted from them. Corresponding exposure maps and response files are generated. The source spectrum is then passed through a final level of processing in conjunction with the background spectrum and the response files to make it suitable for analysis with XSPEC. In this stage, the spectrum is grouped into 500 events per energy bin to ensure that χ^2 statistics are valid when performing the spectral fit in XSPEC, and the first 30 channels (0-29) are flagged as "bad".

3.5 Bayesian block algorithm for optimum binning of astrophysical time series

The Bayesian block binning algorithm is a nonparametric modelling technique that finds the optimal segmentation of data in an observation interval (Scargle et al., 2013). It addresses the general problem of detecting and characterising local variability in time series data, where "local" refers to features in a sub-range of the total interval. For signals that may be present all or most of the time, such as periodicity, Fourier or wavelet analyses would be more appropriate. The method can be used for essentially any data mode (i.e., time-tagged events, binned data or point measurements), and in this dissertation it is applied to point measurements, i.e., measurements of source flux with gaussian errors.

The optimal segmentation of the data is that which corresponds to the maximum of some quantitative expression, for example, the sum of a goodness-of-fit measure of a simple model of the data in each segment. For this work, the piecewise constant model is chosen to describe the data in each segment. Using this model, the time range of the observation interval is divided into segments, from here on called "blocks", where the signal is modelled as a constant. In this case, the segmentation analysis is known as "change-point detection", where the "change points" are the discrete times at which there is a significant change in the signal. This is the simplest model, and allows for an exact treatment of quantities such as the likelihood. More complex models can be used, but their improved flexibility is offset by the increased complexity of the model and its interpretation.

A key issue for this analysis is determining the number of blocks in the final representation. The number of blocks cannot be set explicitly, but it is influenced by defining a prior distribution for the number of blocks. A parameter that controls the steepness of the prior distribution is adjusted, establishing relative probabilities of smaller or larger number of blocks. A prior that assigns smaller probability to a large number of blocks is desired, and in this regard, the geometric prior (Coram, 2002) is used:

$$P(N_{\text{blocks}}) = p\gamma^{N_{\text{blocks}}} \tag{3.5.1}$$

In general, the value N_{blocks} is not known in advance. To circumvent this issue, the value $\text{ncp}_{\text{prior}}$ is introduced, which is the contribution of the prior to the fitness. Scargle et al. empirically relate $\text{ncp}_{\text{prior}}$ to the false-positive probability p_0 using simulations of a synthetic pure-noise time series. This relation is given by the expression

$$\text{ncp}_{\text{prior}} = 4 - \ln\left(73.53 p_0 N^{-0.478}\right) \tag{3.5.2}$$

where N is the total number of data points in the observation interval. Adjusting $\text{ncp}_{\text{prior}}$ through p_0 is equivalent to adjusting the prior distribution.

The algorithm starts at the beginning of the time series, and with each iteration, adds one more data point into the subset of data under consideration for partitioning. For each new data point added, all possible block representations of the current subset of data is tested. The partitioning that provides the maximum fitness is chosen, as it is most representative of the data. For point measurements, the fitness is given by

$$\ln\left(L_{\text{max}}^{(k)}\right) = \frac{b_k^2}{4a_k}, \quad a_k = \frac{1}{2}\sum_n^k \frac{1}{\sigma_n^2} \quad \text{and} \quad b_k = -\sum_n^k \frac{x_n}{\sigma_n^2}, \tag{3.5.3}$$

where x_n is the value of the point measure, and σ_n is the corresponding error. The value of $\text{ncp}_{\text{prior}}$ must also be subtracted from $\ln\left(L_{\text{max}}^{(k)}\right)$ to include the effect of the prior on the fitness. This process continues until all the data points have been included, thus finding the optimal block representation of the entire time series.

3.5.1 Determination of uncertainty

Analysis of uncertainty is an important component of any data analysis procedure. Two aspects of uncertainty are addressed in this work, the first concerning the significance of the change points found by the algorithm and the second concerning the locations of the change points.

To calculate the significance of a given change point, a likelihood ratio test is used. The fitness for the blocks directly on either side of the change point is compared to that of the single block that would exist if the change point were not there. This test is equivalent to the TS measure used in the *Fermi*-LAT analysis.

The location of a given change point can be easily tested in an approximate way that neglects inter-change-point dependencies. This is achieved by fixing all but the change point in question and then computing the fitness as a function of the location of that change point. The fitness distribution can then be converted into a normalised probability distribution which provides comprehensive information about the location of the change point.

3.6 Bibliography

Abdo, A. A., Ackermann, M., Ajello, M., et al., 2009; 'FERMI LARGE AREA TELESCOPE BRIGHT GAMMA-RAY SOURCE LIST'. *The Astrophysical Journal Supplement Series*, vol. 183(1):46

Aharonian, F., Hofmann, W., Konopelko, A., et al., 1997; 'The potential of ground based arrays of imaging atmospheric Cherenkov telescopes. I. Determination of shower parameters'. *Astroparticle Physics*, vol. 6(3-4):343

Aharonian, F. A., Akhperjanian, A., Barrio, J. A., et al., 2001; 'Evidence for TeV gamma ray emission from Cassiopeia A'. *Astronomy and Astrophysics*, vol. 370:112

Berge, D., Funk, S., Hinton, J., 2007; 'Background modelling in very-high-energy $\{\gamma\}$-ray astronomy'. *Astronomy and Astrophysics*, vol. 466:1219

Burrows, D. N., Hill, J. E., Nousek, J. A., et al., 2005; 'The Swift X-Ray Telescope'. *Space Science Review*, vol. 120:165

Capalbi, M., Perri, M., Saija, B., et al., 2005; 'The Swift XRT Data Reduction Guide'. http://www.swift.ac.uk/analysis/xrt/files/xrt_swguide_v1_2.pdf

Coram, M., 2002; *Nonparametric Bayesian Classification*. PhD Thesis, Stanford University

FSSC, 2013; 'Fermi Science Tools Cicerone - Likelihood'. http://fermi.gsfc.nasa.gov/ssc/data/analysis/documentation/Cicerone/Cicerone_Likelihood/

Hanna, D., McCann, A., McCutcheon, M., et al., 2010; 'An LED-based flasher system for VERITAS'. *Nuclear Instruments and Methods in Physics Research Section A*, vol. 612(2):278

Hillas, A. M., 1985; ‘Cerenkov light images of EAS produced by primary gamma’. In ‘Proceedings of the 19th International Cosmic Ray Conference’, , (eds. Jones, F. C., Adams, J., Mason, M.), vol. 3 of *International Cosmic Ray Conference*, 445–448. NASA Conf. Publ., La Jolla, USA

Hofmann, W., Jung, I., Konopelko, A., et al., 1999; ‘Comparison of techniques to reconstruct VHE gamma-ray showers from multiple stereoscopic Cherenkov images’. *Astroparticle Physics*, vol. 12(3):135

Kildea, J., Atkins, R. W., Badran, H. M., et al., 2007; ‘The Whipple Observatory 10 m gamma-ray telescope, 1997 - 2006’. *Astroparticle Physics*, vol. 28(2):182

Konopelko, A., Hemberger, M., Aharonian, F. A., et al., 1999; ‘Performance of the stereoscopic system of the HEGRA imaging air Čerenkov telescopes: Monte Carlo simulations and observations’. *Astroparticle Physics*, vol. 10:275

Li, T.-P., Ma, Y.-Q., 1983; ‘Analysis methods for results in gamma-ray astronomy’. *The Astrophysical Journal*, vol. 272:317

Moretti, A., Campana, S., Mineo, T., et al., 2005; ‘Inflight calibration of the Swift XRT Point Spread Function’. In ‘Society of Photo-Optical Instrumentation Engineers (SPIE) Conference Series’, , (ed. Siegmund, O. H. W.), vol. 5898, 360

Nolan, P. L., Abdo, A. A., Ackermann, M., et al., 2012; ‘Fermi Large Area Telescope Second Source Catalog’. *The Astrophysical Journal Supplement Series*, vol. 199(2):31

Page, K., UK Swift Science Data Centre, 2011; ‘XRT Data Analysis Guide’. http://www.swift.ac.uk/analysis/xrt/

Petry, D., 2001; ‘Large zenith angle observations with the high-resolution Granite III camera’. In ‘Proceedings of the 27th International Cosmic Ray Conference.’,

Punch, M., Akerlof, C. W., Cawley, M. F., et al., 1991; ‘Supercuts: An Improved Method of Selecting Gamma-rays’. In ‘Proceedings of the 22nd International Cosmic Ray Conference. 11-23 August’, vol. 1

Reynolds, P. T., Akerlof, C. W., Cawley, M. F., et al., 1993; ‘Survey of candidate gamma-ray sources at TeV energies using a high-resolution Cerenkov imaging system - 1988-1991’. *The Astrophysical Journal*, vol. 404:206

RXTE Guest Observer Facility, 2006; ‘Reduction and Analysis of PCA Binned-Mode Data’. http://heasarc.nasa.gov/docs/xte/recipes/pca_spectra.html

Scargle, J. D., Norris, J. P., Jackson, B., et al., 2013; ‘STUDIES IN ASTRONOMICAL TIME SERIES ANALYSIS. VI. BAYESIAN BLOCK REPRESENTATIONS’. *The Astrophysical Journal*, vol. 764(2):167

Chapter 4

Non-thermal emission of astrophysical objects

Many classes of astrophysical objects have now been detected at VHE energies. AGN constitute the most numerous source class, but starburst galaxies, pulsar wind nebulae (PWNe), supernova remnants (SNRs), binaries and pulsars have also been observed. Although this list covers a wide variety of source types, they all share a common property that makes them visible at VHE energies: each one is a site of non-thermal emission.

4.1 Non-thermal emission mechanisms

Non-thermal processes are the primary mechanisms for producing the broadband radiation observed from astrophysical sources. Synchrotron radiation is generated by charged particles moving relativistically in a electromagnetic fields. Inverse-Compton scattering can then promote these photons into the VHE regime. This is believed to be the primary production mechanism for astrophysical VHE radiation, and requires the presence of both a low-energy photon field and an ultra-relativistic electron population.

Synchrotron radiation up to X-ray energies is commonly observed in astrophysical sources. In order to produce such energetic photons, the accelerated electrons must have Lorentz factors of order $\gamma \simeq 10^6$, equivalent to energies of about a few TeV. From this, it is clear that understanding the acceleration of charged particles is necessary to explain the observed non-thermal emission.

4.1.1 Acceleration of charged particles

Any process that accelerates high-energy particles should naturally explain the characteristic power-law energy spectrum that is observed (e.g., Kirk & Duffy, 1999; Longair, 2011, Ch. 17). The Fermi acceleration processes (Fermi, 1949) remain among the most efficient and feasible mechanisms. These processes and the magnetic reconnection mechanism are relevant to the AGN and PWN studied in this thesis, and are outlined below.

First-order Fermi acceleration This acceleration mechanism, also referred to as diffusive shock acceleration, is a process that is capable of providing large boosts to a particle's energy as it repeatedly crosses a shock front. A shock typically has magnetic inhomogeneities close by in both the downstream and upstream regions, which can reflect a particle back and forth across a shock front. The particle gains an average energy of

$$\left\langle \frac{\Delta E}{E} \right\rangle = \frac{2\beta}{3} \tag{4.1.1}$$

with each crossing, where $\beta = v/c$ is the velocity of the shock.

This process results in a power-law energy spectrum of particles

$$n(\gamma) \propto \gamma^{-q}, \tag{4.1.2}$$

as the probability of a particle remaining in the acceleration region decreases with an increasing number of crossings. Thus, fewer particles are accelerated to higher energies. At parallel shocks (the upstream and downstream flows are both parallel to the magnetic field and perpendicular to the shock), the spectral index q is generally in the range $2.2 \leq q \leq 2.3$ for isotropic scattering in the upstream and downstream (Achterberg et al., 2001). Summerlin & Baring (2012) showed that acceleration at oblique (the flows are neither parallel nor perpendicular to the magnetic field or the shock) subluminal shocks is capable of producing hard ($q < 2$) particle spectral indices in the presence of large-angle scattering.

It is worth noting that first-order Fermi acceleration proceeds quite differently in the ultrarelativistic limit. Achterberg et al. (2001) show that the process is subject to the effects of relativistic beaming, and upstream particles are confined to a small angle with respect to the shock normal. The energy change per shock crossing cycle becomes limited to $\Delta E \simeq E$, except for the first crossing in which the particles originate upstream. In that case, the energy is boosted by a factor of $\sim \Gamma_s^2$, where Γ_s is the Lorentz factor of the shock, for those particles that are scattered back across the shock into the upstream region.

Second-order Fermi acceleration In this scenario, turbulence in the magnetic field causes the presence of randomly moving "magnetic mirrors". A particle is reflected from the magnetic mirror, gaining energy if the mirror is moving towards the particle and losing energy if it is receding. As the probability of a head-on collision with the mirror is greater than a rear-on collision, the energy of the particle increases with time. Averaged over the all collision angles, the particle receives an average gain in energy per collision of

$$\left\langle \frac{\Delta E}{E} \right\rangle = \frac{8\beta^2}{3}, \tag{4.1.3}$$

where $\beta = v/c$ is the velocity of the mirror. This gives an exponential increase in the energy of the particle as the same fractional increase occurs on each collision.

A feature of this acceleration process is that it also naturally produces a power-law particle distribution (see Equation 4.1.2) where the index $q = 1 + (\alpha\tau_{\mathsf{esc}})^{-1}$. Here, τ_{esc} is the time that a particle remains within the accelerating region and $\alpha = (4/3)(v^2/cL)$, where L is the mean free path between mirrors along a field line.

Shear acceleration Rieger & Duffy (2004) consider a number of scenarios for particle acceleration by a velocity shear in astrophysical jets. This type of acceleration may be important for blazars that exhibit very hard electron injection spectral indices, such a 1ES 1959+650 (see Chapter 5). However, shear acceleration is much more favourable for protons rather than electrons, given that the mean free path for protons is much greater than the mean free path for electrons emitting at the same frequency.

Although second-order Fermi effects are not directly taken into account, it is likely that lower-energy emission resulting from second-order Fermi processes can provide the seed particles for efficient gradual shear acceleration within the jet.

Magnetic reconnection This is a process through which magnetic energy can be converted into kinetic energy and particle acceleration through the topological rearrangement of magnetic field lines. Oppositely directed magnetic field lines in a plasma can break and reconnect, altering the connectivity pattern in doing so (Parker, 1957; Sweet, 1958; Petschek, 1964). This is schematically illustrated in Figure 4.1.

Magnetic reconnection has been invoked as a mechanism capable of producing the minute-scale VHE variability that has been observed in blazars such as PKS 2155-304 (Aharonian et al., 2007) and Mrk 501 (Albert et al., 2007). For such rapid variability, causality arguments that relate the minimum variability timescale to the light crossing time of the emitting region constrain

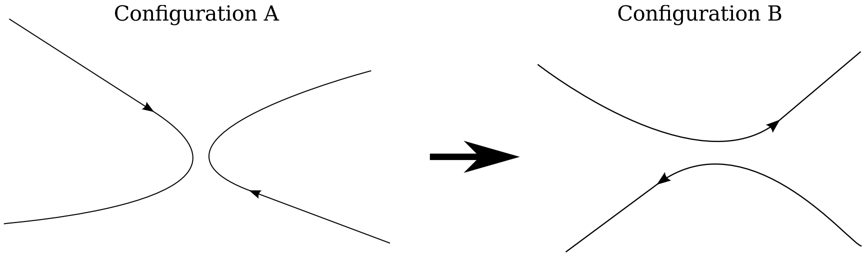

Figure 4.1: Schematic depiction of magnetic reconnection. In the left, two oppositely directed magnetic field lines are present in a given configuration. They break, and reconnect in a different configuration, shown on the right, thus rearranging the magnetic topology.

the emitting region to be much smaller than the size of even a small black hole. Giannios et al. (2009) propose a model in which compact emitting regions move relativistically within a Poynting flux-dominated jet. A fraction of the magnetic energy of the jet is assumed to dissipate through reconnection events, following the process presented in Lyubarsky (2005), which gives a relativistic generalisation of classical (the Sweet-Parker and Petschek) reconnection models. The material outflowing relativistically (in the frame of the jet) from these reconnection regions can efficiently power rapid flares from X-rays through to VHE γ-rays, and is capable of producing observable VHE flares even for a jet of moderate bulk Lorentz factor ($\Gamma \simeq 10$). However, Narayan & Piran (2012) conclude that this type of model can only produce the variability observed in PKS 2155-304 if magnetic reconnection in relativistic plasmas proceeds at the speed of light, which is faster than is currently expected.

Some emerging models of the Crab Nebula also use magnetic reconnection as a mechanism to explain the observed flares from the nebula. One such model that is of particular interest to this thesis (Chapter 6) is that of Bednarek & Idec (2011). The authors suggest that efficient reconnection can occur in the region where the pulsar wind is compressed by the deceleration at the pulsar wind shock region. This allows for particle acceleration that is not limited by synchrotron energy losses in the reconnection regions. This model is discussed in more detail in Section 4.3.1.

4.1.2 Doppler beaming

In classical mechanics, the Doppler shift is given by

$$\nu = \frac{\nu_{\text{em}}}{1 - \beta \cos\theta} \tag{4.1.4}$$

(e.g., Longair, 2011; Böttcher et al., 2012; Rybicki & Lightman, 1979)[1]. When relativistic motion is introduced, the expression is similar but the effects of time dilation become important. For

---

[1] In this section, the subscript "em" refers to values in the frame of the emitting source, and the subscript "obs" refers to values in the frame of the observer.

example, consider a source emitting radiation of a given frequency ν_{em}. In this case, the spatial separation of corresponding points on the waveform (i.e., peak, or trough) is given by $c\Delta t_{\text{em}}$. In the rest frame of an observer, this separation is reduced by the component of the source's displacement along the line of sight in that time, $(v\cos\theta)\Delta t$. The separation in the observer's frame is then given by

$$\Delta t_{\text{obs}} = (c - v\cos\theta)\Delta t = (1-\beta\cos\theta)\gamma\Delta t_{\text{em}}. \tag{4.1.5}$$

Thus, the frequency of the radiation in the observer's frame is

$$\nu_{\text{obs}} = \frac{\nu_{\text{em}}}{\gamma(1-\beta\cos\theta)} = D\nu_{\text{em}}, \tag{4.1.6}$$

where $D = 1/\gamma(1-\beta\cos\theta)$ is the relativistic Doppler factor.

The apparent direction of electromagnetic radiation also differs between inertial frames. This relativistic aberration is the cause of beaming in astrophysical jets. The propagation directions θ_{obs} and θ_{em} of the radiation can be compared using

$$\cos\theta_{\text{obs,em}} = \frac{k_{x\ \text{obs,em}}}{k_{\text{obs,em}}}, \tag{4.1.7}$$

where k is the wave vector, and k_x is the component of it along the line of sight. Using the relativistic Doppler formula, Equation 4.1.6, and the appropriate Lorentz transformations for the wave vector, this gives the relation

$$\cos\theta_{\text{obs}} = \frac{\cos\theta_{\text{em}} + \beta}{1+\beta\cos\theta_{\text{em}}}. \tag{4.1.8}$$

A limiting case of this formula is $\beta \to 1$, in which case, $\cos\theta_{\text{obs}} \to 1$. This is the condition for relativistic beaming.

The beam angle θ_b is defined to be the half-angle of the cone that encompasses half of the emitted radiation of a source. For a source that emits isotropically, $\theta_{b\ \text{em}} = \pi/2$ and $\cos\theta_{b\ \text{obs}} = \beta = \left(1 - 1/\gamma^2\right)^{1/2}$. When $\gamma \gg 1$, $\theta_{b\ \text{obs}} \simeq 0$. This allows a series expansion of $\theta_{b\ \text{obs}}$ for small angles, and the square root for large γ, resulting in the approximate relation

$$\theta_{b\ \text{obs}} \simeq \frac{1}{\gamma}. \tag{4.1.9}$$

Figure 4.2 illustrates the effects of Doppler beaming of an isotropic emitter.

The observed fluxes from astrophysical sources are also affected by the relativistic Doppler factor. The energy flux in electromagnetic radiation is given by

$$F(\nu) = h\nu \frac{d^3N_{ph}}{dt\,dA\,d\nu} \tag{4.1.10}$$

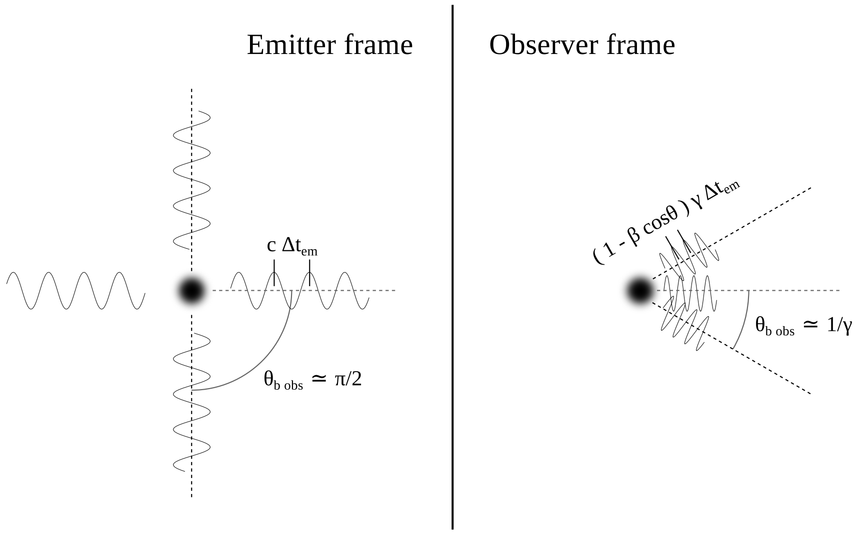

Figure 4.2: The effects of Doppler beaming of an isotropic emitter in the observer frame. The left hand side shows the emitter in its rest frame. In this case, half the emitted radiation is contained within a half-angle of $\pi/2$, and the spatial separation of corresponding points on the waveform is given by $c\Delta t_{\mathrm{em}}$. The right hand side shows the emitter as it appears in the observer frame, in which it is moving relativistically. Relativistic aberration in this frame causes half the emitted radiation to appear within a half-angle of $\sim 1/\gamma$, and the separation of corresponding points on the waveform is given by $(1-\beta\cos\theta)\gamma\Delta t_{\mathrm{em}}$.

where d^3N_{ph} is the number of photons in a frequency interval $[\nu, \nu+d\nu]$. Introducing the distance d between the emitter and the observer, the area can be rewritten as $dA = d^2 d\Omega$, where $d\Omega = d\theta\, d\phi$ is a solid angle element. The transformation between the observed flux and emitted flux is

$$F_{\mathrm{obs}}(\nu_{\mathrm{obs}}) = F_{\mathrm{em}}(\nu_{\mathrm{em}}) \frac{\nu_{\mathrm{obs}}}{\nu_{\mathrm{em}}} \frac{d\nu_{\mathrm{em}}\, d\Omega_{\mathrm{em}}\, dt_{\mathrm{em}}}{d\nu_{\mathrm{obs}}\, d\Omega_{\mathrm{obs}}\, dt_{\mathrm{obs}}} \tag{4.1.11}$$

The frequency transformations cancel out, and it can be seen from Equation 4.1.5 that $dt_{\mathrm{em}}/dt_{\mathrm{obs}} = D$. Also, $\phi_{\mathrm{em}} = \phi_{\mathrm{obs}}$, so $d\Omega_{\mathrm{em}}/d\Omega_{\mathrm{obs}}$ reduces to the derivative of Equation 4.1.8 for transforming θ_{em} to θ_{obs}, which works out to be D^2. Therefore

$$F_{\mathrm{obs}}(\nu_{\mathrm{obs}}) = D^3 F_{\mathrm{em}}(\nu_{\mathrm{em}}) \tag{4.1.12}$$

For a power law, $F(\nu) \propto \nu^{-p}$, and the flux transformation can be further simplified by expressing F_{em} evaluated at the observed frequency using

$$F_{\mathrm{em}}(\nu_{\mathrm{em}}) = F_{\mathrm{em}}(\nu_{\mathrm{obs}}) \left(\frac{\nu_{\mathrm{obs}}}{\nu_{\mathrm{em}}}\right)^p = D^p F_{\mathrm{em}}(\nu_{\mathrm{obs}}), \tag{4.1.13}$$

and so

$$F_{\mathrm{obs}}(\nu_{\mathrm{obs}}) = D^{3+p} F_{\mathrm{em}}(\nu_{\mathrm{obs}}) \tag{4.1.14}$$

4.1.3 Synchrotron radiation

A charged particle will follow a helical trajectory around field lines when travelling through a magnetic field B (e.g., Rybicki & Lightman, 1979; Longair, 2011). As a consequence of this motion, the particle emits cyclotron radiation primarily at the gyrofrequency

$$\omega_g = \frac{eB}{m}, \tag{4.1.15}$$

where e is the charge of the particle, B is the magnetic field, and m is the mass of the particle. Radiation is also emitted at harmonics of the gyrofrequency, but the energy in higher harmonics is small when the particle is non-relativistic. If the particle is moving relativistically however, the higher harmonics become important. Doppler beaming and aberration effects result in a spread of the emitted frequencies, and the high harmonics can become so broadened that the emission spectrum becomes continuous. In the relativistic case, the radiation is known as synchrotron radiation. This process is most efficient for light particles such as electrons.

The average energy loss rate of an electron in a magnetic field is given by

$$-\left(\frac{dE}{dt}\right)_s = \frac{4}{3}\sigma_T c \beta^2 U_B \gamma^2, \tag{4.1.16}$$

where σ_T is the Thompson cross section, $\beta = v/c$ is the particle velocity, U_B is the energy density of the magnetic field, and γ is the Lorentz factor of electron which is related to its energy via $E = \gamma m_e c^2$.

The synchrotron lifetime of a particle is defined as the ratio of the electron energy to the energy-loss rate from synchrotron radiation,

$$\tau_s = \frac{E}{(dE/dt)} \propto \frac{1}{B^2 E}. \tag{4.1.17}$$

This describes the typical timescale in which an electron loses its energy, or "cools".

As the electron is travelling relativistically, the resulting radiation is beamed in the direction of motion by a factor of γ^2 due to relativistic aberration between the rest frame of the electron and the rest frame of the observer. The beamed synchrotron radiation sweeps around as the electron moves on its helical path. A pulse of radiation is seen by the observer every time the electron's velocity vector lies within an angle of $\sim 1/\gamma$ to the observer's line of sight (see Equation 4.1.9). The spectrum of radiation the observer receives is the Fourier transform of this pulse, once the effects on the duration of the pulse in the observer frame have been taken into account. In the observer frame, the pulse duration is given by

$$\Delta t \simeq \frac{1}{2\gamma^2 \omega_g}, \tag{4.1.18}$$

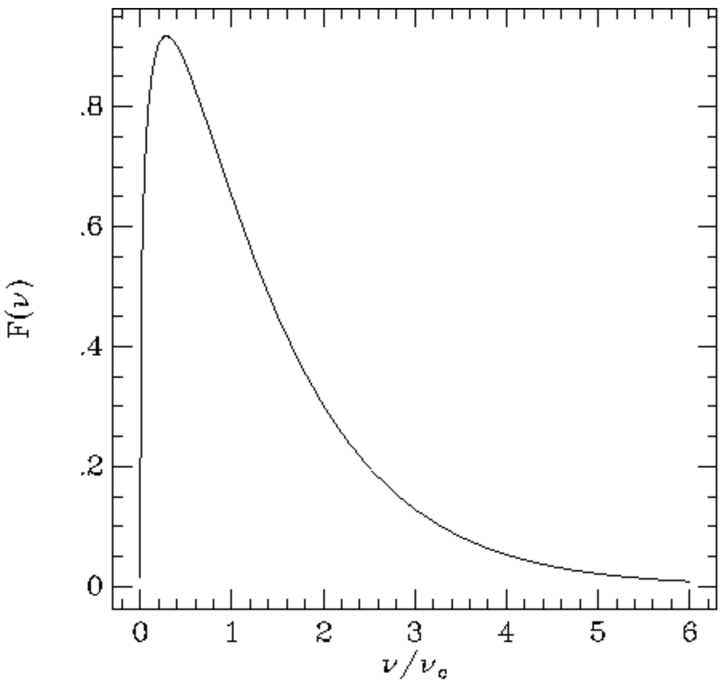

Figure 4.3: Synchrotron spectrum of a single electron showing the characteristic power-law index $\sim 1/3$ at lower energies and exponential decrease at higher energies.

Therefore, the observed pulse duration is $\sim 1/\gamma^2$ times shorter than the non-relativistic gyroperiod $T_g = 2\pi/\omega_g$. Thus, the maximum Fourier component occurs at the frequency

$$\omega = 1/\Delta t \simeq \gamma^2 \omega_g. \tag{4.1.19}$$

A complete derivation of the synchrotron spectrum can be found in text books (e.g., Longair, 2011), but the main result is presented here. The *critical angular frequency* is defined as

$$\omega_c = \left(\frac{3}{2}\right)\left(\frac{c}{v}\right)\gamma^2 \omega_g \sin\alpha, \tag{4.1.20}$$

where α is the pitch angle of the electron. This critical frequency comes from a more rigorous analysis of the radiation, but has a very similar form to Equation 4.1.19. The synchrotron emission is relatively peaked, with maximum emission occurring at $0.29\,\omega_c$. The intensity I of the emission on either side of the maximum behaves according to

$$I(\omega) \propto \begin{cases} \left(\frac{\omega}{\omega_c}\right)^{\frac{1}{3}}, & \omega \ll \omega_c \\ \left(\frac{\omega}{\omega_c}\right)^{\frac{1}{2}} \exp\left(-\frac{\omega}{\omega_c}\right), & \omega \gg \omega_c \end{cases}. \tag{4.1.21}$$

Figure 4.3 shows the synchrotron spectrum of a single electron, which is essentially the sum of a large number of harmonics of the basic gyrofrequency.

If the underlying electron distribution has a power-law spectrum of index $-p$, then the resulting synchrotron radiation also has a power-law spectrum. The simplifying approximation that each electron radiates all of its power the single frequency $\omega = \gamma^2\omega_g$ is used. The index of the resulting photon spectrum is is related to p through

$$F(\nu) \propto B^{\frac{p+1}{2}} \nu^{\frac{-(p-1)}{2}}. \tag{4.1.22}$$

Polarisation The *velocity cone* of an electron is described by the velocity $\mathbf{v}$ of the electron as it spirals about the magnetic field. The magnetic field direction is the axis of the cone, and $\mathbf{v}$ precesses about this axis.

The synchrotron radiation from a single electron is elliptically polarised, as the component parallel to the magnetic field has a different time dependence within each pulse of radiation compared to that of the perpendicular component. In the general case of many electrons with a distribution of pitch angles, all the electrons with velocity cones within the angle $1/\gamma$ of the line of sight contribute to the intensity of radiation the observer sees. These contributions are elliptically polarised in opposite directions on either side of the velocity cone. The overall polarisation is found by integrating over all contributing electrons, and because the angle $1/\gamma$ is very small when the electron is ultrarelativistic, the components of elliptical polarisation parallel to the magnetic field cancel out, and the resultant polarisation is linear.

If the electrons have a power-law energy spectrum of index $-p$, then the fractional polarisation is given by

$$\Pi = \frac{p+1}{p+\frac{7}{3}} \tag{4.1.23}$$

For a typical value of the index, for example $p = 2.5$, the fractional polarisation of synchrotron radiation is expected to be $\sim 72\%$. Thus, in general, the synchrotron radiation of ultrarelativistic electrons in a uniform magnetic field is expected to be highly polarised.

Self-absorption If synchrotron radiation were a thermal process, the particles would have a Maxwellian energy distribution with characteristic temperature $T \sim E/3k$, and the source could not have a brightness temperature[2] greater than T. In fact, absorption occurs regardless of the underlying particle energy distribution, and in this case it is known as synchrotron self-absorption.

Following Longair (2011), if the synchrotron source has the same physical size at all frequencies, the brightness temperature is given by

$$T_b = \left(\frac{\lambda^2}{2k}\right)\left(\frac{F(\nu)}{\Omega}\right), \tag{4.1.24}$$

---

[2] The brightness temperature of an object is the temperature a black body would need to be in order to produce the same intensity at a given frequency ν.

where Ω is the solid angle the source subtends at the observer. T_b is defined using the intensity I_ν of black-body radiation

$$I_\nu = \frac{F(\nu)}{\Omega} = \frac{2h\nu^3}{c^2 e^{(h\nu/kT_b)} - 1} \simeq \frac{2kT_b}{\lambda^2} \tag{4.1.25}$$

in the Rayleigh-Jeans limit. Here, T_b is a lower limit to the temperature of the region as it cannot emit incoherent radiation with an intensity greater than that of a black-body at its thermodynamic temperature. Typically, the spectra of radio sources have an index $\frac{-(p-1)}{2} \simeq 1$, so at sufficiently low frequencies, the brightness temperature of the source will approach the effective electron temperature at that frequency, and self-absorption effects become important.

While a power-law electron distribution is not a thermal equilibrium spectrum, the concept of temperature can still be used. The spectrum of radiation emitted by electrons of energy E is peaked about the critical frequency $\nu = \nu_c$, so emission and absorption processes at the frequency ν are associated with electrons of approximately the same energy. Also, the characteristic timescale for a relativistic gas to relax to an equilibrium spectrum is very long under typical cosmic conditions. Therefore, a temperature T_e can be associated with electron of a given energy through

$$\gamma m_e c^2 = 3kT_e. \tag{4.1.26}$$

Thus, the effective temperature of electrons is a function of their energy.

Given that $\gamma \simeq \left(\frac{\nu}{\nu_g}\right)^{1/2}$, T_e can be written as

$$T_e \simeq \left(\frac{m_e c^2}{3k}\right)\left(\frac{\nu}{\nu_g}\right)^{1/2}. \tag{4.1.27}$$

For a self-absorbed source, the brightness temperature of the radiation must be equal to the effect kinetic temperature of the emitting electrons (i.e., $T_b = T_e$), and so in the Rayleigh-Jeans limit

$$F(\nu) = \frac{2kT_e}{\lambda^2}\Omega = \frac{2m_e}{3\nu_g^{1/2}}\Omega\nu^{5/2} \qquad \text{i.e.,} \qquad F(\nu) \propto B^{-1/2}\nu^{5/2}. \tag{4.1.28}$$

Thus, in the self-absorbed region, the synchrotron spectrum depends only on the magnetic field.

4.1.4 Inverse-Compton radiation

The inverse-Compton (IC) scattering of photons is one of the primary VHE γ-ray production mechanisms. It requires the presence of both a low-energy photon field and an ultra-relativistic electron population. In this situation, the ultra-relativistic electrons scatter the low-energy photons up to high energies, the electrons losing kinetic energy in the process.

In the case where the energy of the photon is much less than the rest mass of the electron $E_p \ll m_e c^2$, the average energy-loss rate of an electron in a single IC scattering event is given by

$$-\left(\frac{dE}{dt}\right)_{IC} = \frac{4}{3}\sigma_T c \beta^2 U_p \gamma^2, \qquad (4.1.29)$$

where U_P is the energy density of the photon field, and the other terms are defined as in Equation 4.1.16. This describes the Thomson regime (elastic scattering), in which the cross section for scattering is constant and given by σ_T. Photons can be accelerated up to a maximum energy of

$$E_{\mathsf{max}} \simeq 4\gamma^2 E_p \qquad (4.1.30)$$

where E_P is the initial energy of the photons in the photon field (the unscattered photons are assumed to be monoenergetic). The average energy of the upscattered photons is given by

$$\langle E \rangle = \frac{4}{3}\gamma^2 E_p. \qquad (4.1.31)$$

At high energies, quantum effects become important and the Klein-Nishina cross section must be used in place of the Thomson cross section. In this regime, where $E_p \gtrsim m_e c^2$, the cross section begins to drop off significantly, decreasing roughly proportional to $(m_e c^2)/E_p$ at the highest energies. Thus, IC scattering is not an efficient mechanism for upscattering high-energy photons.

If the electron population has a power-law distribution of index $-p$, the resulting IC spectrum is also described a power law. In the Thomson regime, the photon spectrum index is related to that of the electrons by

$$F(\nu) \propto \nu^{\frac{-(p-1)}{2}}, \qquad (4.1.32)$$

just as in the case of synchrotron radiation. In the Klein-Nishina regime, the resulting photon spectrum is steeper, given by the relation

$$F(\nu) \propto \nu^{-p}. \qquad (4.1.33)$$

4.2 IC emission models for blazars

Blazars are active galactic nuclei that appear bright from radio to γ-ray frequencies due to the close alignment of their relativistic jets along the line of sight of the observer. The blazar spectral energy distribution (SED) is characterised by a non-thermal double-peaked structure. This emission is assumed to be produced in the jets, and the low-energy peak (radio to UV or X-ray) is attributed to synchrotron emission from relativistic electrons. Different models exist to describe the origin of the high-energy peak, and depend on whether the emission is dominated by leptonic or hadronic components.

4.2.1 Leptonic models

Leptonic models constitute the most popular models used to describe blazar observations. In this type of model, the high-energy peak (extending to TeV energies) is attributed either to the IC up-scattering of the synchrotron photons by relativistic electrons (synchrotron self-Compton models; SSC) (e.g., Maraschi et al., 1992; Böttcher & Chiang, 2002; Sokolov et al., 2004), or the up-scattering of photons external to the jet (external Compton models; EC) (e.g., Sikora et al., 1994; Dermer et al., 1992). These scenarios are not exclusive, and models can include a combination of both.

In an SSC model, a population of relativistic electrons moves along the blazar jet, which carries some magnetic field, and the electrons generate synchrotron radiation. These photons are then up-scattered by the same population of electrons that produced them. This type of model is widespread, but can struggle to reproduce cases where the multiwavelength SED is dominated by the γ-ray component. A photon field external to the jet can be introduced into the scenario to add an EC component to the model to address this problem. Multi-component SSC models also exist and allow for the presence of multiple electron populations.

4.2.2 Hadronic models

In a situation where the hadronic component dominates, the high-energy peak originates from the γ-ray emission of VHE protons. In order to accelerate protons to the ultra-relativistic energies required for this process, very large magnetic fields are required (a few tens of G). These protons can produce secondary γ rays by interacting with matter inside the jet (Pohl & Schlickeiser, 2000), or by interacting with synchrotron photons (Mücke & Protheroe, 2000; Böttcher, 2005). A feature of this emission scenario is that it necessarily creates neutrinos. Therefore, the reliable detection of neutrinos from a blazar would clearly favour a hadronic model for the source.

Böttcher (2005) developed a hadronic model to describe the orphan VHE flare of 1ES 1959+650. Single-zone leptonic models struggle to reproduce such orphan flaring behaviour, as an inevitable feature of an SSC model is that any VHE flaring activity should be accompanied by a (quasi-)simultaneous flare in the synchrotron component. In contrast, relativistic protons may interact with an external photon field supplied by the electron synchrotron radiation to produce VHE emission independent of the synchrotron component.

Böttcher (2010) presents a more general lepto-hadronic model for blazar spectra, using analytic fit functions to Monte-Carlo generated results of hadronic interactions, along with some prior assumptions about the target photon field (in this case, the electron-synchrotron photon field) as well as the proton spectrum. This simplified lepto-hadronic model provides reasonable representations of the spectral energy distributions of the four sub-classes of blazars, modelling even strongly peaked spectral shapes.

4.2.3 SSC models

In this dissertation, a SSC model with an additional EC component is used to describe the multiwavelength SED of the blazar 1ES 1959+650 (Chapter 5). Two versions of this type of model are applied to the observations. The first model (model 1) is essentially the model described in Acciari et al. (2009) (which is a quasi-equilibrium version of the model of Böttcher & Chiang (2002)) with the addition of an EC component. The parameters for this model were provided by Dr. Markus Böttcher. This is in accordance with the VERITAS publication policy, which requires that published model parameters be provided by an experienced theorist. The second model (model 2) is from the blazar SED tool[3] (Tramacere et al., 2011, 2009; Massaro et al., 2006) which provides a web interface to a numerical code that reproduces radiative and accelerative processes in blazar jets.

Model 1

This model assumes that a population of ultrarelativistic leptons is injected into a spherical emitting volume (the "blob") of radius R_B in the comoving frame which moves at a relativistic speed $\beta_\Gamma c$ which corresponds to the bulk Lorentz factor Γ. The size of the blob is constrained by the shortest observed variability timescale $\delta t_{\mathsf{var,min}}$ through the relation

$$R_B \leq \frac{c\delta t_{\mathsf{var,min}} D}{(1+z)}. \tag{4.2.1}$$

The injected population is described by an injection power L_e, where

$$L_e = \pi R_B^2 \Gamma^2 \beta_\Gamma c m_e c^2 \int_1^\infty \gamma n(\gamma) d\gamma, \tag{4.2.2}$$

and a single power law spectral shape of index q with low- and high-energy cutoffs, γ_{min} and γ_{max} respectively.

An equilibrium between the particle injection, radiative cooling, and the escape of particles from the emitting region gives rise to a temporary quasi-equilibrium state described by a broken power

---

[3] `http://isdc-web00.isdc.unige.ch/sedtool/SED_Web_tool/html_js/SED_Web_tool/SED_start_test.html`

law. Particle escape is specified through an escape time parameter η_{esc} where $t_{\text{esc}} = \eta_{\text{esc}}(R/c)$. The break in the electron spectrum occurs at γ_b, where $t_{\text{esc}} = t_{\text{cool}}(\gamma)$. Depending on whether γ_b is less than or greater than γ_{min}, the system is in the fast or slow cooling regime.

The relation $\gamma_b < \gamma_{\text{min}}$ puts the system in the fast cooling regime. In this case, the equilibrium distribution is described by

$$n(\gamma) \propto \begin{cases} \gamma^{-2}, & \gamma_b < \gamma < \gamma_{\text{min}} \\ \gamma^{-(q+1)}, & \gamma_{\text{min}} < \gamma < \gamma_{\text{max}} \end{cases} . \tag{4.2.3}$$

In the slow cooling regime, $\gamma_b > \gamma_{\text{min}}$, and the equilibrium distribution is given by

$$n(\gamma) \propto \begin{cases} \gamma^{-q}, & \gamma_{\text{min}} < \gamma < \gamma_b \\ \gamma^{-(q+1)}, & \gamma_b < \gamma < \gamma_{\text{max}} \end{cases} . \tag{4.2.4}$$

The external radiation field is characterised by blackbody emission from dust at a temperature T_{BB} and with energy density u_{ext} around the central AGN engine. Due to the low energy of these external seed photons, Klein-Nishina effects are expected to be negligible.

The observing angle between the jet and the line-of-sight, θ_{obs}, can be set to be the superluminal angle in the face of a lack of constraints. The superluminal angle is the angle for which Γ is equal to the Doppler factor D (see Equation 4.1.6). The magnetic field B in the emitting region is a free parameter. The Poynting flux along the jet is denoted by L_B,

$$L_B = \pi R_B^2 \Gamma^2 \beta_\Gamma c m_e c^2 U_B, \tag{4.2.5}$$

where $U_B = B^2/(8\pi)$ is the magnetic energy density. The equipartition parameter is given by L_B/L_e.

A standard flat ΛCDM cosmology is assumed, with $\Omega_m = 0.3$ and $\Omega_\Lambda = 0.7$. The effect of EBL absorption is accounted for using the model of Finke et al. (2010).

The free parameters of this model are given in Table 4.1.

Model 2

The SSC component of this model is almost identical to model 1. The radiation is produced in a relativistic jet with bulk Lorentz factor Γ that is observed at the superluminal angle. It is a purely leptonic SSC model with a single-zone homogeneous spherical emitting region of radius R_B, and an entangled magnetic field. Electrons are accelerated to relativistic energies

Parameter	Description
$\gamma_{\text{Bot, min}}$	Low-energy cutoff of the injected electron spectral distribution
$\gamma_{\text{Bot, max}}$	High-energy cutoff of the injected electron spectral distribution
q_{Bot}	Power law index of the injected electron spectral distribution
η_{esc}	Particle escape time parameter
B at z_0 (G)	Magnetic field strength
Γ	Bulk Lorentz factor
θ_{obs} ($^\circ$)	Observing angle between the AGN jet and the line-of-sight
T_{BB} (K)	Temperature of the external radiation field
u_{ext} (erg cm^{-3})	Energy density of the external radiation field
$\delta t_{\text{var,min}}$ (s)	Minimum variability timescale of the AGN (constrained by observations). This value implies the size of the emitting region (R_B).

Table 4.1: Free parameters of Model 1. Parameters relating to the injected electron spectral distribution (first three listed parameters) are given the subscript "Bot" to distinguish them from the otherwise similarly named parameters for Model 2.

through first order or stochastic second order shock acceleration, and their energy distribution is described by an analytic model. These electrons interact with the magnetic field, emitting synchrotron radiation.

For the EC scenario, the seed photons for the IC process are typically UV photons generated by the accretion disk of the black hole, reflected toward the jet by the broad line region within a typical distance from the accretion disk of order 1 pc. If the emission occurs at larger distances, the external radiation is likely to be provided by a dusty torus, and in this case, the photon field is typically peaked at IR frequencies.

The free parameters of model 2 are listed in Table 4.2.

When adjusted to represent the data presented in Chapter 5, γ_{min} is required to be different for model 1 and model 2. For model 1 the photon spectrum is given by $n(\gamma) \propto \gamma^{-(q+1)}$, and for model 2 $n(\gamma) \propto \gamma^{-q}$. This means care must be taken when directly comparing the parameters of the models, as the electron indices will appear to be in disagreement.

4.3 Emission models for pulsar wind nebulae

Pulsar Wind Nebulae (PWNe) are bubbles of shocked relativistic particles that are produced when the relativistic wind from a pulsar interacts with its environment (Gaensler & Slane,

Parameter	Description
N (cm^{-3})	The number of electrons per unit volume
$\gamma_{\text{T, min}}$	Low-energy cutoff of the injected electron spectral distribution
$\gamma_{\text{T, max}}$	High-energy cutoff of the injected electron spectral distribution
q_{T}	Power law index of the injected electron spectral distribution
B at z_0 (G)	Magnetic field strength
Γ	Bulk Lorentz factor
θ_{obs} ($^\circ$)	Observing angle between the AGN jet and the line-of-sight
T_{BB} (K)	Peak temperature of the disk
L_{disk}	Luminosity of the disk
R_{torus}	Radius of the torus
τDT	Fraction of the disk luminosity re-emitted by the torus in IR
$\delta t_{\text{var,min}}$ (s)	Minimum variability timescale of the AGN (constrained by observations). This value implies the size of the emitting region (R_B).

Table 4.2: Free parameters of Model 2. Parameters relating to the injected electron spectral distribution are given the subscript "T" for this model to distinguish them from the parameters of Model 1.

2006). In the late 1960s, radio and optical pulsations were detected spatially coincident with the Crab Nebula (Cocke et al., 1969; Staelin & Reifenstein, 1968), the remnant of a supernova explosion seemingly observed by Asian astronomers in 1054. These pulsations were detected with a period of 0.33 ms. It was quickly concluded that the nebula contains a rapidly rotating neutron star, what we now call a pulsar, that was formed during the supernova and is now the central engine of the nebula.

Shortly after their detection, Richards & Comella (1969) showed that the pulsations were slowing down at a rate of 36 ns per day. This spin down rate implies that kinetic energy is being dissipated at a rate of $\sim 5 \times 10^{38}$ ergs s^{-1}. This value is similar to the inferred rate at which energy is being supplied to the nebula (Gold, 1969). Given this similarity, a self-consistent magnetohydrodynamic model was developed that explains the main features of the nebula (Rees & Gunn, 1974; Kennel & Coroniti, 1984a,b).

Rees & Gunn (1974) proposed that in the region close to the central pulsar, the pulsar environment is unaffected by the surrounding nebula. This region extends up to some radius R_s, and within that radius, the energy flux from the pulsar streams outward, partly in the form of a relativistic wind that contains a toroidal magnetic field, and partly in the form of electromagnetic waves of frequency $\frac{1}{P} \simeq 30$ Hz. If the pulsar were completely isolated, the wind and low-frequency waves would eventually reach arbitrarily large radii. However, this is not true

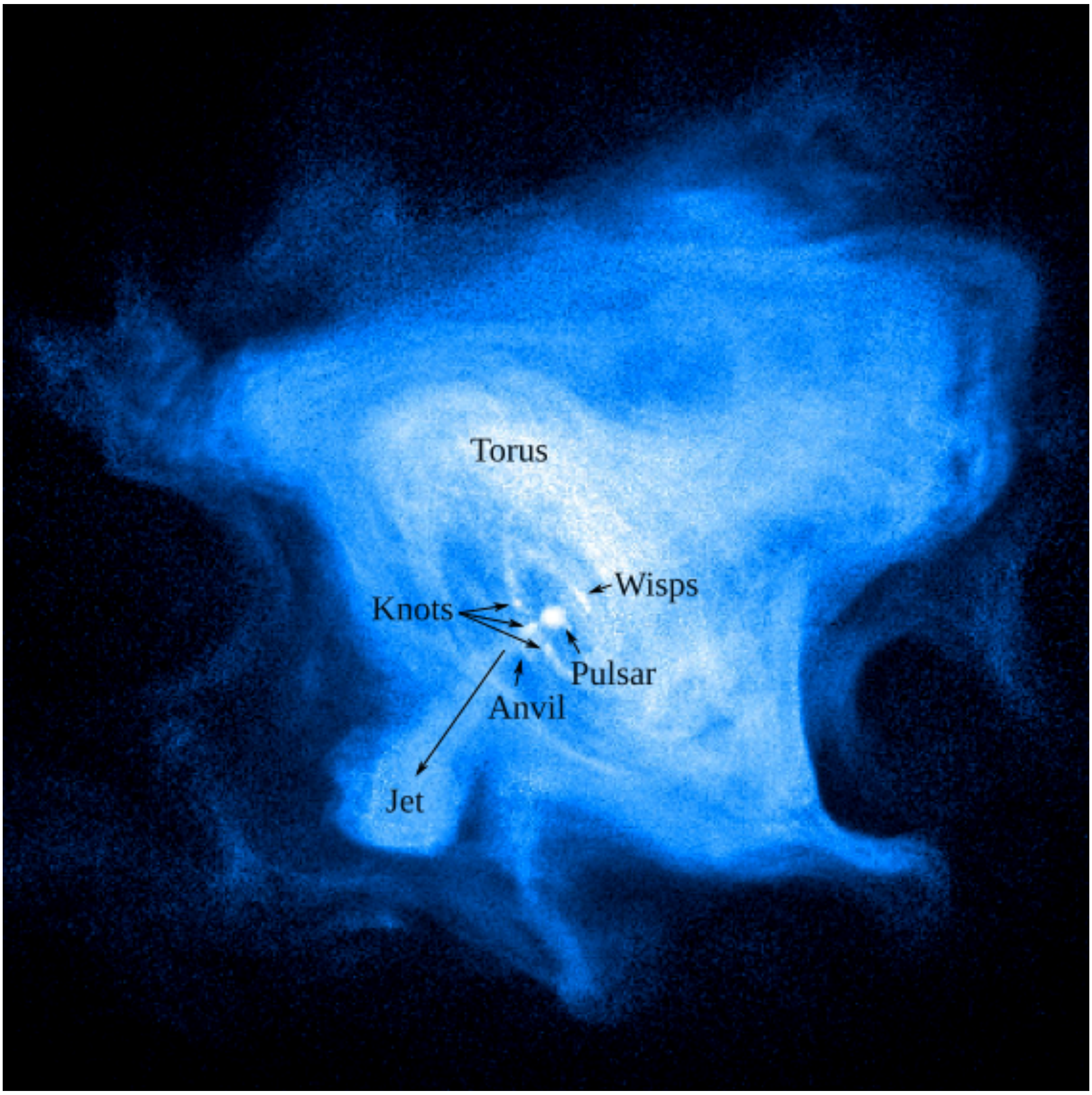

Figure 4.4: Chandra X-ray image of the Crab Nebula (credit: NASA/CXC/SAO/F. Seward et al.) showing the different features visible in the nebula. The pulsar lies at the centre, surrounded by an underluminous region that is thought to correspond to the pulsar wind. The wisps are believed to be the region in which the pulsar wind interacts with the surrounding nebula.

for a pulsar inside a nebular cavity, as all the energy stays within the volume that expands at $\dot{R}_{\text{nebula}} \ll c$. In this case, there is a characteristic radius (R_s) where the ram pressure balances the total magnetic and particle pressure within the bulk of the nebular volume. For a simple idealised model of the Crab Nebula, this places $R_s \simeq 3 \times 10^{17}$ cm. A shock transition must occur at R_s, and the authors tentatively associated this with the location of the wisps (see Figure 4.4 for an overview of the features present in the Crab Nebula).

The low-frequency waves are absorbed at R_s, most likely through synchrotron absorption, increasing the energy of the relativistic electrons being fed into the nebula. This implies that the continuum emission from the nebula is ordinary synchrotron radiation, and the magnetic field must be comparable with the equipartition value.

Unlike the low-frequency waves, the magnetic field carried by the wind is not destroyed. Instead, the flux accumulates in the body of the nebula and the magnetic energy builds up more rapidly than the particle energy. Beyond R_s, the bulk motions are subsonic and the magnetic stresses and particle pressure come more or less into equilibrium.

Assuming the continuum emission to be composed of just synchrotron radiation, the inferred relativistic electron spectrum in the nebula for a mean field of $\sim 5 \times 10^{-4}$ G breaks at $\gamma \simeq 10^5$ (~ 50 GeV) and $\gamma \simeq 5 \times 10^6$ (~ 2 TeV). These breaks derive from apparent changes in the slope of the continuum spectrum in IR and UV which can readily be seen in Figure 4.5. Electrons with $\gamma \gtrsim 10^5$ have synchrotron lifetimes $\lesssim 1000$ years, and so the break at this energy can be attributed to synchrotron losses. However, the break at $\gamma \simeq 5 \times 10^6$ must be a feature of the injection spectrum itself. The authors offer no convincing explanation for why the injection spectrum might have this form, but suggest that statistical acceleration may play a role and that such processes may be taking place at the location of the wisps.

Kennel & Coroniti (1984a) extended the model of Rees & Gunn (1974). They calculated the properties of the strong MHD shock that must stand in the wind of the Crab pulsar if it is to be confined, and also the nonrelativistic flow downstream of the shock. They found that the entire flow is critically dependent on the ratio of electromagnetic to particle energy fluxes in the pulsar wind. The boundary conditions imposed by the stellar envelope surrounding the nebula place the shock at a radial distance of $\simeq 3 \times 10^{17}$ cm. This is in agreement with Rees & Gunn (1974), and is consistent with the underluminous zone observed close around the pulsar.

4.3.1 New models for the Crab Nebula

The type of model described in the previous section, while capable of accounting for most of the observed spatial and spectral features, only predicts constant emission from the nebula. The discovery of flaring episodes at MeV γ-ray energies by the AGILE (Tavani et al., 2011), Figure 4.6, and *Fermi*-LAT (Abdo et al., 2011), Figure 4.7, teams was completely unexpected in this framework.

In response, many theories were developed to explain this new-found behaviour. While differing in the details, these models generally suggest one of three scenarios; instabilities in the termination

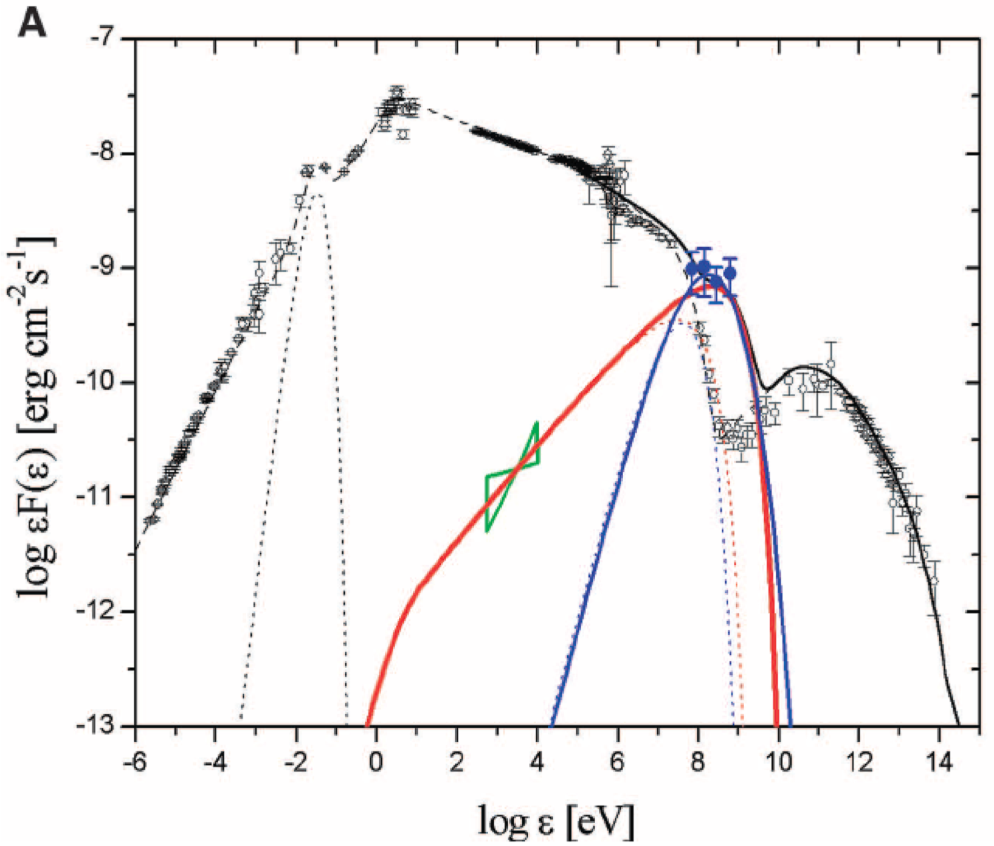

Figure 4.5: Spectrum of the Crab Nebula showing the average nebula emission in black. The AGILE flare data from September 2010 is indicated by the blue circles. The breaks at IR and UV energies are clearly noticeable. The far infrared bump is due to thermal emission from dust in the nebula. Figure from Tavani et al. (2011).

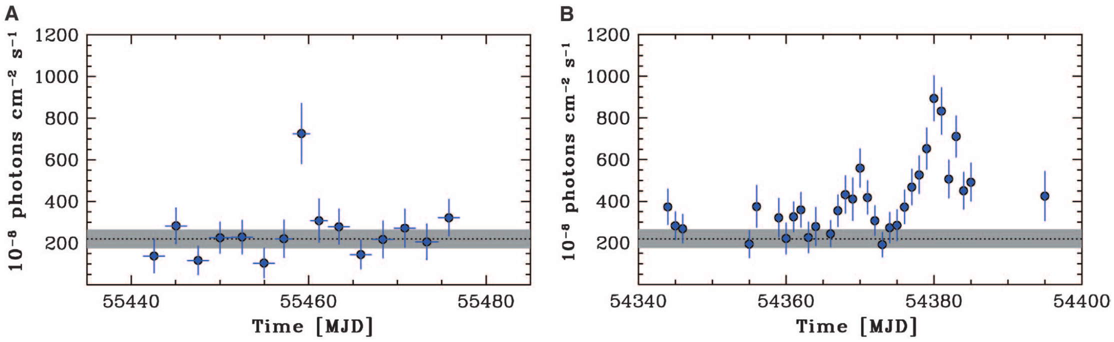

Figure 4.6: AGILE observations from 100 MeV to 5 GeV of flares from the Crab Nebula in September 2010 (A) and October 2007 (B) (Tavani et al., 2011).

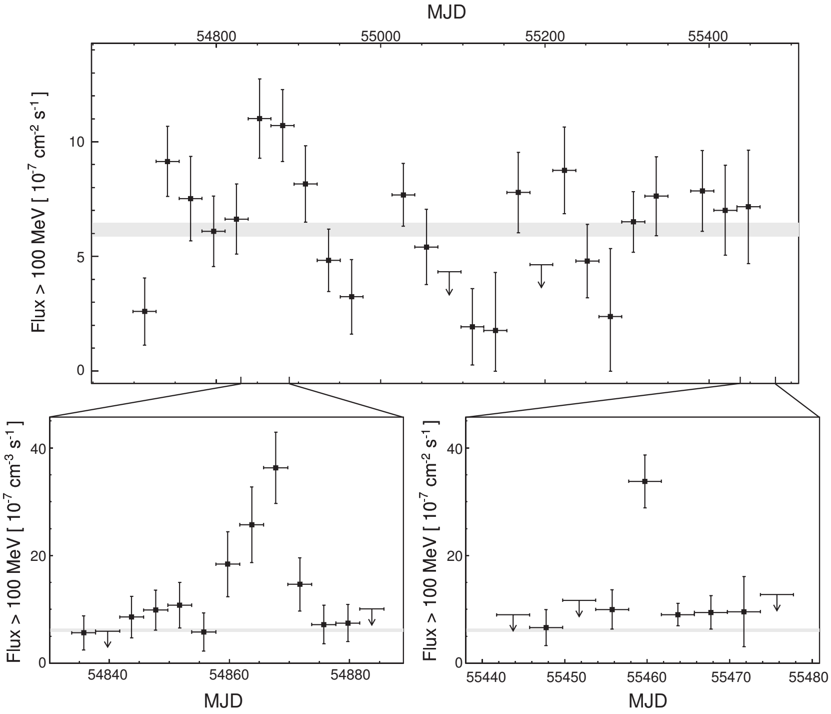

Figure 4.7: *Fermi*-LAT observations of the Crab Nebula, showing flares in February 2009 and September 2010 (Abdo et al., 2011). The flare seen in September 2010 coincides with that seen by AGILE.

shock, i.e., coming from the inner knot feature, (e.g., Komissarov & Lyutikov (2011)), particle acceleration due to magnetic reconnection events in the nebula (e.g., Bednarek & Idec (2011)), or plasma kink instabilities (e.g., Moser & Bellan (2012)) which may provide a framework for variability originating in the anvil region.

Bednarek & Idec (2011) suggest that the variable γ-ray emission originates behind the shock where the pulsar wind interacts with the nebula as a result of magnetic reconnection. This is the only model to date with predictions for the TeV behaviour, and is therefore of particular interest to the observations presented in Chapter 6. The model predicts TeV variability on the same timescales as those observed from the synchrotron nebula, as it is the same population of synchrotron-radiating electrons that upscatter soft photons into the VHE regime.

The authors suggest that the variability timescale on the order of days can be explained if the emission comes from only a part of the pulsar wind shock. They consider a scenario in which the shock is moving with a substantial Lorentz factor γ_s in an outward direction from the pulsar. The γ-ray emission is related to the region in the pulsar wind that is in the process of being decelerated at the pulsar wind shock. Given the relativistic motion of the shock, only γ-rays produced in a particular region can reach us, the observers. Figure 4.8 illustrates this basic scenario.

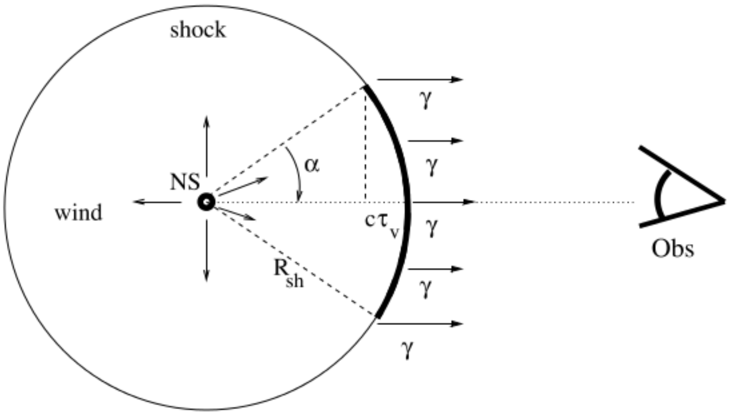

Figure 4.8: Schematic illustration of the emission scenario for the Crab Nebula (Bednarek & Idec, 2011). γ-rays are produced behind the shock (R_{sh}) in the region of strong deceleration of the pulsar wind. Only γ-rays produced in the region marked by the thick line, defined by the angle α, can reach us, the observers. However, the γ-rays arrive at different times due to the curvature of the shock itself. The angle α is related to the collimation of the γ-ray emission, which is caused by the relativistic motion of the emission region.

A lower limit on the magnetic field in the emission region was estimated, first using the observed break in the quiescent synchrotron spectrum at ~ 100 MeV and the minimum variability timescale, and also by extrapolating the magnetic field from the Crab pulsar surface up to the location of the first optical wisps. Both of these methods produce a lower limit of a few$\times 10^{-3}$ G, considerably larger than the magnetic field strength within the Crab nebula volume as a whole ($\sim 10^{-4}$ G).

The model assumes that the electrons are accelerated in the reconnection regions of the magnetic field in the pulsar wind before it reaches the shock region. This acceleration process circumvents the limit that would be imposed by synchrotron energy losses in a standard shock acceleration scenario. Given the observed shape of the spectrum from the Crab nebula, the electrons are assumed to reach an equilibrium spectrum described by a differential power law with index between $3.0 - 3.6$ and with a characteristic cut-off at $\gamma = 3 \times 10^{9}$ for flares. In this case, TeV variability is also expected from the same population of electrons upscattering either the microwave background radiation or very low-energy synchrotron radiation within the nebula. Such variability is interpreted to be of the order of $\sim 10\%$ above 1 TeV, and more substantial above 10 TeV.

4.4 Bibliography

Abdo, A. A., Ackermann, M., Ajello, M., et al., 2011; ‘Gamma-ray flares from the Crab Nebula.’ *Science (New York, N.Y.)*, vol. 331(6018):739

Acciari, V. A., Aliu, E., Aune, T., et al., 2009; ‘Multiwavelength Observations of a TeV-Flare from W Comae’. *The Astrophysical Journal*, vol. 707(1):612

Achterberg, A., Gallant, Y. A., Kirk, J. G., et al., 2001; ‘Particle acceleration by ultra-relativistic shocks: theory and simulations’. *Monthly Notices of the Royal Astronomical Society*, vol. 328(2):393

Aharonian, F., Akhperjanian, A. G., Bazer-Bachi, A. R., et al., 2007; ‘An Exceptional Very High Energy Gamma-Ray Flare of PKS 2155-304’. *The Astrophysical Journal*, vol. 664(2):L71

Albert, J., Aliu, E., Anderhub, H., et al., 2007; ‘Variable Very High Energy γRay Emission from Markarian 501’. *The Astrophysical Journal*, vol. 669(2):862

Bednarek, W., Idec, W., 2011; ‘On the variability of the GeV and multi-TeV gamma-ray emission from the Crab nebula’. *Monthly Notices of the Royal Astronomical Society*, vol. 414(3):2229

Böttcher, M., 2005; ‘A Hadronic Synchrotron Mirror Model for the ”Orphan” TeV Flare in 1ES 1959+650’. *The Astrophysical Journal*, vol. 621(1):176

—, 2010; ‘Models for the Spectral Energy Distributions and Variability of Blazars’. In ‘Fermi meets Jansky - AGN at Radio and Gamma-Rays’, , (eds. Savolainen, T., Ros, E., Porcas, R., et al.). Bonn, Germany

Böttcher, M., Chiang, J., 2002; ‘X-Ray Spectral Variability Signatures of Flares in BL Lacertae Objects’. *The Astrophysical Journal*, vol. 581(1):127

Böttcher, M., Harris, D. E., Krawczynski, H. (Eds.) , 2012; *Relativistic Jets from Active Galactic Nuclei*. Wiley-VCH

Cocke, W. J., Disney, M. J., Taylor, D. J., 1969; ‘Discovery of Optical Signals from Pulsar NP 0532’. *Nature*, vol. 221(5180):525

Dermer, C. D., Schlickeiser, R., Mastichiadis, A., 1992; ‘High-energy gamma radiation from extragalactic radio sources’. *Astronomy and Astrophysics*, vol. 256:L27

Fermi, E., 1949; ‘On the Origin of the Cosmic Radiation’. *Physical Review*, vol. 75(8):1169

Finke, J. D., Razzaque, S., Dermer, C. D., 2010; ‘Modeling the Extragalactic Background Light from Stars and Dust’. *The Astrophysical Journal*, vol. 712(1):238

Gaensler, B. M., Slane, P. O., 2006; ‘The Evolution and Structure of Pulsar Wind Nebulae’. *Annual Review of Astronomy and Astrophysics*, vol. 44(1):17

Giannios, D., Uzdensky, D. A., Begelman, M. C., 2009; ‘Fast TeV variability in blazars: jets in a jet’. *Monthly Notices of the Royal Astronomical Society: Letters*, vol. 395(1):L29

Gold, T., 1969; ‘Rotating Neutron Stars and the Nature of Pulsars’. *Nature*, vol. 221(5175):25

Kennel, C. F., Coroniti, F. V., 1984a; ‘Confinement of the Crab pulsar’s wind by its supernova remnant’. *The Astrophysical Journal*, vol. 283:694

—, 1984b; ‘Magnetohydrodynamic model of Crab nebula radiation’. *The Astrophysical Journal*, vol. 283:710

Kirk, J. G., Duffy, P., 1999; ‘Particle acceleration and relativistic shocks’. *Journal of Physics G: Nuclear and Particle Physics*, vol. 25(8):R163

Komissarov, S. S., Lyutikov, M., 2011; ‘On the origin of variable gamma-ray emission from the Crab nebula’. *Monthly Notices of the Royal Astronomical Society*, vol. 414(3):2017

Longair, M. S., 2011; *High Energy Astrophysics*. Cambridge University Press, 3rd editio ed.

Longair, M. S., 2011; *High Energy Astrophysics*. Cambridge University Press, 3 ed.

Lyubarsky, Y. E., 2005; ‘On the relativistic magnetic reconnection’. *Monthly Notices of the Royal Astronomical Society*, vol. 358(1):113

Maraschi, L., Ghisellini, G., Celotti, A., 1992; ‘A jet model for the gamma-ray emitting blazar 3C 279’. *The Astrophysical Journal*, vol. 397:L5

Massaro, E., Tramacere, A., Perri, M., et al., 2006; ‘Log-parabolic spectra and particle acceleration in blazars’. *Astronomy and Astrophysics*, vol. 448(3):861

Moser, A. L., Bellan, P. M., 2012; ‘Magnetic reconnection from a multiscale instability cascade.’ *Nature*, vol. 482(7385):379

Mücke, A., Protheroe, R. J., 2000; ‘Modeling the April 1997 flare of Mkn 501’. In ‘Proceedings of the 26th International Cosmic Ray Conference’, , (eds. Dingus, B. L., Salamon, M. H., Kieda, D. B.), vol. 515 of *American Institute of Physics Conference Series*, 149–153. American Institue of Physics

Narayan, R., Piran, T., 2012; 'Variability in blazars: clues from PKS 2155304'. *Monthly Notices of the Royal Astronomical Society*, vol. 420(1):604

Parker, E. N., 1957; 'Sweet's mechanism for merging magnetic fields in conducting fluids'. *Journal of Geophysical Research*, vol. 62(4):509

Petschek, H. E., 1964; 'Magnetic Field Annihilation'. *The Physics of Solar Flares*

Pohl, M., Schlickeiser, R., 2000; 'On the conversion of blast wave energy into radiation in active galactic nuclei and gamma-ray bursts'. *Astronomy and Astrophysics*, vol. 354:395

Rees, M. J., Gunn, J. E., 1974; 'The origin of the magnetic field and relativistic particles in the Crab Nebula'. *Monthly Notices of the Royal Astronomical Society*, vol. 167:1

Richards, D. W., Comella, J. M., 1969; 'The Period of Pulsar NP 0532'. *Nature*, vol. 222(5193):551

Rieger, F. M., Duffy, P., 2004; 'Shear Acceleration in Relativistic Astrophysical Jets'. *The Astrophysical Journal*, vol. 617(1):155

Rybicki, G. B., Lightman, A. P., 1979; *Radiative processes in astrophysics*. Wiley Interscience

Sikora, M., Begelman, M. C., Rees, M. J., 1994; 'Comptonization of diffuse ambient radiation by a relativistic jet: The source of gamma rays from blazars?' *The Astrophysical Journal*, vol. 421:153

Sokolov, A., Marscher, A. P., McHardy, I. M., 2004; 'Synchrotron Self-Compton Model for Rapid Nonthermal Flares in Blazars with Frequency-dependent Time Lags'. *The Astrophysical Journal*, vol. 613(2):725

Staelin, D. H., Reifenstein, E. C., 1968; 'Pulsating Radio Sources near the Crab Nebula - 1725616.pdf'. *Science*, vol. 162(3861):1481

Summerlin, E. J., Baring, M. G., 2012; 'Diffusive Acceleration of Particles at Oblique, Relativistic, Magnetohydrodynamic Shocks'. *The Astrophysical Journal*, vol. 745(1):63

Sweet, P. A., 1958; 'The Neutral Point Theory of Solar Flares'. *Electromagnetic Phenomena in Cosmical Physics*

Tavani, M., Bulgarelli, A., Vittorini, V., et al., 2011; 'Discovery of powerful gamma-ray flares from the Crab Nebula.' *Science (New York, N.Y.)*, vol. 331(6018):736

Tramacere, A., Giommi, P., Perri, M., et al., 2009; ‘Swift observations of the very intense flaring activity of Mrk421 during 2006. I. Phenomenological picture of electron acceleration and predictions for MeV/GeV emission’. *Astronomy and Astrophysics*, vol. 501(3):879

Tramacere, A., Massaro, E., Taylor, A. M., 2011; ‘STOCHASTIC ACCELERATION AND THE EVOLUTION OF SPECTRAL DISTRIBUTIONS IN SYNCHRO-SELF-COMPTON SOURCES: A SELF-CONSISTENT MODELING OF BLAZARS FLARES’. *The Astrophysical Journal*, vol. 739(2):66

Chapter 5

Multiwavelength observations of the blazar 1ES 1959+650

The BL Lac object 1ES 1959+650 was discovered in 1993 with redshift $z = 0.047$ (Schachter et al., 1993). It was later found to be a source of TeV emission by the Utah Seven Telescope Array (Nishiyama, 1999) and the Whipple 10 m Telescope (Holder et al., 2003). It has exhibited dramatic VHE flaring episodes, most notably on June 4, 2002, when a γ-ray flare without an increase in X-ray emission was detected from the source, providing the first unambiguous example of an "orphan" γ-ray flare (Krawczynski et al., 2004; Holder et al., 2003; Daniel et al., 2005).

Krawczynski et al. (2004) modelled this orphan flare with a simple SSC model and found that this under-predicted the observed radio and optical fluxes. The authors examined mechanisms for producing an orphan γ-ray flare in the context of a SSC model and found that it could not be fully explained by one-zone SSC models. Multi-component SSC models may account for orphan γ-ray flares either through an extra low-energy electron population or a second high-density electron population confined to a small emission volume. Sokolov et al. (2004) showed that it is also possible for flares to occur with frequency-dependent time lags through shock collision in the blazar jet. Hadronic models were also developed as alternative models for this event (Böttcher, 2005).

This source was monitored as part of the VERITAS blazar monitoring program in the hopes of observing it in another dramatic outburst. Over seasons of these monitoring observations, a significant detection was accumulated of the source in its non-flaring state. This chapter reports on multiwavelength observations of 1ES 1959+650 from UV to VHE γ-rays during the period $2007-2011$.

The data presented in this chapter were published in 2013 (Aliu et al., 2013). For this publication, model parameters were provided by a collaborator, Prof. Markus Böttcher, using proprietary code. For completeness, the SED was remodelled for this chapter using the blazar SED tool[1] (Tramacere et al., 2011, 2009; Massaro et al., 2006). This tool consists of a web interface to a numerical code that reproduces radiative and accelerative processes acting in blazar jets. The original parameters from the publication are also presented for comparison. The source is considered to be in a low flux state during the sampling of observations covered here due to a mean recorded VHE γ-ray flux > 1 TeV of 23% of the Crab Nebula flux.

5.1 Multiwavelength Observations and Analysis

5.1.1 VERITAS

VERITAS observations of 1ES 1959+650 were carried out between November 13, 2007 and October 28, 2011 (MJD $54417-55862$) as part of a routine blazar program monitoring for enhanced emission. The source never met the threshold criteria for target of opportunity observations of enhanced VHE emission, so only minimal monitoring data were taken. On December 2, 2010 (MJD 55532), the Whipple 10 m Telescope observed the source in an apparent state of elevated emission. VERITAS was alerted and ToO observations were taken. While it was confirmed that the measured flux was greater than average by a factor of ~ 2 (the source was seen at ~ 50 % Crab Nebula flux), the increase was not deemed sufficient to trigger ToO observations.

The data were taken in wobble mode, with a $0.^\circ5$ offset from the source position in each of the four cardinal directions alternately so that the background can be estimated from simultaneously gathered data, and systematic effects in the background estimation cancel out (Aharonian et al., 2001; Berge et al., 2007). Observations were conducted in a range of zenith angles $34^\circ - 53^\circ$ using the full four-telescope array, giving a total of 7.6 hours of live time on the source in 14 separate nights over four years.

The data are analysed as described in Chapter 3. In this analysis, images composed of fewer than five pixels are rejected. For each image, mean scaled width and mean scaled length parameters are required to be in the range $0.05-1.15$ and $0.05-1.3$ respectively (Konopelko et al., 1999).

---

[1] `http://isdc-web00.isdc.unige.ch/sedtool/SED_Web_tool/html_js/SED_Web_tool/SED_start_test.html`

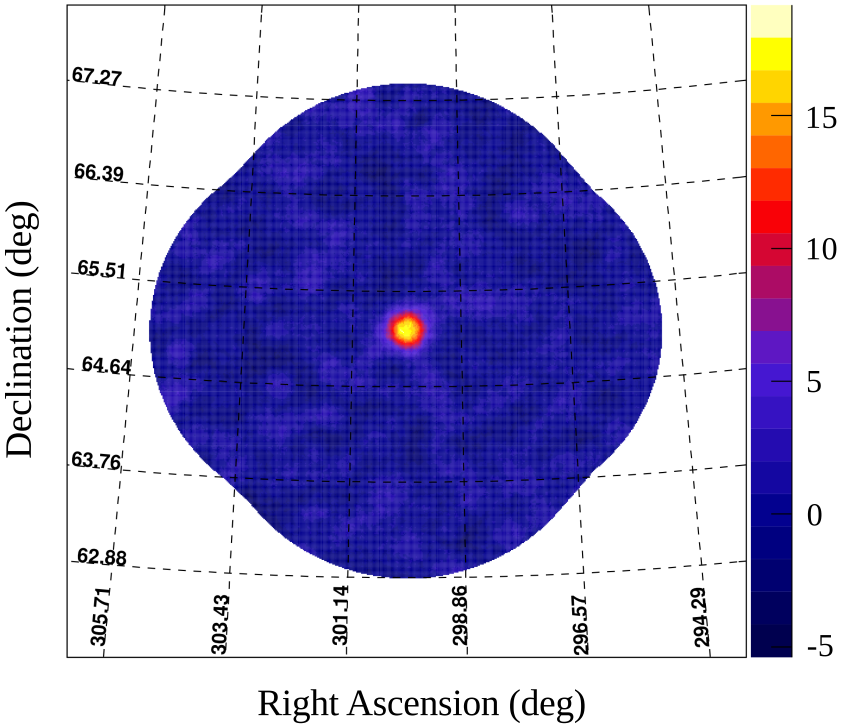

Figure 5.1: VERITAS smoothed significance map of the region around 1ES 1959+650 showing a clear detection of a point source. The colour scale shows the number of standard deviations above the background (σ).

The altitude of the maximum Cherenkov emission from the reconstructed shower is required to be higher than 7 km above the array. A circular region of radius $0^\circ\!.1$ centered on the source coordinates is defined from which γ-ray like events are selected.

For the low elevation observations of 1ES 1959+650, the energy threshold is found to increase to $\sim$800 GeV from $\sim$100 GeV achievable at higher elevations. All VERITAS fluxes are therefore quoted above 1 TeV. 1ES 1959+650 is detected at $16.4\,\sigma$ with an average flux of $(3.97 \pm 0.37) \times 10^{-12}$ photons cm^{-2} s^{-1} (or $(7.54 \pm 0.7) \times 10^{-12}$ ergs cm^{-2} s^{-1}, equivalent to $\sim 23\,\%$ Crab Nebula flux) above 1 TeV. This corresponds to 268 excess γ-rays at the source location at RA= $19^h59^m59^s \pm 20^s_{\text{stat}}$ and Dec= $65°9'.25 \pm 0'.34_{\text{stat}}$ (J2000 coordinates). The source location is determined by fitting a 2-dimensional Gaussian to the uncorrelated excess map. The source position is then equal to the centre of the distribution. The observed VERITAS signal is consistent with a point source, and the source is designated VER J1959+651. A significance map of the source region is shown in Figure 5.1.

A nightly light curve is shown in the top panel of Figure 5.2. A constant flux is fit to the light curve, using the low significance flux points corresponding to the upper limit values. This yields $\chi^2/NDF = 5.37$ and fit probability 3.43×10^{-9}, providing $> 5\,\sigma$ evidence for flux variability. It can be seen that the variability amplitude with respect to the average is of order ~ 2.

A time-averaged differential spectrum, shown in Figure 5.3, is constructed from the entire data set. The spectrum is fit with a power law of form

$$\frac{dN}{dE} = N \left(\frac{E}{E_0} \right)^{-\Gamma}, \tag{5.1.1}$$

where E_0 is the pivot energy and is set at 1 TeV. The fit parameters are $N = (6.12 \pm 0.53_{\text{stat}} \pm 2.45_{\text{sys}}) \times 10^{-12}$ cm^{-2} s^{-1} TeV^{-1}, $\Gamma = 2.54 \pm 0.08_{\text{stat}} \pm 0.3_{\text{sys}}$, with $\chi^2/NDF = 1.25$ and a fit probability of 0.28.

5.1.2 Fermi-LAT

Analysis is performed on all *Fermi*-LAT observations of 1ES 1959+650 since the satellite's launch through December 2, 2011 (MJD $54682 - 55897$). The LAT analysis procedure is described in Chapter 3, but the specifics of this analysis are reiterated here for convenience. Events are extracted from a region of interest (ROI) of radius 10° centered on the coordinates of 1ES 1959+650, taken from the *Fermi*-LAT second source catalog (2FGL) (Nolan et al., 2012). Events from the *diffuse class* with zenith angle $< 100^\circ$ and energy in the range $0.3 - 100$ GeV are selected. Data taken when the rocking angle of the spacecraft is greater than 52° are discarded to avoid contamination from photons from the Earth's limb. Source significance and spectral parameters are computed using an unbinned likelihood analysis with the LAT Science Tools[2].

A background model including all γ-ray sources from the 2FGL within 12° of 1ES 1959+650 is created. Remaining excesses in the ROI are modeled as point sources with a simple power-law spectrum. The spectral parameters of sources within the ROI are left free during the minimisation process. The galactic and extragalactic diffuse γ-ray emission as well as the residual instrumental background are included using the recommended model files[3].

A light curve is calculated in 4-week bins and is shown in the third panel of Figure 5.2. Flux variability up to a factor of ~ 2 above the mean is evident; fitting the light curve with a constant flux gives a $\chi^2/NDF = 2.26$ and a fit probability of 9.24×10^{-6}. The data are then rebinned into 4-week bins centred on VERITAS observations, and data from intervening periods without VERITAS observations are removed. The resulting light curve is shown in Figure 5.4. This contemporaneous data set shows no evidence of variability with a constant flux fit yielding $\chi^2/NDF = 1.33$ and a fit probability of 0.26.

---

[2] ScienceTools-v9r23p1 with P7SOURCE_V6 instrument response function

[3] gal_2yearp7v6_v0, iso_p7v6clean

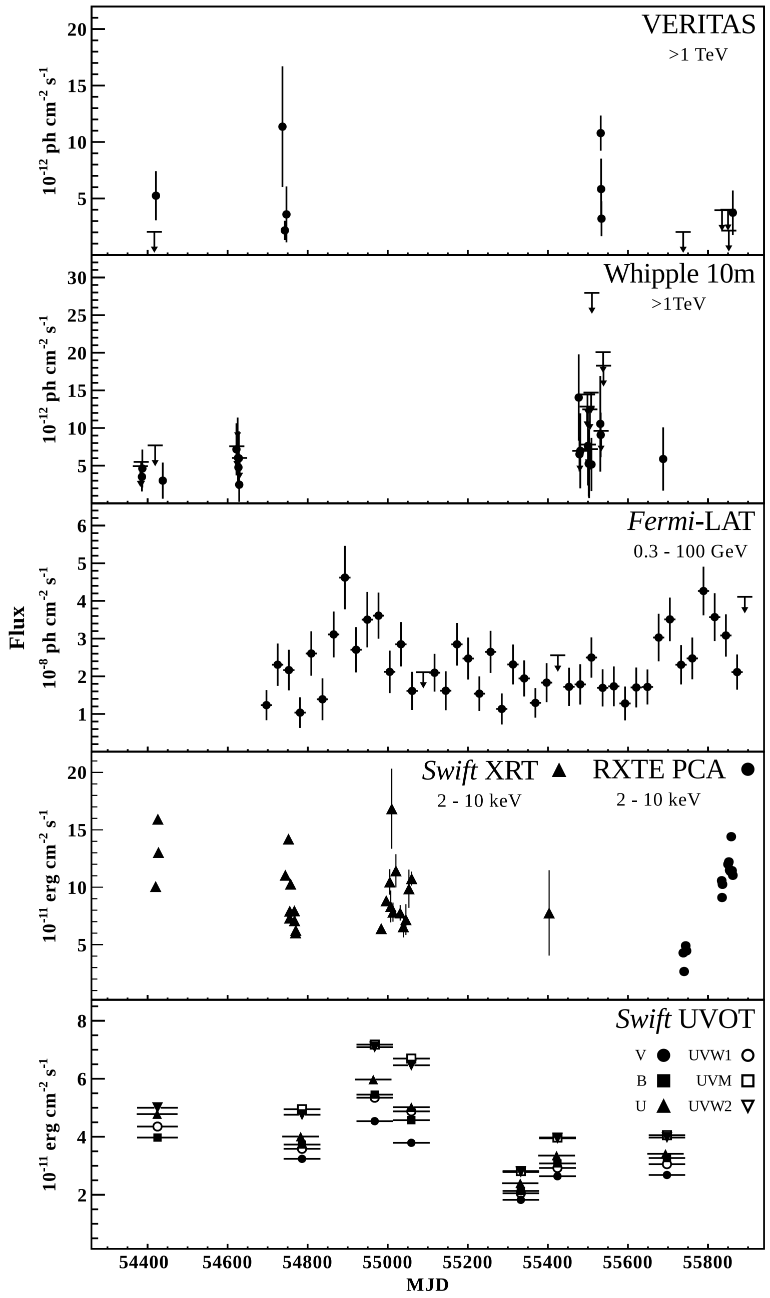

Figure 5.2: Light curves of 1ES 1959+650 in all energy bands analysed for this work[†]. VERITAS and Whipple light curves are displayed in nightly bins; the *Fermi*-LAT light curve is shown in 4-week bins; RXTE PCA and *Swift* XRT are binned by observation, the duration of which can vary; the *Swift* UVOT light curve is in 90-day bins. Strong variability is seen in the X-ray regime on the order of 48 hours from the RXTE observations (panel 4), however, this timescale is dominated by the time between observations. Other wavebands exhibit more stable emission, with γ-rays (panels $1-3$) showing variability on the order of ~ 2. For VERITAS and Whipple data sets, upper limits are calculated for points with a significance $< 1\sigma$. For *Fermi*-LAT, upper limits are calculated for bins with $TS < 3$.

[†] Whipple 10 m Telescope and *Swift* UVOT data are shown for completeness, but were not analysed by the author.

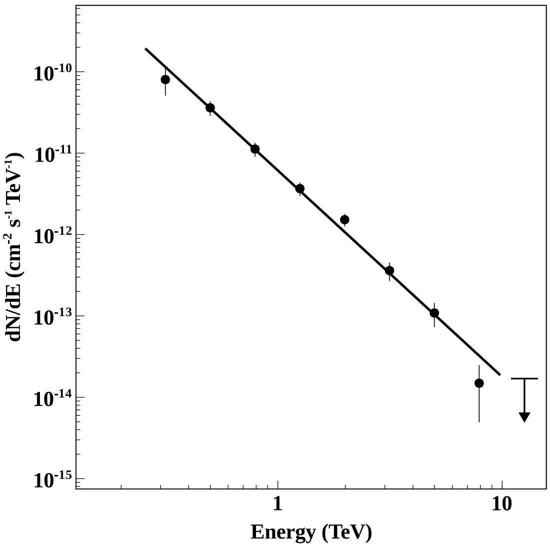

Figure 5.3: VERITAS time-averaged differential spectrum of 1ES 1959+650 fit with a power law (see Equation 5.1.1); $N = (6.12 \pm 0.53_{\text{stat}} \pm 2.45_{\text{sys}}) \times 10^{-12}$ cm^{-2} s^{-1} TeV^{-1}, $\Gamma = 2.54 \pm 0.08_{\text{stat}} \pm 0.3_{\text{sys}}$, and $E_0 = 1$ TeV.

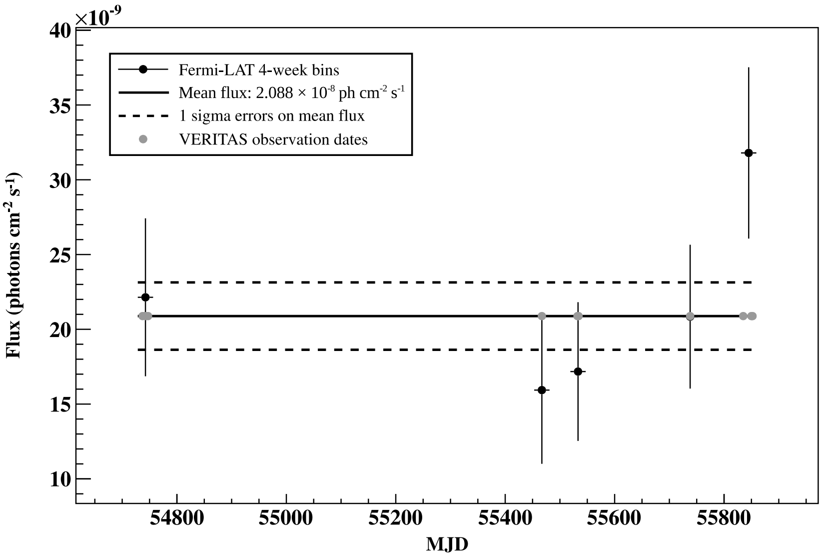

Figure 5.4: *Fermi*-LAT light curve of 1ES 1959+650 in 4-week bins centred on VERITAS observations of the source. VERITAS observation dates are marked in grey and *Fermi*-LAT fluxes for the corresponding bins are shown in black. The mean of the *Fermi*-LAT points is marked with the solid line, and the $1\,\sigma$ errors from the mean are indicated with the dashed lines.

The source is detected with a test statistic of 2620 ($\simeq 50\,\sigma$) with an average flux of $(2.16 \pm 0.09) \times 10^{-8}$ photons cm^{-2} s^{-1} (or $(1.89 \pm 0.08) \times 10^{-11}$ ergs cm^{-2} s^{-1}). A flux-index correlation study is performed on the entire data set, the result of which is shown in Figure 5.5. The Pearson product-moment correlation coefficient is found to be 0.37 ± 0.15 implying a medium level of linear correlation. The error is calculated using the standard method of error propagation (e.g., Lindberg, 2000). The Kendall tau rank correlation test may be more appropriate for these data, as it makes no assumptions about the functional form of the correlation. Therefore, the Kendall tau rank coefficient is also calculated and found to be 0.24 with a two-sided significance level of 0.03. The absence of a strong correlation in either of these tests is expected in the context of Abdo et al. (2010b), which found no significant flux-index correlation effect for HBLs detected by *Fermi*-LAT. It is interesting to note however, that the tendency for a softer spectral index with brighter source state seen in Figure 5.5 is also apparent for the average of the eight brightest representatives of the HBL subclass in Figure 5 of Abdo et al. (2010b), albeit an insignificant effect in that work.

A differential spectrum is produced from the entire data set and a second spectrum is constructed from the contemporaneous data set. Both are fit with a power law of form given in Equation 5.1.1 with E_0 fixed at $1402.26\,$MeV, and are found to be fully consistent. Parameters obtained from the whole data set are $N = (3.33 \pm 0.12) \times 10^{-12}$ cm^{-2} s^{-1} MeV^{-1}, $\Gamma = 1.99 \pm 0.03$. Parameters for the contemporaneous data set are $N = (3.34 \pm 0.72) \times 10^{-12}$ cm^{-2} s^{-1} MeV^{-1}, $\Gamma = 1.98 \pm 0.18$. These results are similar to the 2FGL values of $N = (2.9 \pm 0.12) \times 10^{-12}$ cm^{-2} s^{-1} MeV^{-1} and $\Gamma = 1.94 \pm 0.03$. An alternative spectral model was not tested in this analysis.

Butterfly representations of the confidence region for the spectral flux are produced for both spectra. These are not calculated in a truly rigorous manner, but are rather approximated. The power law energy spectrum is linear in log-log space,

$$\log\left(\frac{dN}{dE}\right) = \log N - \Gamma \log\left(\frac{E}{E_0}\right). \tag{5.1.2}$$

In this case, the error on $\log\left(\frac{dN}{dE}\right)$ is given by

$$\sigma_{\log\left(\frac{dN}{dE}\right)} = \sqrt{\frac{\sigma_N^2}{N^2} + \sigma_\Gamma^2 \log^2\left(\frac{E}{E_0}\right)}, \tag{5.1.3}$$

where σ_N and σ_Γ are the errors on the flux normalisation and spectral index respectively. The butterfly region is constructed by creating the upper and lower boundaries such that

$$\log\left(\frac{dN}{dE}\right) = \log N - \Gamma \log\left(\frac{E}{E_0}\right) \pm \sigma_{\log\left(\frac{dN}{dE}\right)}. \tag{5.1.4}$$

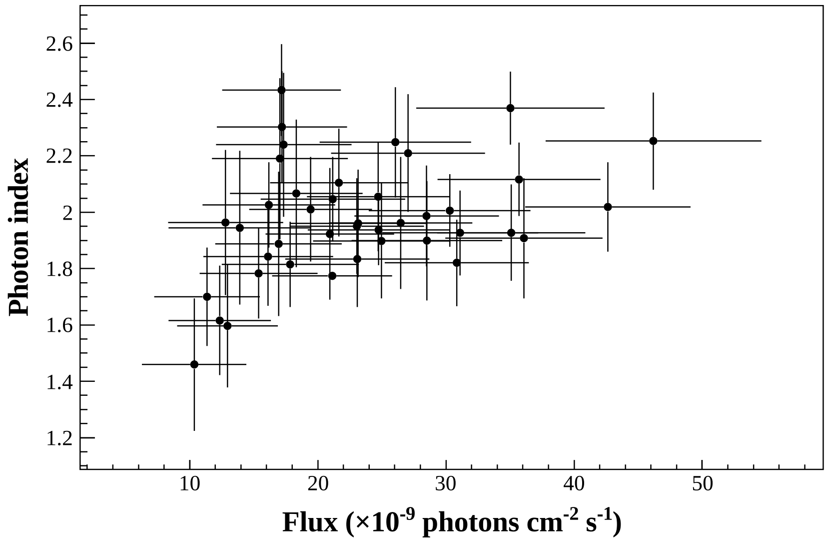

Figure 5.5: Flux-index correlation of *Fermi*-LAT data. The Pearson product-moment correlation coefficient is found to be 0.37 ± 0.15 implying a medium level of linear correlation.

At the pivot energy $E = E_0$,

$$\log\left(\frac{dN}{dE}\right) = \log N \pm \frac{\sigma_N}{N}, \tag{5.1.5}$$

independent of σ_Γ. At the limits of the spectrum, where $E \gg E_0$ or $E \ll E_0$, the boundaries asymptotically approach

$$\log\left(\frac{dN}{dE}\right) = \log N - (\Gamma \pm \sigma_\Gamma)\log\left(\frac{E}{E_0}\right), \tag{5.1.6}$$

which are a pair of straight lines independent of σ_N.

Using these equations, the six points defining the area of the butterfly plot are calculated, and are shown connected by straight lines (Figures 5.9-5.11).

5.1.3 RXTE PCA

The PCA data set comprises observations of 1ES 1959+650 during the period June 26, 2011 to October 28, 2011 (MJD $55738 - 55862$). A table summarising these observations can be found in Appendix A. Analysis of PCA data is performed on *Standard-2 mode* data following the RXTE Cook Book (RXTE Guest Observer Facility, 2006) and as described in Chapter 3, using the HEASoft[4] and XSPEC[5] packages. GTIs are produced for data in which the Earth elevation angle is $> 10^\circ$, the pointing offset $< 0\overset{\circ}{.}0$, the time since the last South Atlantic Anomaly passage > 30 minutes, and the electron contamination of the data < 0.1. A deadtime correction factor is calculated individually for each observation.

---

[4] HEASoft version 6.11.1

[5] XSPEC version 12.7

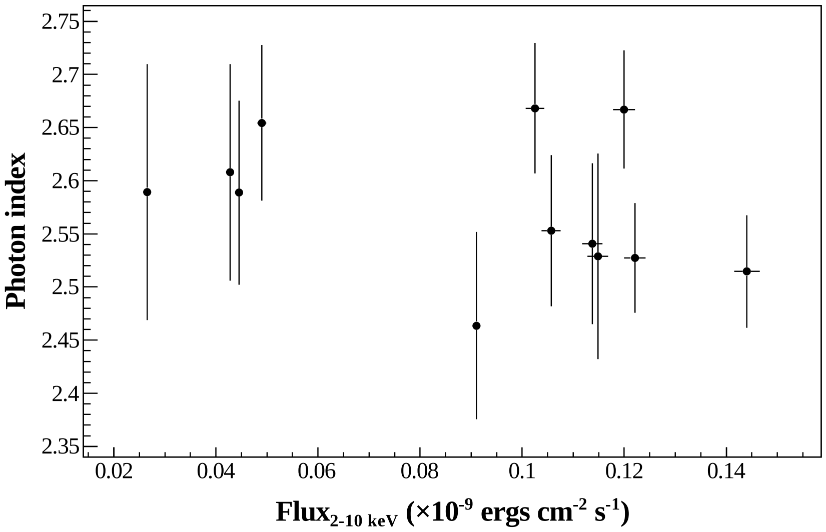

Figure 5.6: Flux-index plot of RXTE PCA data showing no significant variation of photon index with flux level.

A light curve binned by observation (durations vary between ~0.4 and ~2.5 ks) is shown in the fourth panel of Figure 5.2 and exhibits flux variability of a factor of ~4 throughout the data set. This variability is seen on the timescale of 48 hours, dominated by the time between observations. No significant variability within single observations is present. The photon index is found to be constant for all flux levels (see Figure 5.6). A constant index is fit to the data, yielding $\chi^2/NDF = 1.17$ and a fit probability of 0.29. This stable index is in contrast to the source behaviour reported in Giebels et al. (2002), in which the X-ray index was found to harden with increasing source brightness in the same energy range (2 - 10 keV).

A differential time-averaged spectrum is produced from the top layer only and fit in the range $3 - 10$ keV with a power law of the form given in Equation 5.1.1 with $E_0 = 1$ keV and an extra factor of K on the right hand side, where K is a multiplicative constant to correct for deadtime. The fit is performed in XSPEC using the model `constant*po`, and freezing the `constant` component to K, the deadtime correction factor which is calculated to be 1.02 for the entire data set. Fit results are $N = (7.27 \pm 0.23) \times 10^{-2}$ cm^{-2} s^{-1} keV^{-1} and $\Gamma = 2.63 \pm 0.02$ with $\chi^2/NDF = 1.76$ and a fit probability of 0.04.

An average differential spectrum is also produced using only the three observations of 1ES 1959+650 that are truly simultaneous with VERITAS observations. The model parameters are found to be $N = (7.90 \pm 0.46) \times 10^{-2}$ cm^{-2} s^{-1} keV^{-1} and $\Gamma = 2.58 \pm 0.04$ in agreement with the full time-averaged spectral parameters, with an improved goodness-of-fit, $\chi^2/NDF = 1.23$.

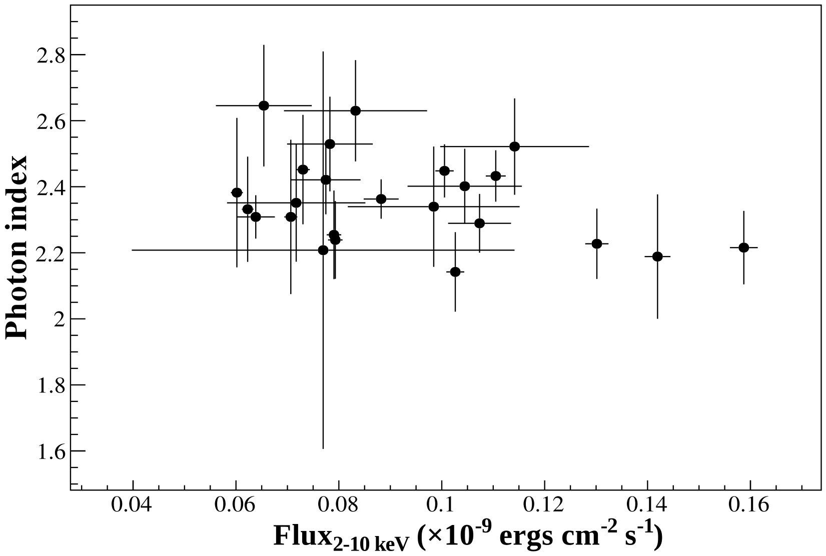

Figure 5.7: Flux-index plot of *Swift* XRT data showing no significant variation of photon index with flux levels.

5.1.4 Swift XRT

Swift XRT observations of 1ES 1959+650 taken in *photon counting mode* are analysed as described in Chapter 3 (a table summarising these observations can be found in Appendix A). A correction for pile-up is applied individually to each observation by fitting a King function (see Equation 3.4.2) to the data and using an annular source selection region, the inner radius of which is set to the value at which the fit and data diverge for that particular observation. This analysis is completed using the same HEASoft and XSPEC packages as in §5.1.3.

A light curve binned by observation is produced, and the flux and flux variability is found to be consistent with results from RXTE PCA. This light curve is shown in the fourth panel of Figure 5.2, showing variability over the course of the observations up to a factor of ~ 3. As with RXTE PCA data, the photon index is found to be stable for all flux levels (see Figure 5.7) with a fit with constant index yielding $\chi^2/NDF = 0.93$ and a fit probability of 0.55.

No XRT observations of 1ES 1959+650 occurred simultaneously with VERITAS observations, so only one time-averaged differential spectrum (see Figure 5.8) is produced and binned with 500 events per bin. The spectrum is fit in the range $0.3 - 10$ keV, ignoring all bad channels, with a photo-absorbed power law (the `phabs*po` model in XSPEC, using the default absorption cross-section) of form $dN/dE = \exp\left[-n_H\,\sigma(E)\right] N(E/E_0)^{-\Gamma}$. Free parameters are returned as $n_H = (1.57 \pm 0.05) \times 10^{21}$, $N = (6.36 \pm 0.12) \times 10^{-2}$ cm^{-2} s^{-1} keV^{-1}, and $\Gamma = 2.4 \pm 0.02$ with $\chi^2/NDF = 1.68$ and a fit probability of 5.2×10^{-3}. The galactic hydrogen density obtained from this fit is larger than the measured value of 1.0×10^{21} reported in Kalberla et al. (2005).

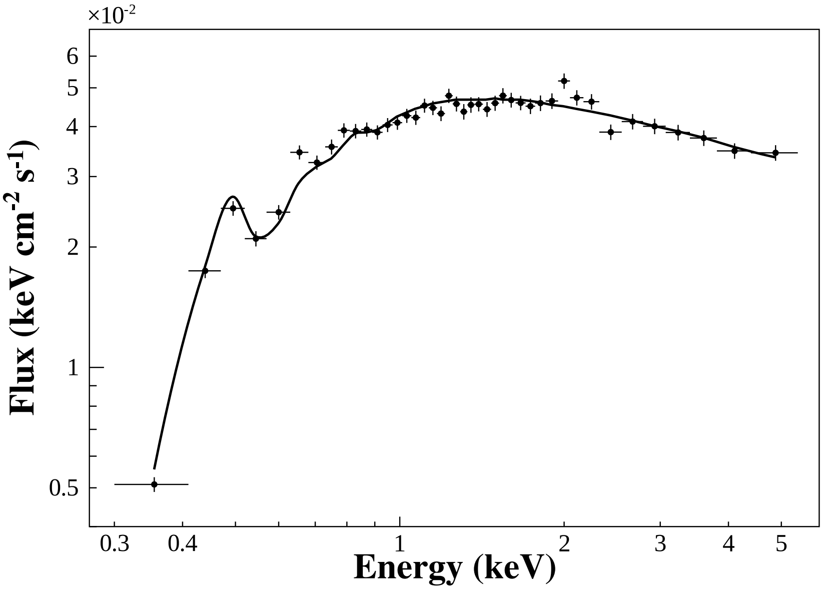

Figure 5.8: Time-average differential spectrum measured with *Swift* XRT in the range $0.3-10$ keV, fit with a photo-absorbed power law of form $dN/dE = \exp\left[-n_H\,\sigma(E)\right] N(E/E_0)^{-\Gamma}$; $n_H = (1.57 \pm 0.05) \times 10^{21}$, $N = (6.36 \pm 0.12) \times 10^{-2}$ cm^{-2} s^{-1} keV^{-1}, and $\Gamma = 2.4 \pm 0.02$.

Freezing the n_H parameter to the value of Kalberla et al. (2005) degrades the goodness-of-fit (in this case $\chi^2/\mathit{NDF} = 5.76$ with a fit probability 1.36×10^{-28}). It is found that a photo-absorbed log parabolic model (the `phabs*logpar` model in XSPEC) does not provide a better fit than the original power law model, yielding a $\chi^2/\mathit{NDF} = 1.72$ with a fit probability 3.77×10^{-3}.

5.2 Broadband SED and modelling

Multiwavelength SEDs are constructed from VERITAS, *Fermi*-LAT, RXTE PCA and *Swift* UVOT data. The time-averaged spectrum from the entire VERITAS data set provides the VHE γ-ray information. While there is evidence for flux variability in the VERITAS observations, there are not enough data to produce time-resolved spectra. The spectrum from the *Fermi*-LAT data set contemporaneous with VERITAS is used, removing any bias in this part of the SED due to flux variability; there is clear variability over the course of the entire LAT data set whereas the LAT data set contemporaneous with VERITAS shows no evidence of variability. The stability of the *Fermi*-LAT flux contemporaneous with the VERITAS observations indicates that the entire inverse-Compton component of the SED is likely to be stable. In this case, the time-averaged VERITAS spectrum is a reasonable representation of the VHE component of the source.

The UVOT data is coarsely binned, so no attempt was made to extract regions (quasi-) simultaneous with VERITAS, and a time-averaged spectrum from the entire data set was used.

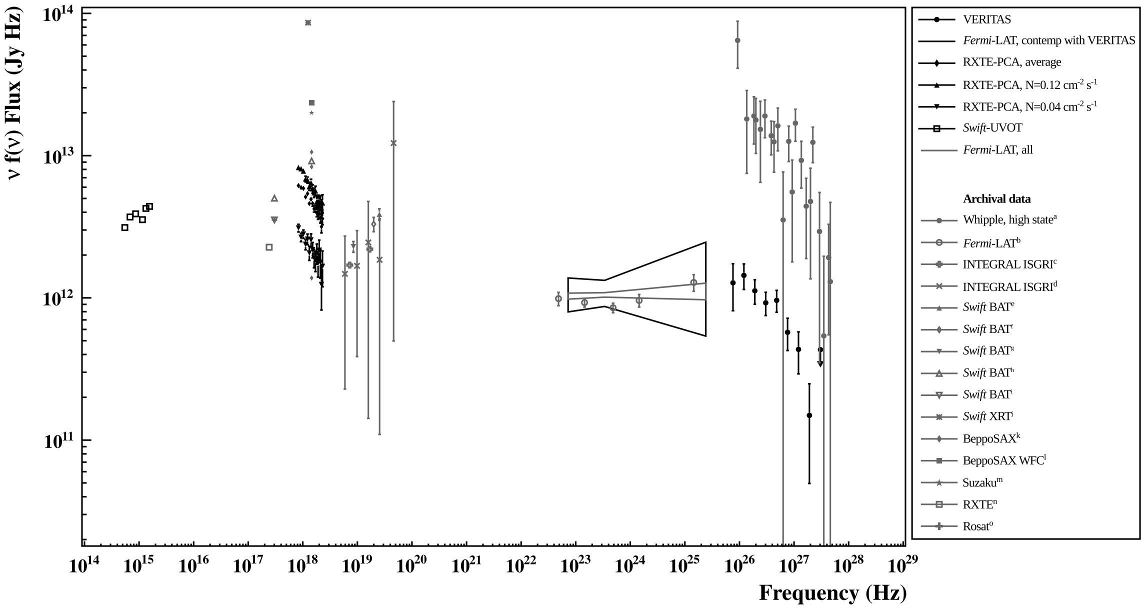

Figure 5.9: Current and previous observations of 1ES 1959+650. The *Fermi*-LAT spectra produced in this work are represented by butterfly plots (grey for the time-averaged spectrum, black for the contemporaneous spectrum), while data points are used for all other instruments. Data analysed in this work are shown in black and archival data are shown in grey for comparison. [a]Daniel et al. (2005); [b]Nolan et al. (2012); [c]Beckmann et al. (2009); [d]Bottacini et al. (2010); [e]Tueller et al. (2010); [f]Cusumano et al. (2010); [g]Ajello et al. (2009); [h]Winter et al. (2009); [i]Tavecchio et al. (2010); [j]Maselli et al. (2010); [k]Donato et al. (2005); [l]Verrecchia et al. (2007); [m]Tagliaferri et al. (2008); [n]Resconi et al. (2009); [o]Massaro et al. (2009)

While this may introduce a slight systematic bias on the statistical error at low energies, it is not expected that this should alter the main result of the modeling.

Significant variability is observed in the RXTE PCA X-ray data, even within the three observations that were taken simultaneously with VERITAS observations. However, as the X-ray statistics are high, it is feasible to create spectra for the individual observations, as well as an average spectrum from the three observations. It is found that the photon index is consistent within errors for the different X-ray spectra, but the normalisation is variable.

Three broadband SEDs are then formed, differing only in the X-ray regime; one SED with the highest normalisation X-ray spectrum, one with the lowest normalisation X-ray spectrum, and one using the average X-ray spectrum. This provides the opportunity to investigate the possible cause of large variability in X-rays with fairly steady emission in other regimes, which is in contrast to the orphan γ-ray variability previously observed in this source. Figure 5.9 shows the data analysed in this work (black) compared to archival data on this source (grey), highlighting the low TeV state observed.

The SEDs are modelled using the blazar SED tool (Tramacere et al., 2011, 2009; Massaro

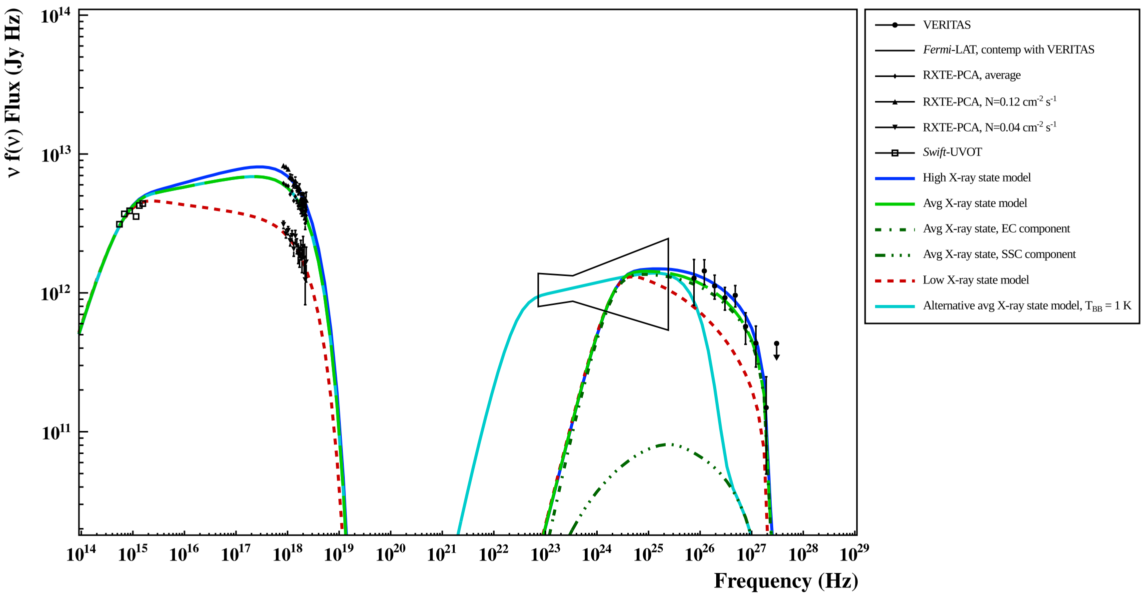

Figure 5.10: Observed SEDs and corresponding models of 1ES 1959+650. The solid (blue) line corresponds to the model for the highest X-ray normalisation, the dotted (red) line shows the model for the lowest X-ray normalisation, and the dashed (green) line represents the model for the time-averaged X-ray spectrum. It is seen that none of these models provides an accurate representation of the *Fermi*-LAT spectrum. The solid cyan line shows an alternative model for the time-averaged X-ray SED in which the temperature of the dust is set to be extremely cold (1 K). In this case, the *Fermi*-LAT spectrum is well described, but the VHE flux is completely underestimated.

et al., 2006). The model provided by this tool is described in Chapter 4. In this analysis the electron energy distribution is chosen to be a power law of index q_T with low- and high-energy cutoffs, $\gamma_{T,\,\mathrm{min}}$ and $\gamma_{T,\,\mathrm{max}}$ respectively. The SSC contribution to the IC component of the SED is found to be insufficient to represent the data. An EC component on a thermal blackbody is therefore added, motivated by the known presence of dust in the central environment of 1ES 1959+650 (Fumagalli et al., 2012).

It is found that the X-ray variability can be modelled by changing only the index of the electron spectrum. These models provide a reasonable representation of the data, but tend to underestimate the flux at a few hundred MeV. To create a model that well describes the shallow *Fermi*-LAT spectrum, the temperature of the dust supplying the seed photons for the EC component can be set to be extremely cold ($\sim$1 K). In this case, the flux at a few hundred MeV is reproduced by the IC component, but the VHE flux is completely underestimated. The data and models are shown in Figure 5.10, and the parameters of the models are shown in Table 5.1.

Parameter	**High X-ray**	**Low X-ray**	**Avg. X-ray**	**Alternative avg. X-ray**
N (cm^{-3})	2×10^{-4}	2×10^{-4}	2×10^{-4}	2×10^{-4}
$\gamma_{T,\ \mathrm{min}}$	1.3×10^{4}	1.3×10^{4}	1.3×10^{4}	1.3×10^{4}
$\gamma_{T,\ \mathrm{max}}$	9×10^{5}	9×10^{5}	9×10^{5}	9×10^{5}
q_T	2.8	3.1	2.85	2.85
B at z_0 (G)	0.02	0.02	0.02	0.02
Γ	30	30	30	30
R_B (cm)	1.5×10^{17}	1.5×10^{17}	1.5×10^{17}	1.5×10^{17}
θ_{obs} (°)	1.91	1.91	1.91	1.91
T_{BB} (K)	80	80	80	1
L_{disk} (erg s^{-1})	10^{41}	10^{41}	10^{41}	10^{41}
R_{torus} (cm)	10^{18}	10^{18}	10^{18}	10^{18}
τDT	0.05	0.05	0.05	0.03
L_k (erg s^{-1})	3.92×10^{43}	3.81×10^{43}	3.90×10^{43}	3.90×10^{43}
L_B (erg s^{-1})	3.04×10^{43}	3.04×10^{43}	3.04×10^{43}	3.04×10^{43}
L_B/L_k	0.77	0.80	0.78	0.78

Table 5.1: Parameters of SSC+EC models from the blazar SED tool for the multiwavelength SEDs corresponding to the highest, lowest, and time-averaged X-ray states.

5.2.1 Published model parameters

For the publication (Aliu et al., 2013), the SEDs were modelled using a purely leptonic SSC model (described in Acciari et al. (2009), which is a quasi-equilibrium version of the model of Böttcher & Chiang (2002)) with the addition of an external radiation field that is isotropic in the rest frame of the AGN (EC component). The parameters for this model were provided by Dr. Markus Böttcher. This is in accordance with the VERITAS publication policy, which requires that published model parameters be provided by an experienced theorist. A description of this model is given in Chapter 4.

A set of parameters is derived for each of the three X-ray states (high, low, and average), and it is found that the X-ray variability can be modeled by changing almost exclusively the electron injection spectral index, with minor adjustments of the kinetic luminosity in electrons. The models provide a reasonable representation of the data, but tend to underestimate the flux at a few hundred MeV.

The data and models are shown in Figure 5.11. The parameters of the models are shown in Table 5.2.

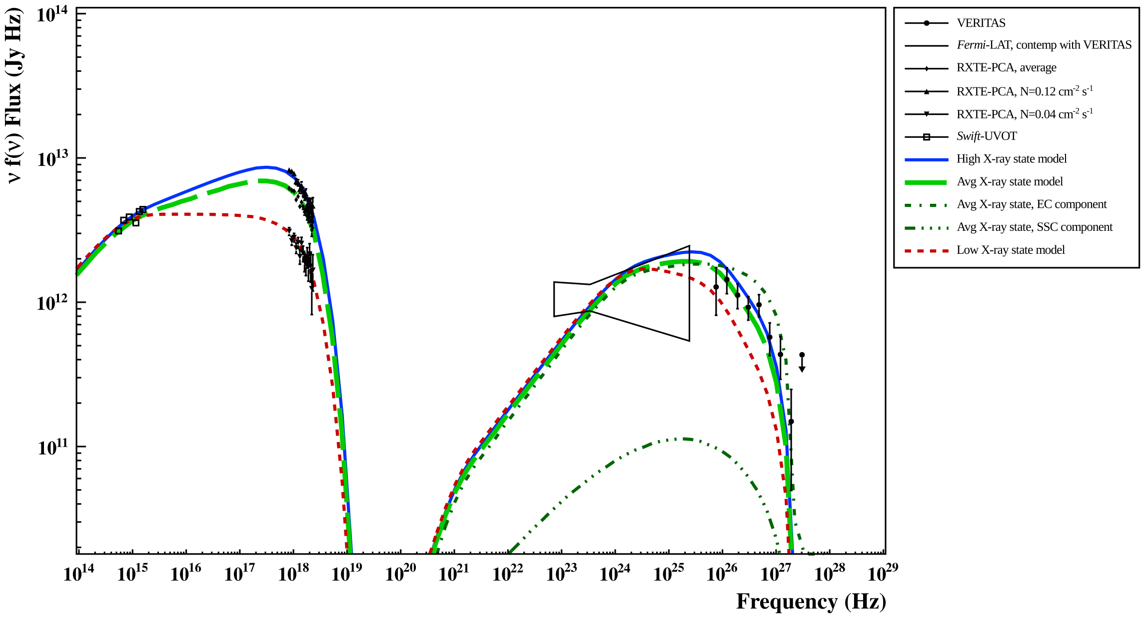

Figure 5.11: SEDs and published models of 1ES 1959+650 (Aliu et al., 2013). The solid (blue) line corresponds to the model for the highest X-ray normalisation, the dotted (red) line shows the model for the lowest X-ray normalisation, and the dashed (green) line represents the model for the time-averaged X-ray spectrum.

Parameter	High X-ray	Low X-ray	Avg. X-ray
$\gamma_{\text{Bot, min}}$	1.8×10^4	1.8×10^4	1.8×10^4
$\gamma_{\text{Bot, max}}$	9×10^5	9×10^5	9×10^5
q_{Bot}	1.7	2.0	1.75
η_{esc}	1000	1000	1000
B at z_0 (G)	0.02	0.02	0.02
Γ	30	30	30
R_B (cm)	1.5×10^{17}	1.5×10^{17}	1.5×10^{17}
θ_{obs} (°)	1.91	1.91	1.91
T_{BB} (K)	20	20	20
u_{ext} (erg cm^{-3})	3.5×10^{-10}	3.5×10^{-10}	3.5×10^{-10}
$\delta t_{\text{var,min}}$ (s)^a	1.74×10^5	1.74×10^5	1.74×10^5
L_e (erg s^{-1})	3.28×10^{43}	3.27×10^{43}	3.03×10^{43}
L_B (erg s^{-1})	3.04×10^{43}	3.04×10^{43}	3.04×10^{43}
L_B/L_e	0.93	0.93	1.0

Table 5.2: Parameters of SSC+EC models for the 3 multiwavelength SEDs corresponding to the highest, lowest, and time-averaged X-ray states.
[a] This parameter is consistent with the variability timescale of the RXTE observations reported in this chapter, though it was not directly constrained by these observations.

5.3 Discussion

The parameters for both sets of models are chosen to reproduce the significant X-ray variability recorded during simultaneous observations of low-flux and marginally variable γ-ray observations. In the models produced by the blazar SED tool, a scenario in which the kinetic luminosity dominates slightly over the magnetic field is favoured. The Böttcher models however, prefer a scenario in which the electrons and magnetic field are in equipartition. Almost all other models of this source (with the exception of Tavecchio et al. (2010), which is essentially in equipartition) present a system that is out of equipartition, with the electron energy density dominating over the magnetic field by several orders of magnitude.

Both cases presented here attempt to describe a scenario in which it is easy to generate de-coupled high-energy variability, such as the X-ray variability seen in this work, or the "orphan" γ-ray flare observed in 2002. This can be achieved if the X-rays are produced by the highest-energy electrons, but the VHE γ-rays are produced by significantly lower-energy electrons. In order to create this scenario where the very-high-energy electrons produce the X-rays, a low magnetic field and high Doppler factor is required, differing from the models presented in previous work, (e.g., Tagliaferri et al., 2008; Tavecchio et al., 2010). De-coupled X-ray flares can then be easily created by hardening the electron spectrum, or VHE flares produced by injecting additional electrons at lower energies.

Such modelling efforts are not entirely unprecedented: other examples of blazars which exhibit uncorrelated X-ray and γ-ray fluxes exist. In particular, a multiwavelength study of PKS 2155-304 (Aharonian et al., 2009) did not find any evidence of a flux correlation between X-ray and VHE fluxes. This source was also modelled using a one-zone SSC model and assuming that the electrons responsible for the synchrotron emission in the X-ray band have higher energies than the electrons that produce the inverse-Compton emission in the VHE range. PG 1553+113 has also been found to have relatively stable VHE emission, with clear variability in X-rays. Abdo et al. (2010a) modelled that behaviour with a single-zone SSC model, changing only the electron distribution to produce the different X-ray states. Aleksić et al. (2012) modelled only the average of the low-energy bump in conjunction with the γ-ray data, also using a one-zone SSC model.

It is of note that the X-ray to optical flux ratio observed in 1ES 1959+650 in this case is lower than has been reported previously in the literature. A substantial break is therefore needed around optical wavelengths in order to connect to the X-rays, whereas the other SEDs are consistent with a smooth continuum through the optical-UV to X-rays. As a result, a steeper electron spectrum is required here than is presented in other works.

Initially it appears the that the electron injection spectral indices disagree between the blazar SED tool models and Böttcher models. However, the electrons are in the fast cooling regime in the Böttcher models, which means that the particle distribution between $\gamma_{\text{Bot, min}}$ and $\gamma_{\text{Bot, max}}$

is described by $n(\gamma) \propto \gamma^{-(q_{\text{Bot}}+1)}$. In the blazar SED tool, the particles are described by $n(\gamma) \propto \gamma^{-(q_T)}$. Therefore, the comparison is in fact between q_T and $q_{\text{Bot}}+1$, and these values are very similar for a given X-ray state in the two sets of models.

The very hard electron injection spectral indices ($1.7 \leq q_{\text{Bot}} \leq 2.0$; $1.8 \leq q_T - 1 \leq 2.1$) pose challenges to standard models of ultrarelativistic Fermi acceleration at parallel shocks. These models can produce indices in the range $2.2 \lesssim q \lesssim 2.3$ (Achterberg et al., 2001). This may indicate the presence of other processes such as acceleration at oblique subluminal shocks which are capable of producing hard electron indices in the presence of large-angle scattering (Summerlin & Baring, 2012), stochastic acceleration (second-order Fermi acceleration) (Virtanen & Vainio, 2005), or particle acceleration at shear boundary layers in the case of an inhomogeneous jet with a fast inner spine and slow outer cocoon (Ostrowski, 2000; Stawarz & Ostrowski, 2002; Rieger & Duffy, 2004).

These observations show that 1ES 1959+650 can be reasonably described by a leptonic SSC + EC model in a low VHE flux state. However, it is clear that this type of model cannot account for the total flux observed in the IC peak. It can be made to represent the observed MeV-GeV flux, or the observed VHE flux, but cannot create the emission seen in both simultaneously. This indicates that this type of model is not sufficient to describe observed emission from this source. Also, the fact that the same SED may be fit equally well with models that are in equipartition, and out of equipartition, indicates that these models are not particularly well-constrained as they stand.

It seems likely that a single-zone leptonic SSC + EC model is too simplistic to describe the data. It is true that the addition of a hadronic component may improve the models' representation of the IC peak, but including an extra independent high-energy component is not very meaningful, since that component would be essentially unconstrained. In fact, Backes et al. (2012) found that even lepto-hadronic modelling could not reproduce the entire high-energy bump, and only a model comprising two independent SSC emission zones could provide a reasonable description of the SED.

In any case, neglecting these concerns and accepting the current models, the parameters obtained cannot be fully explained by first-order Fermi acceleration at parallel shocks, and instead may suggest particle acceleration at oblique subluminal shocks, or that 1ES 1959+650 may consist of an inhomogeneous jet with a fast inner spine and slower-moving outer cocoon.

On May 20, 2012, VERITAS observed a rapid VHE flare from 1ES 1959+650. VERITAS was observing this source almost nightly at the time due to a highly elevated optical state. The VHE flux rose to $\sim 120\%$ of the Crab Nebula flux without an increase in the X-ray emission. These observations are to be presented in Aliu et al. (prep).

5.4 Bibliography

Abdo, A. A., Ackermann, M., Ajello, M., et al., 2010a; 'FERMI OBSERVATIONS OF THE VERY HARD GAMMA-RAY BLAZAR PG 1553+113'. *The Astrophysical Journal*, vol. 708(2):1310

—, 2010b; 'SPECTRAL PROPERTIES OF BRIGHT FERMI -DETECTED BLAZARS IN THE GAMMA-RAY BAND'. *The Astrophysical Journal*, vol. 710(2):1271

Acciari, V. A., Aliu, E., Aune, T., et al., 2009; 'Multiwavelength Observations of a TeV-Flare from W Comae'. *The Astrophysical Journal*, vol. 707(1):612

Achterberg, A., Gallant, Y. A., Kirk, J. G., et al., 2001; 'Particle acceleration by ultra-relativistic shocks: theory and simulations'. *Monthly Notices of the Royal Astronomical Society*, vol. 328(2):393

Aharonian, F., Akhperjanian, A. G., Anton, G., et al., 2009; 'SIMULTANEOUS OBSERVATIONS OF PKS 2155304 WITH HESS, FERMI , RXTE , AND ATOM: SPECTRAL ENERGY DISTRIBUTIONS AND VARIABILITY IN A LOW STATE'. *The Astrophysical Journal*, vol. 696(2):L150

Aharonian, F. A., Akhperjanian, A., Barrio, J. A., et al., 2001; 'Evidence for TeV gamma ray emission from Cassiopeia A'. *Astronomy and Astrophysics*, vol. 370:112

Ajello, M., Costamante, L., Sambruna, R. M., et al., 2009; 'THE EVOLUTION OF SWIFT /BAT BLAZARS AND THE ORIGIN OF THE MeV BACKGROUND'. *The Astrophysical Journal*, vol. 699(1):603

Aleksić, J., Alvarez, E. A., Antonelli, L. A., et al., 2012; 'PG 1553+113: FIVE YEARS OF OBSERVATIONS WITH MAGIC'. *The Astrophysical Journal*, vol. 748(1):46

Aliu, E., Archambault, S., Arlen, T., et al., 2013; 'Multiwavelength Observations and Modeling of 1ES 1959+650 in a Low Flux State'. *The Astrophysical Journal*, vol. 775:3

Aliu, E., et al., in prep;

Backes, M., Uellenbeck, M., Hayashida, M., et al., 2012; ‘Long-term spectral and temporal behavior of the high-frequency peaked BL LAC object 1ES 1959+650’. In ‘HIGH ENERGY GAMMA-RAY ASTRONOMY: 5th International Meeting on High Energy Gamma-Ray Astronomy. AIP Conference Proceedings’, vol. 1505, 522–525. Heidelberg, Germany

Beckmann, V., Soldi, S., Ricci, C., et al., 2009; ‘The second INTEGRAL AGN catalogue’. *Astronomy and Astrophysics*, vol. 505(1):417

Berge, D., Funk, S., Hinton, J., 2007; ‘Background modelling in very-high-energy $\{\gamma\}$-ray astronomy’. *Astronomy and Astrophysics*, vol. 466:1219

Bottacini, E., Böttcher, M., Schady, P., et al., 2010; ‘PROBING THE TRANSITION BETWEEN THE SYNCHROTRON AND INVERSE-COMPTON SPECTRAL COMPONENTS OF 1ES 1959+650’. *The Astrophysical Journal Letters*, vol. 719(2):L162

Böttcher, M., 2005; ‘A Hadronic Synchrotron Mirror Model for the "Orphan" TeV Flare in 1ES 1959+650’. *The Astrophysical Journal*, vol. 621(1):176

Böttcher, M., Chiang, J., 2002; ‘X-Ray Spectral Variability Signatures of Flares in BL Lacertae Objects’. *The Astrophysical Journal*, vol. 581(1):127

Cusumano, G., La Parola, V., Segreto, A., et al., 2010; ‘The Palermo Swift -BAT hard X-ray catalogue’. *Astronomy & Astrophysics*, vol. 524:A64

Daniel, M. K., Badran, H. M., Bond, I. H., et al., 2005; ‘Spectrum of Very High Energy Gamma-Rays from the blazar 1ES 1959+650 during Flaring Activity in 2002’. *The Astrophysical Journal*, vol. 621(1):181

Donato, D., Sambruna, R. M., Gliozzi, M., 2005; ‘Six years of BeppoSAX observations of blazars: A spectral catalog’. *Astronomy and Astrophysics*, vol. 433(3):1163

Fumagalli, M., Dessauges-Zavadsky, M., Furniss, A., et al., 2012; ‘A search of CO emission lines in blazars: the low molecular gas content of BL Lac objects compared to quasars’. *Monthly Notices of the Royal Astronomical Society*, vol. 424(3):2276

Giebels, B., Bloom, E. D., Focke, W., et al., 2002; ‘Observation of XRay Variability in the BL Lacertae Object 1ES 1959+65’. *The Astrophysical Journal*, vol. 571(2):763

Holder, J., Bond, I. H., Boyle, P. J., et al., 2003; ‘Detection of TeV Gamma Rays from the BL Lacertae Object 1ES 1959+650 with the Whipple 10 Meter Telescope’. *The Astrophysical Journal Letters*, vol. 583(1):L9

Kalberla, P. M. W., Burton, W. B., Hartmann, D., et al., 2005; 'The Leiden/Argentine/Bonn (LAB) Survey of Galactic HI. Final data release of the combined LDS and IAR surveys with improved stray-radiation corrections'. *Astronomy and Astrophysics*, vol. 440:775

Konopelko, A., Hemberger, M., Aharonian, F. A., et al., 1999; 'Performance of the stereoscopic system of the HEGRA imaging air Čerenkov telescopes: Monte Carlo simulations and observations'. *Astroparticle Physics*, vol. 10:275

Krawczynski, H., Hughes, S. B., Horan, D., et al., 2004; 'Multiwavelength Observations of Strong Flares from the TeV Blazar 1ES 1959+650'. *The Astrophysical Journal*, vol. 601(1):151

Lindberg, V., 2000; 'Uncertainties and Error Propagation'

Maselli, A., Cusumano, G., Massaro, E., et al., 2010; 'The blazar content in the Swift -BAT hard X-ray sky'. *Astronomy and Astrophysics*, vol. 520:A47

Massaro, E., Giommi, P., Leto, C., et al., 2009; 'Roma-BZCAT: a multifrequency catalogue of blazars'. *Astronomy and Astrophysics*, vol. 495(2):691

Massaro, E., Tramacere, A., Perri, M., et al., 2006; 'Log-parabolic spectra and particle acceleration in blazars'. *Astronomy and Astrophysics*, vol. 448(3):861

Nishiyama, T., 1999; 'Detection of a new TeV gamma-ray source of BL Lac object 1ES 1959+650'. In 'Proceedings of the 26th International Cosmic Ray Conference', , (eds. Dingus, B. L., Kieda, D. B., Salamon, M. H.), vol. 3 of *International Cosmic Ray Conference*, 370. Salt Lake City, USA

Nolan, P. L., Abdo, A. A., Ackermann, M., et al., 2012; 'Fermi Large Area Telescope Second Source Catalog'. *The Astrophysical Journal Supplement Series*, vol. 199(2):31

Ostrowski, M., 2000; 'On possible 'cosmic ray cocoons' of relativistic jets'. *Monthly Notices of the Royal Astronomical Society*, vol. 312(3):579

Resconi, E., Franco, D., Gross, A., et al., 2009; 'The classification of flaring states of blazars'. *Astronomy and Astrophysics*, vol. 502(2):499

Rieger, F. M., Duffy, P., 2004; 'Shear Acceleration in Relativistic Astrophysical Jets'. *The Astrophysical Journal*, vol. 617(1):155

RXTE Guest Observer Facility, 2006; 'Reduction and Analysis of PCA Binned-Mode Data'. http://heasarc.nasa.gov/docs/xte/recipes/pca_spectra.html

Schachter, J. F., Stocke, J. T., Perlman, E., et al., 1993; 'Ten new BL Lacertae objects discovered by an efficient X-ray/radio/optical technique'. *The Astrophysical Journal*, vol. 412:541

Sokolov, A., Marscher, A. P., McHardy, I. M., 2004; 'Synchrotron Self-Compton Model for Rapid Nonthermal Flares in Blazars with Frequency-dependent Time Lags'. *The Astrophysical Journal*, vol. 613(2):725

Stawarz, L., Ostrowski, M., 2002; 'Radiation from the Relativistic Jet: A Role of the Shear Boundary Layer'. *The Astrophysical Journal*, vol. 578(2):763

Summerlin, E. J., Baring, M. G., 2012; 'Diffusive Acceleration of Particles at Oblique, Relativistic, Magnetohydrodynamic Shocks'. *The Astrophysical Journal*, vol. 745(1):63

Tagliaferri, G., Foschini, L., Ghisellini, G., et al., 2008; 'Simultaneous Multiwavelength Observations of the Blazar 1ES 1959+650 at a Low TeV Flux'. *The Astrophysical Journal*, vol. 679(2):1029

Tavecchio, F., Ghisellini, G., Ghirlanda, G., et al., 2010; 'TeV BL Lac objects at the dawn of the Fermi era'. *Monthly Notices of the Royal Astronomical Society*, vol. 401(3):1570

Tramacere, A., Giommi, P., Perri, M., et al., 2009; 'Swift observations of the very intense flaring activity of Mrk421 during 2006. I. Phenomenological picture of electron acceleration and predictions for MeV/GeV emission'. *Astronomy and Astrophysics*, vol. 501(3):879

Tramacere, A., Massaro, E., Taylor, A. M., 2011; 'STOCHASTIC ACCELERATION AND THE EVOLUTION OF SPECTRAL DISTRIBUTIONS IN SYNCHRO-SELF-COMPTON SOURCES: A SELF-CONSISTENT MODELING OF BLAZARS FLARES'. *The Astrophysical Journal*, vol. 739(2):66

Tueller, J., Baumgartner, W. H., Markwardt, C. B., et al., 2010; 'THE 22 MONTH SWIFT -BAT ALL-SKY HARD X-RAY SURVEY'. *The Astrophysical Journal Supplement Series*, vol. 186(2):378

Verrecchia, F., in 't Zand, J. J. M., Giommi, P., et al., 2007; 'The Beppo SAX WFC X-ray source catalogue'. *Astronomy and Astrophysics*, vol. 472(2):705

Virtanen, J. J. P., Vainio, R., 2005; 'Stochastic Acceleration in Relativistic Parallel Shocks'. *The Astrophysical Journal*, vol. 621(1):313

Winter, L. M., Mushotzky, R. F., Reynolds, C. S., et al., 2009; 'X-RAY SPECTRAL PROPERTIES OF THE BAT AGN SAMPLE'. *The Astrophysical Journal*, vol. 690(2):1322

CHAPTER

6

The search for variability in the VHE emission of the Crab Nebula during the March 2013 MeV flare

The Crab Nebula is one of the best-studied cosmic particle accelerators. Its distance of ~ 2 kpc and absolute luminosity of 5×10^{38} erg s^{-1} allow the study of the nebula in great detail across the entire electromagnetic spectrum. From the earliest days of X-ray astronomy, the Crab Nebula was considered sufficiently steady and bright for use as a "standard candle" calibration source (Toor & Seward, 1974; Kirsch et al., 2005). Once detected in the VHE regime, it was immediately adopted as a TeV standard candle also (Weekes et al., 1989).

There may have been hints even around the time that it was proposed as an X-ray calibration source that the Crab Nebula was not a truly stable emitter (McBreen et al., 1973; Greisen et al., 1975). However, it was not until 2011 that the nebula's variability was clearly observed and quantified. Wilson-Hodge et al. (2011) reported a decline of $\sim 7\%$ in the Crab Nebula flux in the 15 – 50 keV band since 2008. This effect was observed by *Fermi*-GBM and independently confirmed by *Swift*-BAT, RXTE-PCA and INTEGRAL-IBIS. A similar decline was also seen in the ~ 3 – 15 keV band with RXTE-PCA, and in the 50 – 100 keV band with *Fermi*-GBM, *Swift*-BAT and INTEGRAL-IBIS. In the same month, Tavani et al. (2011) reported the detection of strong γ-ray flares in the range 0.1 – 5 GeV with AGILE in October 2007 and September 2010. This was corroborated by Abdo et al. (2011), who reported > 100 MeV flares detected by *Fermi*-LAT in February 2009 and September 2010, the latter being the same flare as seen by AGILE. The discovery of variability in the Crab Nebula on any timescale was completely unexpected. Even more surprising was the extremity of the short-term flares - the Crab Nebula flux was seen to increase by more than a factor of ten in less than a day in the 100 MeV − 1 GeV range in the most dramatic case.

Multiwavelength campaigns have been executed every time a flare has been observed since the detection of the September 2010 flare (Tavani et al., 2011). Simultaneous coverage at high energies during these campaigns have not yet revealed any correlated activity (Balbo et al., 2011; Striani et al., 2011, 2013; Buehler et al., 2012). While multiwavelength coverage has been excellent in radio, optical, and X-rays, it has been rather sparse at energies above 100 GeV, i.e., in the inverse-Compton component.

Both MAGIC and VERITAS reported TeV emission consistent with previous observations (i.e., no enhancement or change in spectral shape) during the flare in September 2010 (Mariotti, 2010; Ong, 2010). ARGO-YBJ, however, reported a flux about 3-4 times higher than the average emission at a median energy of about 1 TeV, based on a preliminary analysis of their data (Vernetto, 2010). More recently, ARGO-YBJ data from the last five years has been reanalysed to study the variability of the Crab Nebula in the 0.5 − 20 TeV energy range. The long-term light curve is consistent with a uniform flux with a probability of 0.11 (Vernetto, 2013). However, a very tenuous correlation with the corresponding *Fermi*-LAT light curve is also reported, implying (in the case that it is a real effect) the same behaviour of the gamma-ray emission at energies ~ 100 MeV and ~ 1 TeV. The light curve and correlation plot are shown in Figure 6.1.

In March 2013, *Fermi*-LAT detected a flare from the Crab Nebula lasting ~ 2 weeks (Ojha et al., 2013; Mayer et al., 2013). During this period, a 20-fold increase above the average synchrotron flux > 100 MeV was observed. VERITAS observed the Crab Nebula for ten nights during the flare from March 02, 2013 to March 15, 2013 (MJD $56353 - 56366$). This chapter reports on the VERITAS observations of the Crab Nebula during this recent flare. The material presented in this chapter is also published in Aliu et al. (2014), (arXiv:1309.5949).

6.1 VERITAS observations of the March 2013 flare

In the seasons since the discovery of flaring episodes from the Crab Nebula, a ToO programme (of which the author is PI) has been in place for VERITAS to observe the source in the event that another flare is observed by other instruments. On March 02, 2013, two days prior to the Astronomer's Telegram from the *Fermi*-LAT collaboration announcing the gamma-ray flare (Ojha

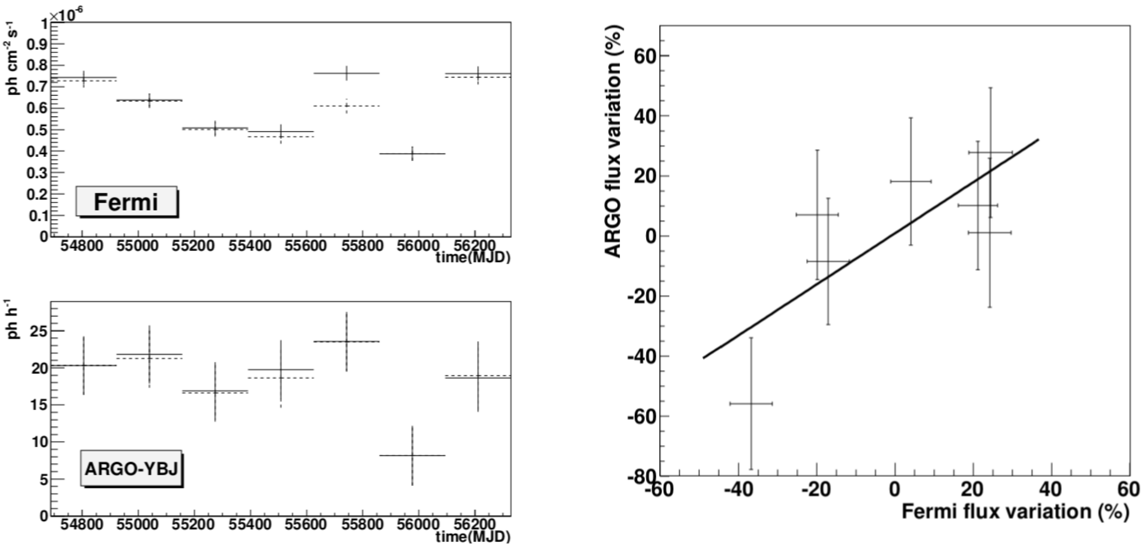

Figure 6.1: ARGO-YBJ observations of the Crab Nebula. The lower left panel shows the light curve of the Crab Nebula measured by ARGO-YBJ, and the upper left panel shows the *Fermi*-LAT light curve in bins matching the lower panel. The ARGO-YBJ light curve is consistent with a constant flux with a probability of 0.11. The dashed lines in both light curves are obtained by excluding days with flares. The right panel shows the correlation plot of the percent variation of the Crab Nebula flux with respect to the average value. Figures are taken from Vernetto (2013).

et al., 2013), this programme was triggered by an automated *Fermi*-LAT analysis pipeline at Barnard College, Columbia University (Errando & Orr, 2011).

Observations of the Crab Nebula began that night. The VERITAS flare data set is composed of ten nights of observations during the flare period spanning March 02, 2013 to March 15, 2013 (MJD $56353 - 56366$). Observations of the Crab Nebula as part of the standard observing schedule from October 13, 2012 to April 02, 2013 excluding the flare period, constitute a baseline data set on the source in its non-flaring state with which to compare the flare data.

The data were taken in wobble mode with an offset of $0\overset{\circ}{.}5$ from the source position alternately in each of the four cardinal directions (Aharonian et al., 2001; Berge et al., 2007). Observations were conducted using the full four-telescope array in a range of zenith angles $12^\circ - 55^\circ$, giving a total of 10.3 hours of live time on the source during the flare and 17.4 hours during the rest of the season. Two nights of flare observations were conducted at large zenith angles, increasing the energy threshold up to ~ 750 GeV for the largest zenith angles, from the ~ 100 GeV threshold achievable at higher elevations. The low-energy threshold is set to a common value of 1 TeV in the analysis to overcome the changing threshold, except where stated otherwise.

In this analysis, images composed of fewer than five pixels are rejected. For each image, mean

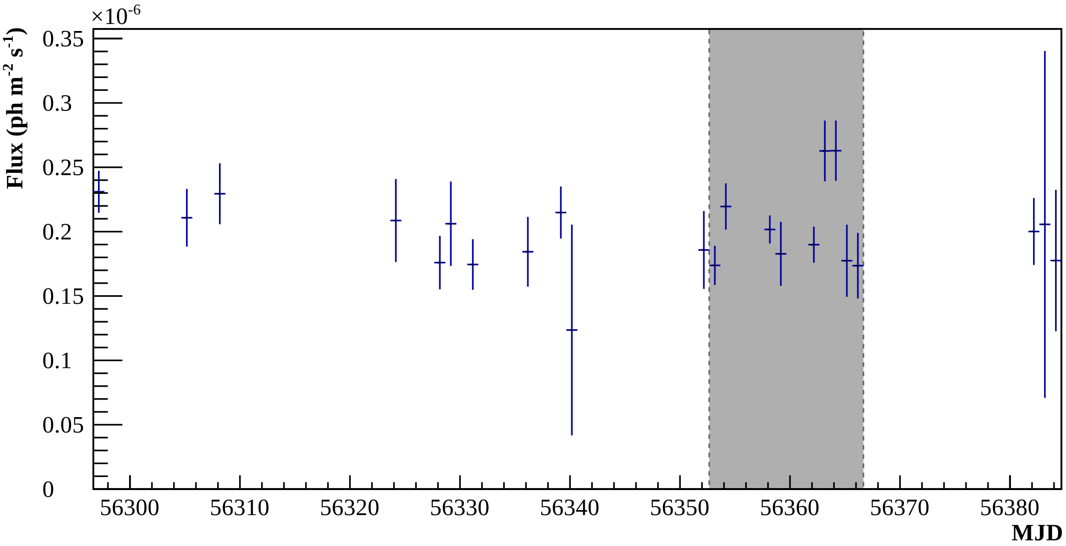

Figure 6.2: VERITAS light curve of the Crab Nebula > 1 TeV in nightly bins. The shaded region corresponds to the flare period, and the unshaded areas correspond to the baseline measurements.

scaled width and mean scaled length parameters are required to be in the range 0 − 1.15 and 0 − 1.4 respectively. No cut is made on the height of the maximum Cherenkov emission from the reconstructed shower. A circular region of radius 0°.16 centered on the source coordinates is defined from which γ-ray like events are selected. Overall, these constitute a looser set of cuts than those normally applied. The looser cuts are used in this case to maximise the possibility of detecting any changes in the source emission in small periods of time.

A nightly light curve is produced for energies > 1 TeV for the flare and baseline data sets, and is shown in Figure 6.2. The flare and baseline periods are first tested independently for variability by fitting the respective light curves with a constant flux. For the flare period, this fit produces a flux > 1 TeV of $(2.05 \pm 0.07) \times 10^{-11}$ photons cm^{-2} s^{-1} with $\chi^2/NDF = 2.12$ and a fit probability of ~ 0.02. The fit to the baseline period yields a flux > 1 TeV of $(2.10 \pm 0.06) \times 10^{-11}$ photons cm^{-2} s^{-1} with $\chi^2/NDF = 0.99$ and a fit probability of ~ 0.48. A constant flux is also fit to the entire light curve (flare plus baseline periods), yielding parameters that are consistent with both previous fits with a flux > 1 TeV of $(2.02 \pm 0.04) \times 10^{-11}$ photons cm^{-2} s^{-1} with $\chi^2/NDF = 1.44$ and a fit probability of ~ 0.08.

Energy spectra are calculated above 1 TeV for the baseline and flare Crab Nebula observations, and are shown together in Figure 6.3. The spectra are parameterised as power laws of the form of Equation 5.1.1. The baseline spectral fit gives a normalisation of $N_0^{\mathrm{baseline}} = (3.48 \pm 0.14_{\mathrm{stat.}} \pm 1.08_{\mathrm{sys.}}) \times 10^{-11}$ cm^{-2} s^{-1} TeV^{-1} and $\gamma^{\mathrm{baseline}} = 2.65 \pm 0.04_{\mathrm{stat.}} \pm 0.3_{\mathrm{sys.}}$, with $\chi^2/NDF = 1.38$. The spectral fit to the flare observations yields a normalisation of $N_0^{\mathrm{flare}} = (3.53 \pm 0.15_{\mathrm{stat.}} \pm$

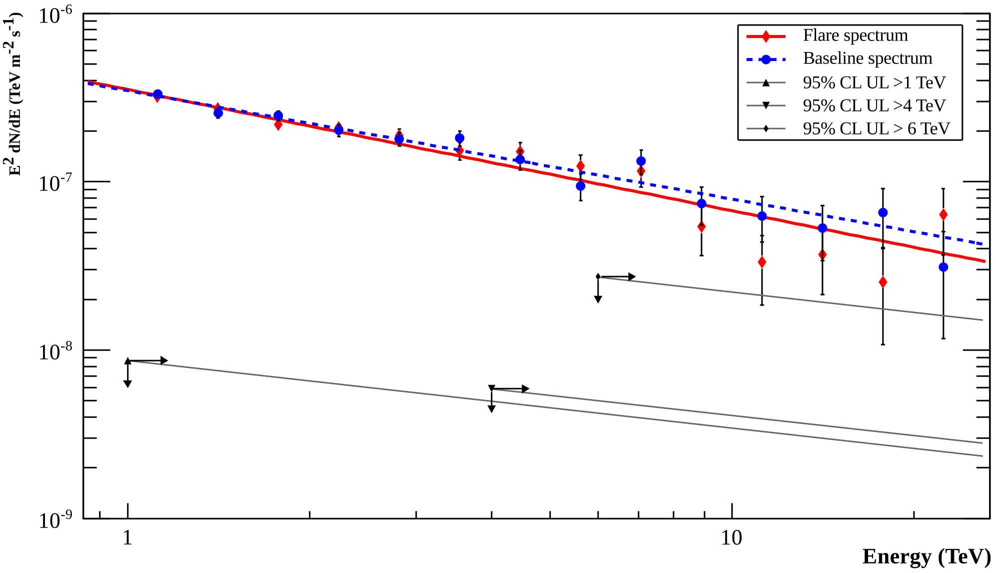

Figure 6.3: VERITAS spectra of the Crab Nebula showing the flare data set in red, and the baseline data set in blue. The spectra are fit with power law functions of the form $\frac{dN}{dE} = N_0 \left(\frac{E}{1\,\mathrm{TeV}}\right)^{\gamma}$. These spectral parameters are mutually consistent, implying no change in the TeV flux or spectral shape during the flare. Also shown here are the upper limits on an extra flux component in the flare, computed assuming a spectral index of -2.4 in Section 6.2.

$1.12_{\mathrm{sys.}}) \times 10^{-11}$ cm^{-2} s^{-1} TeV^{-1} and an index of $\gamma^{\mathrm{flare}} = 2.72 \pm 0.05_{\mathrm{stat.}} \pm 0.3_{\mathrm{sys.}}$, with $\chi^2/NDF = 0.84$.

The average flux during the flare is consistent with the average baseline flux. The spectral parameters of the flare and baseline data sets are also consistent. Therefore, no change in the TeV flux or spectral shape occurred during the period of the GeV flare.

A similar analysis is performed on the subset of the data with information below 1 TeV. This smaller data set is analysed separately with a low-energy threshold of 150 GeV. Fitting the baseline light curve with a constant flux gives a mean flux value > 150 GeV of $(3.32 \pm 0.04) \times 10^{-10}$ photons cm^{-2} s^{-1} with $\chi^2/NDF = 1.75$ and a fit probability of ~ 0.05. A constant flux fit to the flare light curve yields a consistent mean flux > 150 GeV of $(3.36 \pm 0.06) \times 10^{-10}$ photons cm^{-2} s^{-1} with $\chi^2/NDF = 0.72$ and a fit probability of ~ 0.61. In accordance with the results above 1 TeV, no spectral or temporal variability is revealed at these energies. A light curve of the flare period from this analysis can be seen in Figure 6.5.

6.2 Upper limits on the average VHE flux change during the flare

Tests for variability in the VERITAS data set revealed a Crab Nebula flux that is stable during the flare period, and furthermore, is consistent with the baseline flux measured while the source is not flaring. In comparison, the *Fermi*-LAT observed the synchrotron nebula at ~ 20 times the average baseline flux at the peak of the GeV flare. The VERITAS light curves > 1 TeV and < 1 TeV are shown alongside the *Fermi*-LAT light curve for the same period in Figure 6.5.

Figure 6.4 shows the VERITAS baseline and flare spectra in comparison to the *Fermi*-LAT time-averaged spectrum and flare spectra. The full energy range of *Fermi*-LAT extends into the IC bump of the Crab Nebula. However, statistics are limited at these higher energies and in order to probe this region, long integration times are required. Consequently, on the time scales of the flares, the energy range of *Fermi*-LAT is effectively truncated. As a result, there is no information on what changes, if any, occur in the early part of the IC bump in these flaring states. The lower energies, in contrast, exhibit an additional component in the SED between 100 MeV and 1 GeV during the flare.

To fully discern the VHE behaviour of the source during the GeV flare, a relative flux change during the flare is calculated for the VERITAS data as

$$\Delta F^i_{\mathrm{rel.}} = \frac{F^i - \overline{F}}{\overline{F}}, \tag{6.2.1}$$

where F^i is the average flux for a night or group of nights, and $\overline{F}$ is the average baseline flux from the nebula. The average relative flux change over the flare in VERITAS above 1 TeV is $\Delta \overline{F_{\mathrm{rel.}}} = -0.026 \pm 0.035$.

From $\Delta \overline{F_{\mathrm{rel.}}}$, a 95% confidence level upper limit (UL) is computed for an elevated VHE flux. A Bayesian prior is introduced that is zero for negative relative flux changes and one elsewhere. This assumes some positive correlation of the *Fermi*-LAT and VERITAS fluxes during the flare, imposing the constraint that the VHE flux change is positive, or at least zero. The upper limit is calculated over the Bayesian interval $[0, x^{\mathrm{up}}]$ such that

$$\frac{\int\limits_0^{x^{\mathrm{up}}} \exp\left(-\frac{(\Delta\overline{F_{\mathrm{rel}}}-x)^2}{2\sigma^2}\right) dx}{\int\limits_0^{\infty} \exp\left(-\frac{(\Delta\overline{F_{\mathrm{rel}}}-x')^2}{2\sigma^2}\right) dx'} = 0.95 \quad (x^{\mathrm{up}} > 0) \tag{6.2.2}$$

where σ is the error on $\overline{\Delta F_{\mathrm{rel.}}}$, and the 95% CL upper limit is given by x^{up}, which is obtained by solving the equation numerically. Limits are calculated for three different energy thresholds

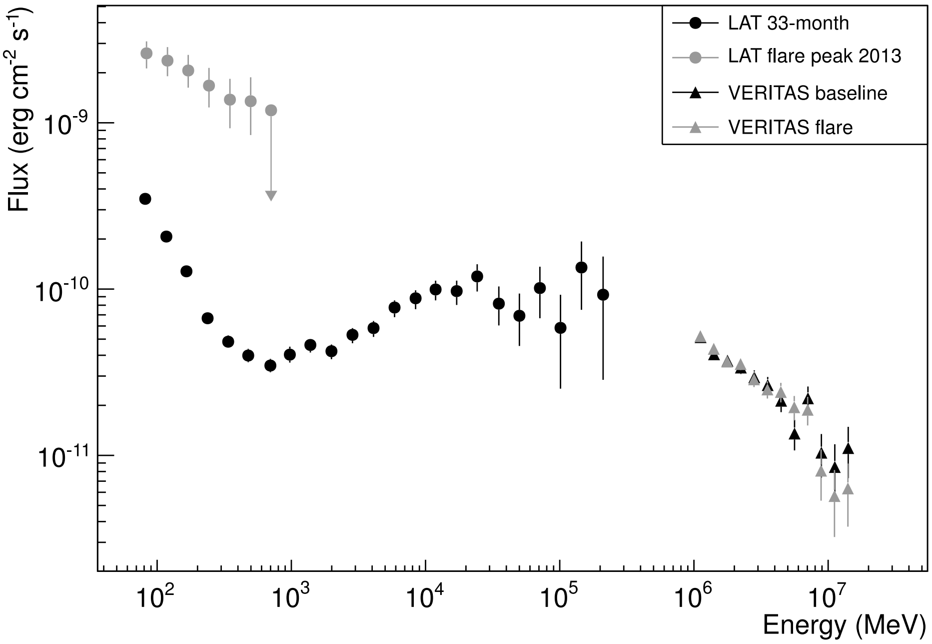

Figure 6.4: VERITAS spectra of the Crab Nebula in comparison to *Fermi*-LAT. The black circles show the *Fermi*-LAT spectrum of the Crab Nebula averaged over the first 33 months of observations (data from Buehler et al. (2012)). In this time, the nebula is observed from the high-energy part of the synchrotron bump to around the peak of the IC bump. The grey circles show the *Fermi*-LAT spectrum from the peak of the flare in March 2013 (data from Mayer et al. (2013)). During the flare, *Fermi*-LAT does not achieve significant detections of the nebula above ~ 1 GeV, and only unconstraining upper limits are available on the rising part of the IC bump. In comparison, the VERITAS spectra for the baseline state (black triangles) and flare state (grey triangles) are compatible.

shown in Table 6.1. These integral upper limits are converted to differential upper limits using the form of $\frac{dN}{dE}$ given in Equation 5.1.1. The integral upper limit is used as dN, the spectral range under consideration for each limit is used as dE, the canonical VHE Crab Nebula index of -2.4 is used as γ, and the energy for which the value of the power law is equal to its average value in the range under consideration for each limit is used as E. The differential representation of the upper limits are also shown in the context of the flare and baseline spectra in Figure 6.3.

Energy band (TeV)	$\overline{\Delta F^{\mathrm{VTS}}_{\mathrm{rel.}}}$ 95% CL UL	95% CL differential UL at threshold (TeV m^{-2} s^{-1})
> 1	5.3%	8.7×10^{-9}
> 4	6.8%	5.9×10^{-9}
> 6	37.4%	2.7×10^{-8}

Table 6.1: 95% CL Bayesian upper limits on the VHE relative flux increase during the flare period for three energy thresholds.

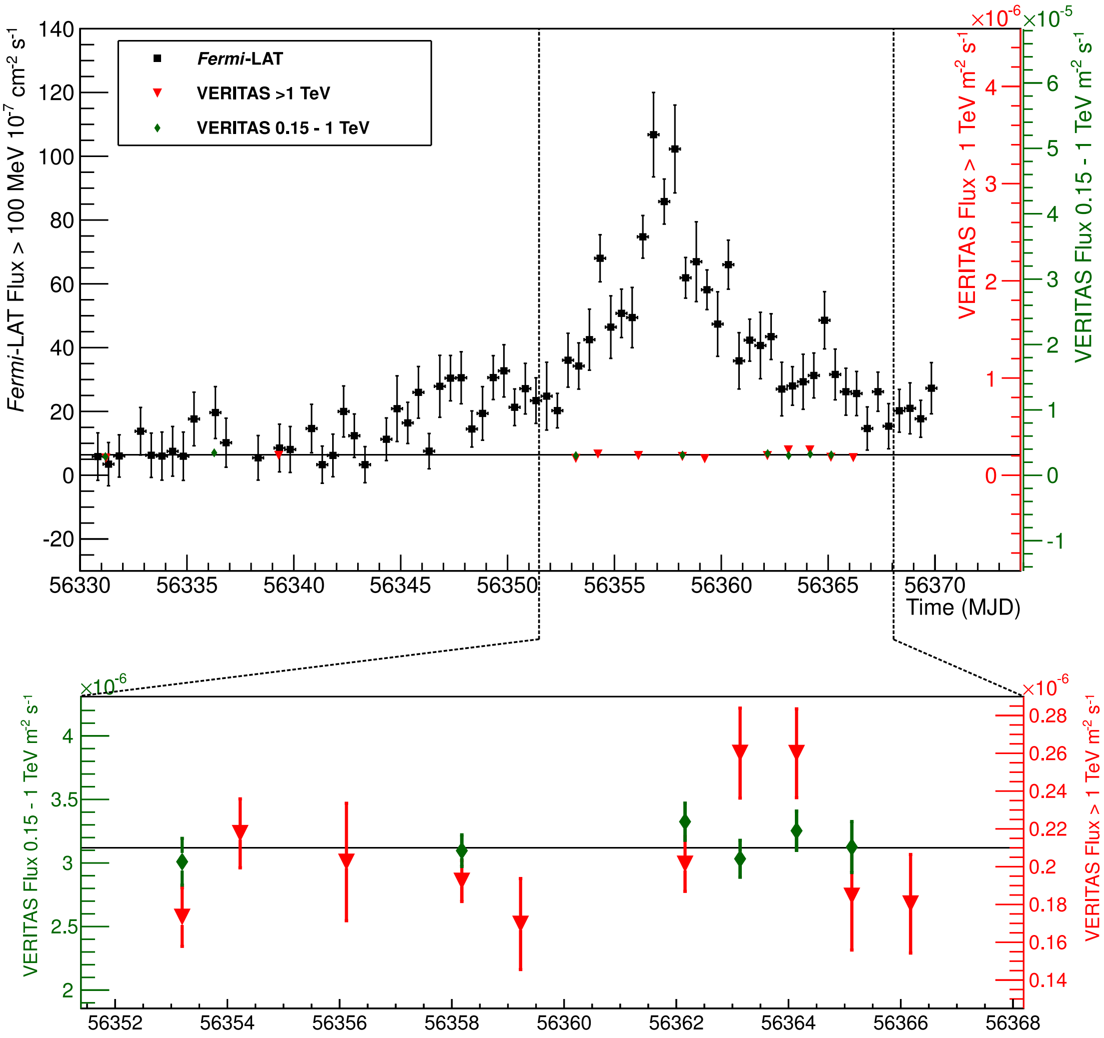

Figure 6.5: VERITAS light curves > 1 TeV and < 1 TeV for the Crab Nebula flare period in nightly bins. Shown for comparison is the *Fermi*-LAT light curve for the same period in 12-hour bins. The baseline Crab Nebula synchrotron flux above 100 MeV as measured by *Fermi*-LAT, and the the average VHE fluxes above 150 GeV and 1 TeV are aligned, and are indicated by the solid black line. The vertical scales of the three light curves have been adjusted such that the zero points and baseline fluxes are coincident.

6.3 Discussion

The VERITAS light curves and reconstructed energy spectrum do not indicate any flux enhancement at TeV energies, while the > 100 MeV synchrotron flux as measured by *Fermi*-LAT was six times the average during these VERITAS observations. At the peak of the flare, the synchrotron flux > 100 MeV reached a maximum of ~ 20 times the average flux at these energies. However, VERITAS could not observe on the night of the peak emission due to poor weather conditions.

Other VHE observations of the flare

The H.E.S.S. array of Cherenkov telescopes also observed the Crab Nebula for four consecutive nights during the flare, from March 6 to March 10 (Abramowski et al., 2013). In agreement with VERITAS, H.E.S.S. observed no significant changes in the VHE flux in this time. The H.E.S.S. measurements of the Crab Nebula spectrum above 1 TeV during the flare yield a spectral shape consistent with that measured by VERITAS. H.E.S.S. report a power law spectrum with a normalisation $N_0^{\mathrm{H,\,flare}} = (3.8 \pm 0.2) \times 10^{-11}$ cm^{-2} s^{-1} TeV^{-1} and an index of $\gamma^{\mathrm{H,\,flare}} = 2.7 \pm 0.1$, which compares well to the VERITAS measurement of a power law with $N_0^{\mathrm{V,\,flare}} = (3.53 \pm 0.15) \times 10^{-11}$ cm^{-2} s^{-1} TeV^{-1} and an index of $\gamma^{\mathrm{flare}} = 2.72 \pm 0.05$.

The first night of H.E.S.S. observations of the flaring nebula is coincident with the highest flux level detected by *Fermi*-LAT during the flare. Abramowski et al. (2013) use the H.E.S.S. observations of the Crab Nebula from that night to calculate upper limits on an enhancement of the integral fluxes above 1 TeV and 5 TeV by comparison to the integral flux of the spectrum published in Aharonian et al. (2006). With this method, the variation on the integral flux above 1 TeV as measured by H.E.S.S. is limited to less than 63%, and the integral flux above 5 TeV is limited to less than 78% at a 95% confidence level. These limits are far less constraining than those derived from the VERITAS observations in this chapter.

Model constraints from the VERITAS observations

The following constraint on the number of extra electrons in the flare with the necessary γ factor to create TeV photons, and the subsequent constraint on the spectral index of this population were derived for the publication in cooperation with collaborators.

Earlier flares had very hard spectra with peak energy reaching up to ~ 400 MeV (Buehler et al., 2012). In the present flare, a peak could not be resolved in the MeV – GeV spectrum, leaving the electron spectrum unconstrained at lower energies.

From electrodynamics, the Lorentz factor of electrons that would emit 200 MeV synchrotron radiation is

$$\gamma_{\rm sy} = 3 \times 10^9 \left(\frac{B}{\rm mG}\right)^{-0.5} , \tag{6.3.1}$$

and their energy-loss rate and life time are

$$\dot{E}_{\rm sy} = (8 \times 10^{-3}\ {\rm erg\ s^{-1}}) \left(\frac{B}{\rm mG}\right), \qquad \tau_{\rm sy} = (3 \times 10^5\ {\rm s}) \left(\frac{B}{\rm mG}\right)^{-1.5} . \tag{6.3.2}$$

Assuming a magnetic field of 1 mG in the emission region, similar to that deduced in Bednarek & Idec (2011), the flare duration $\tau_{\rm sy}$ is on the order of a few days, which is consistent with observed flares at a few hundred MeV. If the magnetic field were significantly stronger than 1 mG, the synchrotron lifetime would become very short compared to the flare duration, and so the electron population would need to be continuously replenished to sustain the flare. Thus, the main cause of the synchrotron flare was likely the injection of a large number of excess electrons at PeV energies.

As discussed in Section 4.3.1, Bednarek & Idec (2011) consider a model in which electrons are accelerated in reconnection regions of the magnetic field, and suggest variability above ~ 1 TeV of roughly 10% with more substantial changes above ~ 10 TeV as a result of inverse-Compton scattering. However, inverse-Compton scattering of soft photons by electrons with Lorentz factors $\sim 10^9$ is heavily Klein-Nishina suppressed and would provide γ-rays in the PeV band, beyond the sensitivity of VERITAS. Excess electrons with Lorentz factors of $\gamma_{\rm IC} \simeq 10^7$ could produce a flux enhancement at TeV energies, however, the non-detection of the flare with VERITAS poses challenges for this model and constrains the number of electrons with Lorentz factors of $\gamma_{\rm IC}$.

The number of electrons with Lorentz factors of $\sim 3 \times 10^9$ can be estimated as

$$N_{\rm e,sy} = \frac{L_{\rm sy}}{\dot{E}_{\rm sy}} \simeq 6 \times 10^{37} \left(\frac{B}{\rm mG}\right)^{-1} , \tag{6.3.3}$$

where $L_{\rm sy}$ is the synchrotron luminosity at 200 MeV. To calculate the number of electrons that may inverse-Compton scatter soft (IR) photons into the TeV band, the density of low-frequency radiation in the nebula must be known. To this end, the values of $L_{\rm soft} \sim 10^{37}$ erg s^{-1} (Marsden et al., 1984) as the PWN luminosity in IR photons, $\epsilon_{\rm soft} \sim 0.1$ eV as the photon energy, and $d_{\rm PWN} \simeq 1$ pc as the characteristic size of the Crab Nebula are used. The density of IR photons is then

$$n_{\rm soft} \simeq \frac{L_{\rm soft}}{4\pi\, d^2_{\rm PWN}\, c\epsilon_{\rm soft}} \simeq 20\ {\rm cm^{-3}}. \tag{6.3.4}$$

Using the upper limit on an extra flux component > 1 TeV given in Table 6.1, the enhanced inverse-Compton luminosity of the nebula is found to be $L_{\rm IC} \lesssim 4 \times 10^{32}$ ergs s^{-1}.

The number of electrons that upscatter photons to TeV energies is given by

$$N_{\rm e,IC} = \frac{L_{\rm IC}}{\sigma_{\rm T}\ n_{\rm soft}\ c\ \gamma m_e c^2}, \tag{6.3.5}$$

where $\sigma_{\rm T}$ is the Thomson cross-section. Ignoring the moderate Klein-Nishina suppression (the kinematic parameter $4\,\epsilon_{\rm soft}\epsilon_\gamma/(m_e^2\,c^4) \simeq 10$), the upper limit derived on excess TeV γ-rays corresponds to at most

$$N_{\rm e,IC}\left(\gamma \approx 10^7\right) \lesssim 10^{44}\ . \tag{6.3.6}$$

Assuming that the spectrum of excess electrons follows a power law, $N_e(\gamma) \propto \gamma^{-s}$, an estimate of the index s can be made by taking the ratio

$$\frac{N_{\rm e,IC}}{N_{\rm e,sy}} = \left(\frac{\gamma_{\rm IC}}{\gamma_{\rm sy}}\right)^{-s}, \tag{6.3.7}$$

which gives

$$s \lesssim \frac{6.2 + \log\left(\frac{B}{\rm mG}\right)}{2.5 - \frac{1}{2}\log\left(\frac{B}{\rm mG}\right)}\ . \tag{6.3.8}$$

This constrains $s \simeq 2.5$ for a magnetic field strength of 1 mG, which is harder than the index assumed by Bednarek & Idec (2011).

Overall, the non-detection by VERITAS of this flare from the Crab Nebula challenges the model of Bednarek & Idec (2011). The upper limits on the VHE flux increase during the flare period derived in this chapter of $5.3\% > 1$ TeV and $6.8\% > 4$ TeV are very competitive, and are clearly more constraining than the $\sim 10\% > 1$ TeV predicted by the model. In addition, the derived electron index is incompatible with those in this model. Due to the dearth of theoretical models with predictions for the VHE behaviour during flaring activity, we cannot suggest an alternative scenario, we can only discount this model in its current form. Any future model which attempts to explain the flaring process of the Crab Nebula will have to obey the constraints of these VHE observations.

6.4 Bibliography

Abdo, A. A., Ackermann, M., Ajello, M., et al., 2011; 'Gamma-ray flares from the Crab Nebula.' *Science (New York, N.Y.)*, vol. 331(6018):739

Abramowski, A., Aharonian, F., Benkhali, F. A., et al., 2013; 'H.E.S.S. Observations of the Crab during its March 2013 GeV Gamma-Ray Flare'. *eprint arXiv:1311.3187*

Aharonian, F., Akhperjanian, A. G., Bazer-Bachi, A. R., et al., 2006; 'Observations of the Crab nebula with HESS'. *Astronomy and Astrophysics*, vol. 457(3):899

Aharonian, F. A., Akhperjanian, A., Barrio, J. A., et al., 2001; 'Evidence for TeV gamma ray emission from Cassiopeia A'. *Astronomy and Astrophysics*, vol. 370:112

Aliu, E., Archambault, S., Aune, T., et al., 2014; 'A search for enhanced very-high-energy gamma-ray emission from the March 2013 Crab Nebula flare'. *The Astrophysical Journal*, vol. 781(1):L11

Balbo, M., Walter, R., Ferrigno, C., et al., 2011; 'Twelve-hour spikes from the Crab Pevatron'. *Astronomy & Astrophysics*, vol. 527:L4

Bednarek, W., Idec, W., 2011; 'On the variability of the GeV and multi-TeV gamma-ray emission from the Crab nebula'. *Monthly Notices of the Royal Astronomical Society*, vol. 414(3):2229

Berge, D., Funk, S., Hinton, J., 2007; 'Background modelling in very-high-energy $\{\gamma\}$-ray astronomy'. *Astronomy and Astrophysics*, vol. 466:1219

Buehler, R., Scargle, J. D., Blandford, R. D., et al., 2012; 'GAMMA-RAY ACTIVITY IN THE CRAB NEBULA: THE EXCEPTIONAL FLARE OF 2011 APRIL'. *The Astrophysical Journal*, vol. 749(1):26

Errando, M., Orr, M., 2011; 'Automated analysis of Fermi-LAT data to trigger ground-based gamma-ray observations'. In 'Proc. of the 32nd International Cosmic Ray Conference', vol. 8 of *International Cosmic Ray Conference*, 135

Greisen, K., Ball Jr., S. E., Campbell, M., et al., 1975; 'Change in the high-energy radiation from the Crab'. *The Astrophysical Journal*, vol. 197:471

Kirsch, M. G., Briel, U. G., Burrows, D. N., et al., 2005; 'Crab: the standard X-ray candle with all (modern) X-ray satellites'. In 'Society of Photo-Optical Instrumentation Engineers (SPIE) Conference Series', , (ed. Siegmund, O. H. W.), vol. 5898 of *Society of Photo-Optical Instrumentation Engineers (SPIE) Conference Series*, 22–33

Mariotti, M., 2010; 'No significant enhancement in the VHE gamma-ray flux of the Crab Nebula measured by MAGIC in September 2010'. *The Astronomer's Telegram*, vol. 2967

Marsden, P. L., Gillett, F. C., Jennings, R. E., et al., 1984; 'Far-infrared observations of the Crab nebula'. *The Astrophysical Journal*, vol. 278:L29

Mayer, M., Buehler, R., Hays, E., et al., 2013; 'RAPID GAMMA-RAY FLUX VARIABILITY DURING THE 2013 MARCH CRAB NEBULA FLARE'. *The Astrophysical Journal*, vol. 775(2):L37

McBreen, B., Ball Jr., S. E., Campbell, M., et al., 1973; 'Pulsed high-energy gamma rays from the Crab nebula.' *The Astrophysical Journal*, vol. 184:571

Ojha, R., Hays, E., Buehler, R., et al., 2013; 'Fermi LAT detection of a new gamma-ray flare from the Crab Nebula region'. *The Astronomer's Telegram*, vol. 4855:1

Ong, R. A., 2010; 'Search for an Enhanced TeV Gamma-Ray Flux from the Crab Nebula with VERITAS'. *The Astronomer's Telegram*, vol. 2968

Striani, E., Tavani, M., Piano, G., et al., 2011; 'THE CRAB NEBULA SUPER-FLARE IN 2011 APRIL: EXTREMELY FAST PARTICLE ACCELERATION AND GAMMA-RAY EMISSION'. *The Astrophysical Journal*, vol. 741(1):L5

Striani, E., Tavani, M., Vittorini, V., et al., 2013; 'VARIABLE GAMMA-RAY EMISSION FROM THE CRAB NEBULA: SHORT FLARES AND LONG WAVES'. *The Astrophysical Journal*, vol. 765(1):52

Tavani, M., Bulgarelli, A., Vittorini, V., et al., 2011; 'Discovery of powerful gamma-ray flares from the Crab Nebula.' *Science (New York, N.Y.)*, vol. 331(6018):736

Toor, A., Seward, F. D., 1974; 'The Crab Nebula as a calibration source for X-ray astronomy'. *The Astronomical Journal*, vol. 79:995

Vernetto, S., 2010; 'Enhanced TeV gamma ray flux from the Crab Nebula observed'. *The Astronomer's Telegram*, vol. 2921

—, 2013; 'Study of the Crab Nebula TeV emission variability during five years with ARGO-YBJ'. In 'Proceedings of the 33rd International Cosmic Ray Conference', 4. Rio de Janeiro, Brazil

Weekes, T. C., Cawley, M. F., Fegan, D. J., et al., 1989; 'Observation of TeV gamma rays from the Crab nebula using the atmospheric Cerenkov imaging technique'. *The Astrophysical Journal*, vol. 342:379

Wilson-Hodge, C. A., Cherry, M. L., Case, G. L., et al., 2011; 'WHEN A STANDARD CANDLE FLICKERS'. *The Astrophysical Journal Letters*, vol. 727(2):L40

CHAPTER 7

The search for short-term flares in the extended VHE Crab Nebula data set

It is always exciting to acquire new data to gain contemporary results and up-to-the-minute insights into the behaviour of a source, such as was achieved in Chapter 6. However, a wealth of VHE Crab Nebula data already exists, spanning many years, and should not be overlooked. VERITAS has observed the Crab Nebula regularly since 2007, accumulating hundreds of hours of observations of the source. The Whipple 10 m Telescope has an even larger archive of data on this source. Given the recent revelations in our understanding of the Crab Nebula's emission, it is of particular relevance at this time to conduct a systematic search for VHE variability in this extensive archive of data.

This chapter reports on the search for short-term flares in an extended data set on the Crab Nebula. Data from the Whipple 10 m Telescope spanning the years 2000 – 2010 and more recent data from VERITAS spanning the years 2007 – 2013 is tested for short-term temporal variability, of the order of that observed by *Fermi*-LAT and AGILE.

It would be interesting to also test for secular variation such as that reported by Wilson-Hodge et al. (2011), but such a study is greatly hindered by the fact the IACTs have traditionally used the Crab Nebula as a calibration source. In the past, any variation in the emission from the nebula observed by these experiments would have been interpreted as an issue with the instrument itself, and the instrument would be adjusted until the expected spectrum was observed from the source. In light of the results of Chapter 6, namely, the non-detection of the recent flare at VHE energies, it would seem that this interpretation may be appropriate. However, any genuine decline in the emission will be masked by these adjustments, rendering any retrospective search for its presence extremely difficult. Therefore, such a study is not addressed in this work.

7.1 The search in Whipple 10 m Telescope data

A data set of Crab Nebula observations taken with the Whipple 10 m Telescope was compiled from the years $2000 - 2010$. Data were taken in 28-minute observations in *paired mode*, whereby observations of the source are matched to observations of blank sky data for the purposes of background estimation. For selection, data were required to be accumulated with a standard experimental setup under good weather conditions at zenith angles $< 35°$.

The data were analysed using the standard Supercuts procedure described in Appendix B of Reynolds et al. (1993) and described in Chapter 3. A light curve in units of γ-rays per minute of the Crab Nebula is created for each observing season, binned by observation. Each light curve is fit with a constant rate to test for temporal stability. All seasons are found to be consistent with the constant fit (a constant rate model would only be confidently rejected below a probability of fit of 5.7×10^{-7}, corresponding to a $5\,\sigma$ threshold for rejection). The seasonal light curves drawn with the constant rate fit and parameters are shown in Figure 7.1.

The data set is searched for short-term flux variability. Two independent methods are employed to achieve this. First, a sliding window algorithm is used to test for variability on specific, pre-defined timescales. This method is relatively simple and unsophisticated, yet is a useful tool to begin the search. Toy Monte Carlo simulations are developed to help understand the significance of the results and to test the sensitivity of the search. On the basis of these simulations, this method is only projected to be sensitive to a 2-fold increase in flux. Therefore, a more sophisticated algorithm, namely the Bayesian block binning algorithm presented in Scargle et al. (2013) and described in Chapter 3, is implemented. This does not perform a search on specific timescales, rather it seeks to characterise variability of any sort in the data set. The results of both methods are presented here.

7.1.1 Sliding window algorithm

The data set is searched for short-term variability on specific timescales of 7 and 14 days, motivated by the flaring timescales reported by *Fermi*-LAT and AGILE. A shorter timescale of 1 day is also tested. A sliding window algorithm was developed to perform this analysis. The algorithm groups observations by their timestamps into nightly bins and a search window of

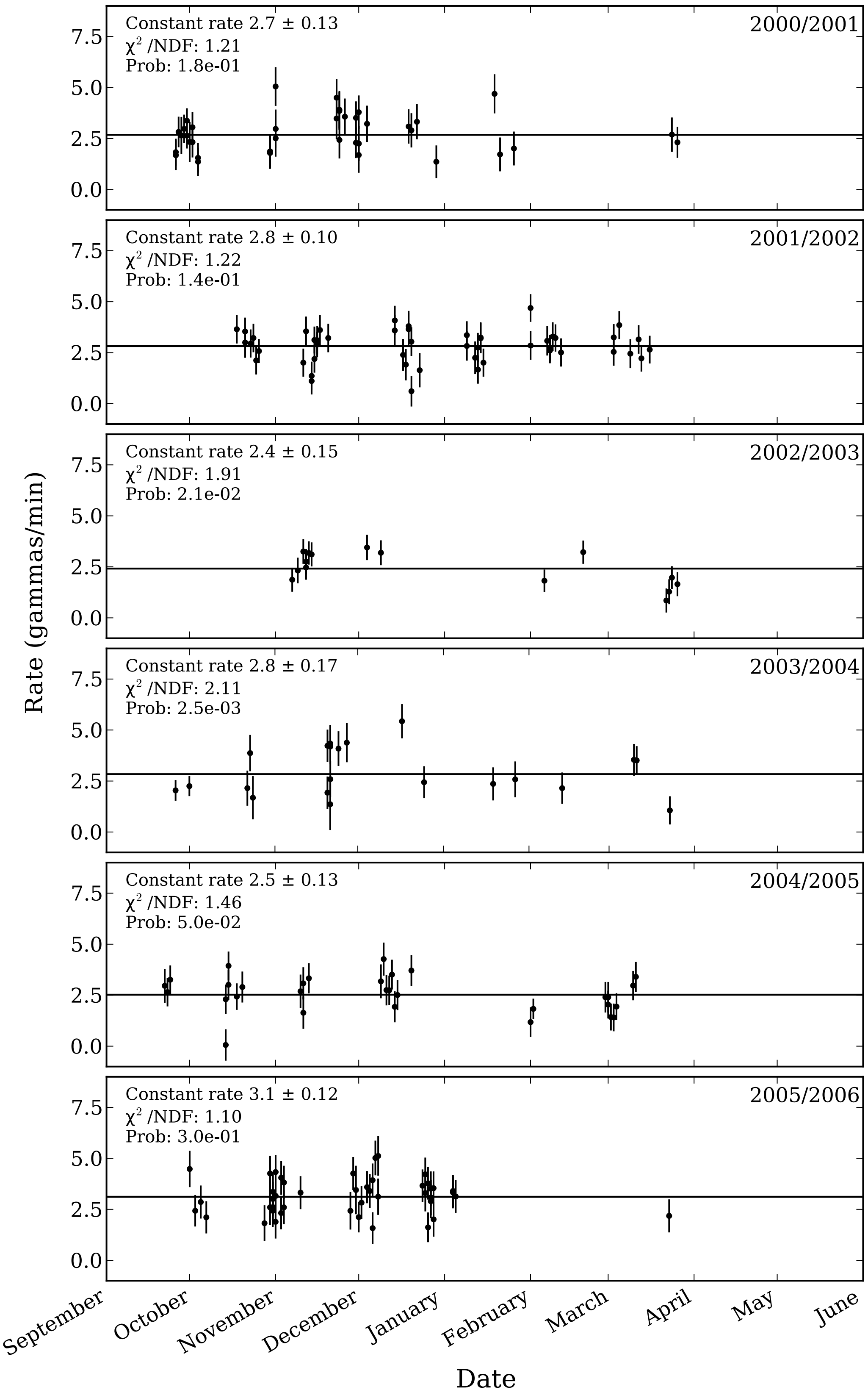
Constant rate 2.7 ± 0.13
χ^2 /NDF: 1.21
Prob: 1.8e-01
2000/2001
Constant rate 2.8 ± 0.10
χ^2 /NDF: 1.22
Prob: 1.4e-01
2001/2002
Constant rate 2.4 ± 0.15
χ^2 /NDF: 1.91
Prob: 2.1e-02
2002/2003
Constant rate 2.8 ± 0.17
χ^2 /NDF: 2.11
Prob: 2.5e-03
2003/2004
Constant rate 2.5 ± 0.13
χ^2 /NDF: 1.46
Prob: 5.0e-02
2004/2005
Constant rate 3.1 ± 0.12
χ^2 /NDF: 1.10
Prob: 3.0e-01
2005/2006
7.5
5.0
2.5
0.0
Rate (gammas/min)
September
October
November
December
January
February
March
April
May
June
Date

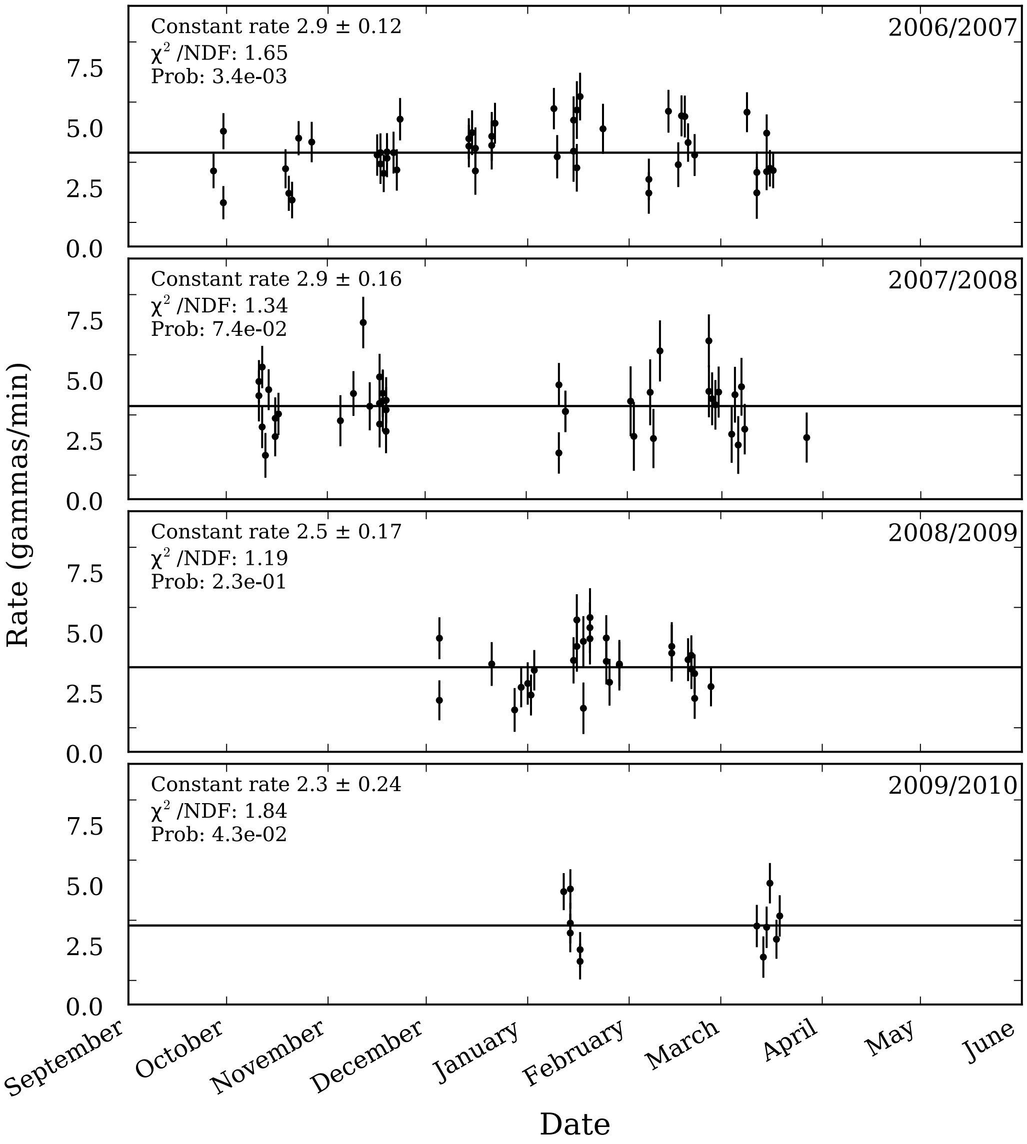

Figure 7.1: Whipple 10 m Telescope light curves, binned by observation, of the Crab nebula for each observing season spanning the years 2000 – 2010. Each season is fit with a constant rate, the result of which is shown on each panel. All seasons are consistent with the constant fit.

the chosen length is iteratively shifted along the data set night-by-night for each season. For each iteration, the average rate inside the window is compared to the average rate outside the window, which includes data both before and after the window. The significance of the signal in the window is calculated according to

$$S = \frac{N_w - \alpha N_o}{\sqrt{N_w + \alpha^2 N_o}}, \tag{7.1.1}$$

where N_w is the number of counts in the window, N_o is the number of counts outside the window, and α is the ratio of the window duration to the non-window duration.

Each window tested for elevated emission is effectively a trial in the search for variability from the source. This means that an appropriate statistical penalty must be paid to account for the total number of tests performed. The penalty is applied to the probability $P_{\textsf{pre}}$ obtained from the sliding window analysis according to

$$P_{\textsf{post}} = 1 - (1 - P_{\textsf{pre}})^N, \tag{7.1.2}$$

where N is the number of trials, (e.g., Biller, 1996).

Figure 7.2 shows the window significances for search timescales of 1, 7 and 14 days for the 11 observing seasons. The highest significance detected in a 1-day window was $3.42\,\sigma$ pre-trials, corresponding to a post-trials significance of $\sim 2.07\,\sigma$. Both 7- and 14-day search windows yielded lower post-trials maximum significances of $\sim 1.38\,\sigma$ and $\sim 1.59\,\sigma$ respectively. Thus, there is no evidence for strong VHE flaring activity on these timescales in this data set.

Figure 7.3 shows the distribution of window significances obtained for the different search timescales for the entire data set. The variances of the Gaussian fits to the significance histograms are not consistent with 1.0, indicating that the observed variations are not solely due to statistical fluctuations. Randomising the dates of the observations and reanalysing the "shuffled" data preserves the width of the distributions, implying that it is independent of the configuration of the data.

There are a number of factors that likely contribute to this phenomenon. The non-uniform zenith angle of observations is a possible cause. Selecting data in narrow zenith bands (e.g., 10°) could ameliorate this effect, however, such a study would suffer from drastically reduced statistics. Atmospheric changes are another likely cause, but cannot be corrected for due to the lack of rigorous on-site weather monitoring. For example, dust particles in the air due to the desert environment and occasionally particulate matter from local forest fires affect atmospheric transparency in the vicinity of the telescope. The is also some evidence that the gains of the

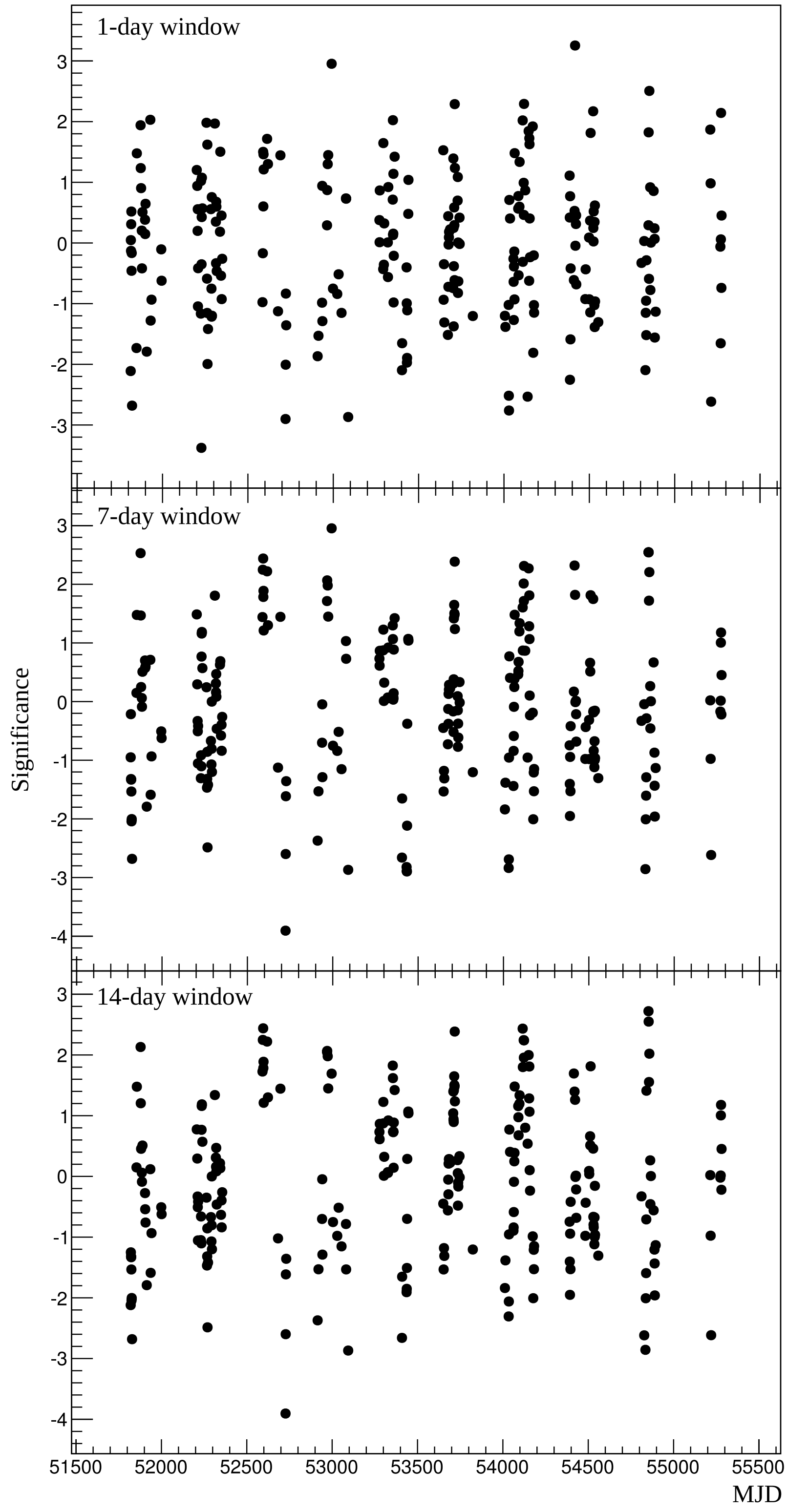

Figure 7.2: 1-, 7-, and 14-day pre-trials window significances for the 11 years of Whipple data analysed are shown from top to bottom. No hint of elevated emission is present in any of the searches. Correcting for the trials factor reduces the spread of these significances even further.

PMTs are temperature dependent, but the analysis package does not include a correction for this.

Characterising the search results

In general, this method produces windows that are not independent, as each window may include runs that also constitute neighbouring windows. A Monte Carlo simulation was developed to confirm that the significance histograms are consistent with statistics, given the overlapping search windows. Simulations of observations were created using Poisson distributions with a constant mean for the source and background rates. The means of these distributions were set to those observed in the real data. Observations were simulated for 18,000 nights with the same source sampling distribution as the real data and analysed. It was found that significance histograms produced with the three search timescales from the simulated data have variances very close to 1.0. Figure 7.4 shows the Gaussian fits to the significance histograms from these simulations.

Another 25,000 individual data sets, equivalent in length and sampling to the observational data, were then simulated and analysed. A distribution of the variances was produced. A variance of > 1.2 (as seen in the real data) was observed in only two cases. This confirms that the source of the broadness of the data distributions is non-statistical in nature. Figure 7.5 shows the distribution of the variances obtained when using a 7-day search window on this simulated data.

The code was adapted to simulate a single flare of known length and emission within an otherwise standard data set. The data sampling was adjusted to ensure one simulated observation per night for the duration of the flare, while still maintaining random sampling in the rest of the data set. This idealised scenario of full sampling of the flare provides the means to put an upper limit on the level of flaring activity that would be detected. The simulation was run 600 times for two different flare emission levels. In both cases, a medium flare duration of 5 days was used, with flare emission levels of $\times 2$ and $\times 1.5$ the average Crab Nebula flux.

Figure 7.6 shows typical data sets obtained for both flare emission levels. For a 7-day window, it was found that the $\times 2$ flare was detected above the $5\,\sigma$ level post-trials in 69% of the data sets. The $\times 1.5$ flare was only detected at the $5\,\sigma$ level post-trials once. These numbers are used for a simple thought experiment outlined below to estimate the level of flaring that may be present in the data set.

Flares in the Mev$-$GeV range have been detected from the Crab Nebula in the last seven years

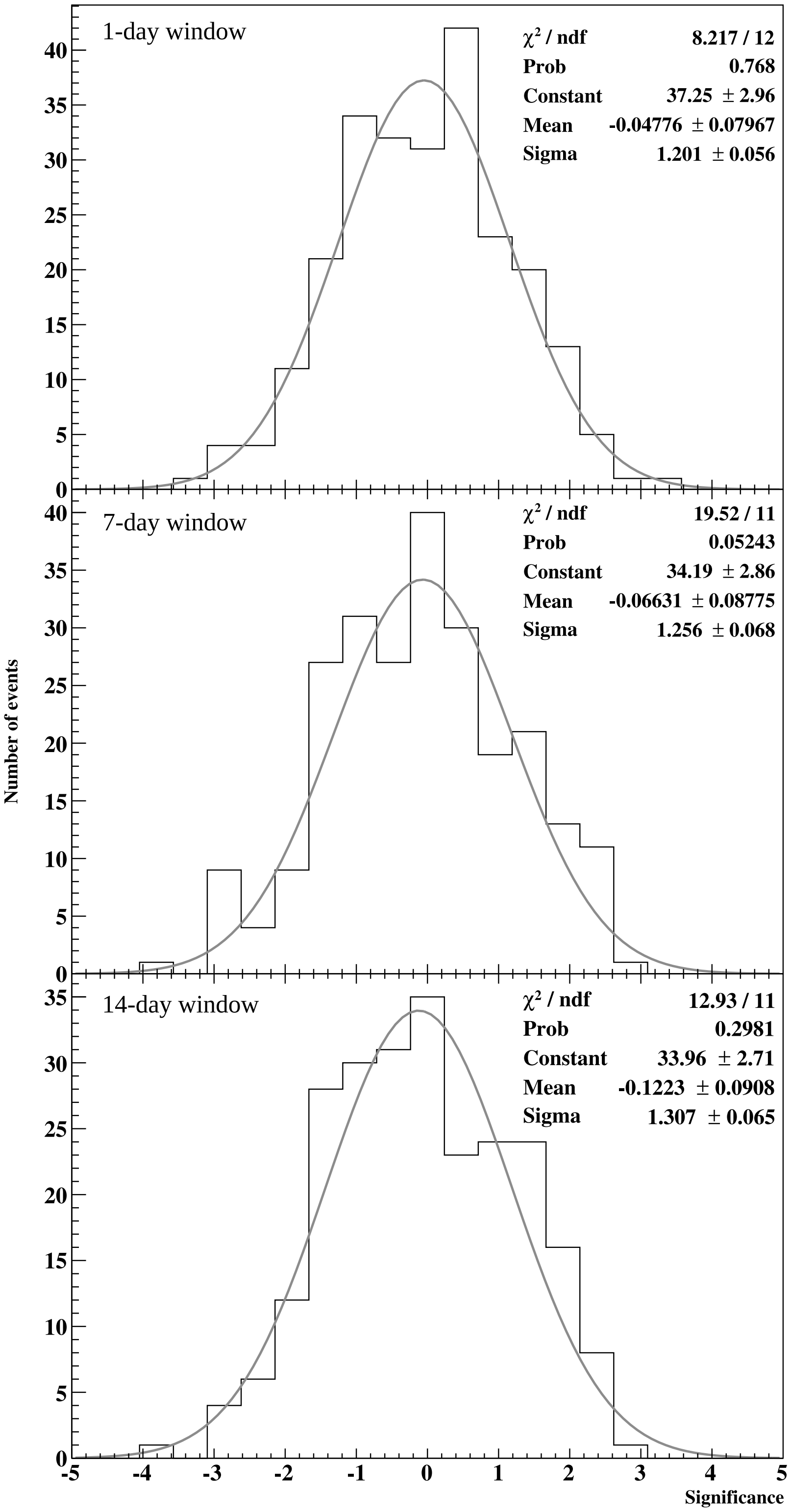

Figure 7.3: Distributions of window significances obtained for 1-, 7-, and 14-day search windows are shown from top to bottom. The Gaussian fit and corresponding parameters for each distribution are also shown. The variances are not consistent with 1.0, implying that the observed variations are not solely due to statistical fluctuations.

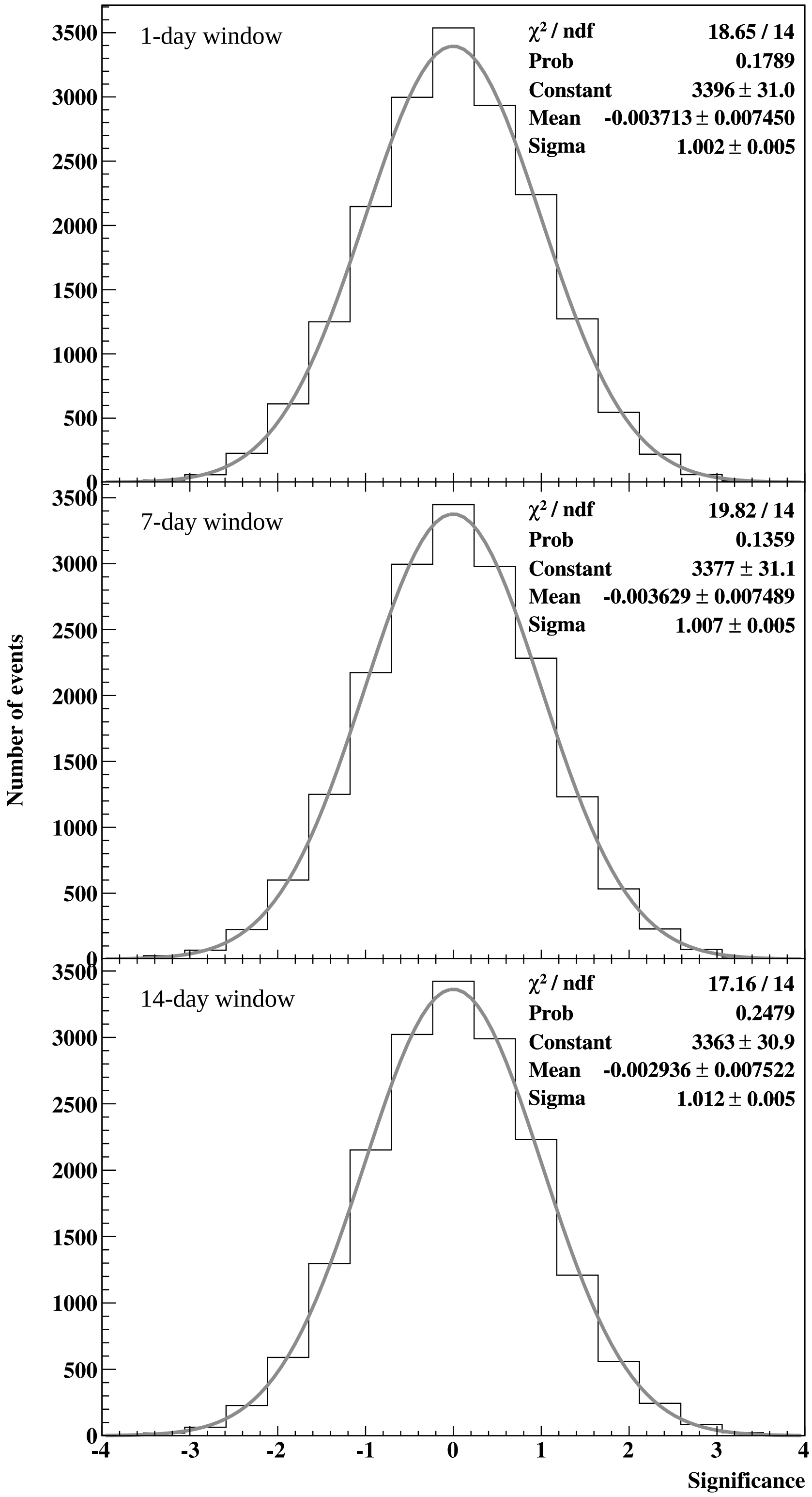

Figure 7.4: Gaussian fits to the significance histograms produced from the simulated 18,000 nights. In contrast to the data, these are found to have variances very close to 1.0.

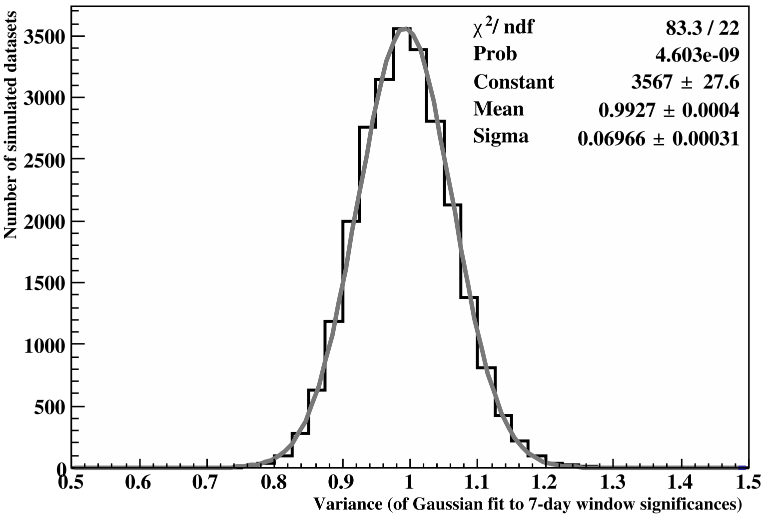

Figure 7.5: Distribution of the variances of the significance distributions for a 7-day search window run on the simulations. A variance of > 1.2, representative of the results from the real data analysis, was observed in only 2 cases, making it an extremely unlikely statistical result.

with an average rate of ~ 0.7 flares per year. In the Whipple data set, the Crab Nebula is observed over about three months per year (it is visible for ~six months, but observations were impossible during bright moon periods) for ten years. This yields an estimate of ~ 1.75 flares present in the entire data set, which rounds to 2 for simplicity. From the simulations, the probability of not detecting a 2-fold flare is 0.31, so the probability of not detecting two such flares is 9.6×10^{-2}. Therefore, we are 90% confident that the anticipated number of flares are not present in the Whipple 10 m Telescope data at the 2-fold level. Performing the same steps considering the smaller flare level simulated, the presence of 1.5-fold flares in the data set cannot be ruled out.

In order to be confidently detected with this sliding window method, a flare would need to be at least double the average flux of the Crab Nebula. Considering the model of Bednarek & Idec (2011) for the sake of argument, due to a lack of other predictions for VHE behaviour, VHE variation of the order of $\sim 10\%$ may be expected. Therefore, this type of sliding window search is insensitive to the low level of flaring activity that may be present in the source.

7.1.2 Bayesian block algorithm

The data set is searched for variability again, this time utilising the more sophisticated Bayesian block binning algorithm (Scargle et al., 2013). This is described in some detail in Chapter 3, but in brief, the algorithm locates and characterises variability on any timescale in the context of a false-positive probability that is provided in advance.

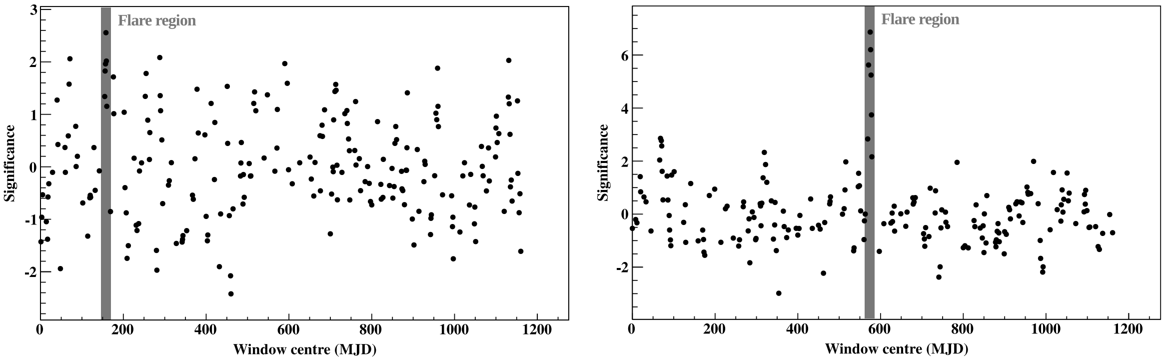

Figure 7.6: Window significances for simulated flare of 5-day duration. The left panel shows a flare with a 50% increase in emission over average levels, and the right panel shows a flare with a 100% increase in emission over average levels. The flare in the left panel is not identified by the sliding window algorithm, whereas that shown on the right is significantly detected.

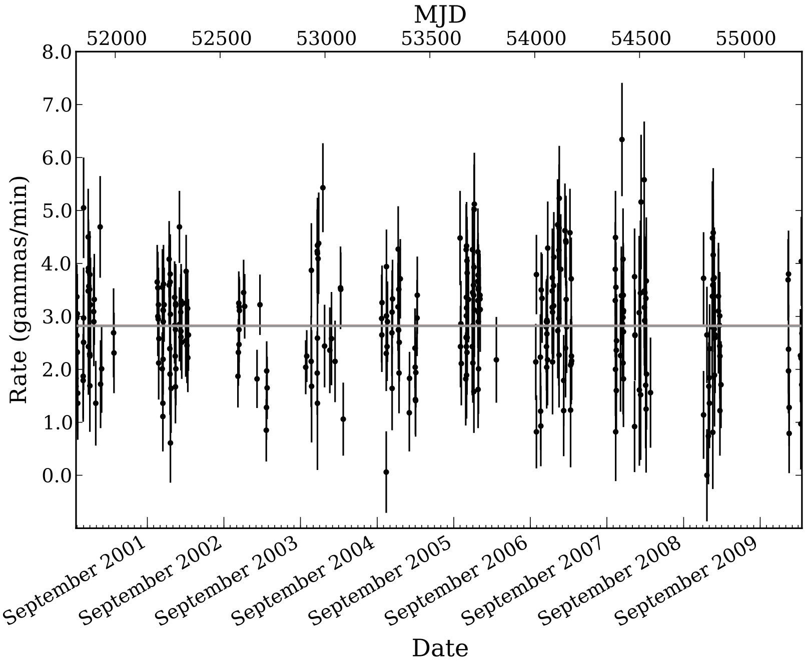

Figure 7.7: Optimal temporal binning of the Whipple 10 m Telescope data set, covering the seasons 2000 − 2010. A false-positive probability of 0.01 is used in this analysis. The algorithm chooses a single bin (shown as the solid grey line) as the best representation of the data, implying this data is consistent with constant emission.

Figure 7.7 shows the result of the Bayesian block binning on the data set. A false-positive probability of 0.01 is chosen for this analysis. The light curve is best described by a single time bin, which implies that it is consistent with a constant source emission model. This is in agreement with the results of the sliding window algorithm.

A similar set of simulations to those used to quantify the sensitivity of the sliding window method were produced in order to perform the same test for the Bayesian block algorithm. Three different flare levels were simulated 600 times each. In all cases, a medium flare duration of 5 days was used, with flare emission levels of $\times 2$, $\times 1.5$ and $\times 1.1$ the average Crab Nebula flux. The $\times 2$ flare level was detected in 92% of cases, the $\times 1.5$ level was detected in 6.5% of cases, and the $\times 1.1$ flare level was detected exactly once. Performing a similar set of steps as before, we are 99.4% confident that the anticipated number of flares (2) are not present in the Whipple 10 m Telescope data at the 2-fold level, using the Bayesian block algorithm. While this method is more sensitive, it still struggles to detect low levels of variation in the rate on short timescales.

7.2 The search in VERITAS data

The successor to the Whipple 10 m Telescope, VERITAS entered full operation in September 2007. The stereoscopic system and superior hardware make VERITAS significantly more sensitive than the Whipple telescope. Since 2007, VERITAS has accumulated hundreds of hours of observations on the Crab Nebula. Although the search for short-term variability in the Whipple archival data did not result in any significant VHE flare candidates, the increased sensitivity of VERITAS provides the opportunity to further probe the emission from this source.

A data set was compiled of all VERITAS observations of the Crab Nebula since the complete array entered operation. Only observations taken with the full four-telescope array were considered for this study. The data were taken in wobble mode, with an offset from the source position in each of the four cardinal alternately (Aharonian et al., 2001; Berge et al., 2007). In general, a wobble offset of $0.^{\circ}5$ was used, but offsets up to $1.^{\circ}3$ from the source were occasionally present. This data set comprises 157.05 hours of live time on the source taken over the full range of zenith angles $5^{\circ} - 65^{\circ}$.

A cut on zenith angle, similar to that imposed on the data in the Whipple study, could be applied to the VERITAS data. However, this would significantly reduce the amount of data available for this analysis, reducing the overall effectiveness of the study. The flux reconstruction of the VERITAS data analysis is rigorous enough to robustly account for a wide range of observing angles.

In this analysis, images composed of fewer than five pixels are rejected. For each image, mean scaled width and mean scaled length parameters are required to be in the range 0.05 − 1.1 and 0.05 − 1.3 respectively. The altitude of the maximum Cherenkov emission from the reconstructed shower is required to be higher than 7 km above the array. A circular region of radius $0.^{\circ}1$ centered on the source coordinates is defined from which γ-ray like events are selected. These constitute

Season	RMS spread on flux (%)
2007/2008	23.97
2008/2009	17.92
2009/2010	26.59
2010/2011	13.20
2011/2012	15.75
2012/2013	17.69
All	20.85

Table 7.1: RMS spread of the flux in the VERITAS light curves from Figure 7.8.

the standard cut levels for VERITAS.

A nightly light curve is constructed individually for each season of VERITAS observations, and these are shown in Figure 7.8. Each light curve is fit with a constant flux as a preliminary test for stability, and all seasons are found to be consistent with a constant flux (a constant rate model would only be confidently rejected below a probability of fit of 5.7×10^{-7}, corresponding to a $5\,\sigma$ threshold for rejection). This fit, along with the corresponding parameters, are shown for each observing season on the light curves.

Some scatter in the Crab Nebula flux about the average value is evident in the seasonal light curves. Aharonian et al. (2006) report a RMS spread of 15% on the integral flux of the Crab Nebula as detected by H.E.S.S. in 2003 and 2004. In general, the RMS spread in the VERITAS data is slightly larger than that observed by H.E.S.S. This spread is likely due to the atmospheric effects described in Section 7.3. Table 7.1 summarises the RMS spread of the flux in the VERITAS light curves.

The Bayesian block binning algorithm is run on the total light curve to test for variability in the data set. As before, a false-positive probability of 0.01 is chosen for this analysis. The optimum temporal binning of the data set is shown in Figure 7.9. The light curve is best represented by two bins with the change point located at February 2, 2011. The significance of the change point, obtained by comparing the fitness of the block representation with the change point to fitness of the block representation if the change point did not exist is calculated to be 36.86, corresponding to $\sim 6\,\sigma$. While the presence of a change point is unexpected, this representation of the data is not consistent with the type of short-term variability that would be evidence of a flare at VHE energies. Therefore, this analysis of the VERITAS data is in agreement with the study of the Whipple data, where no evidence for significant flaring activity was found.

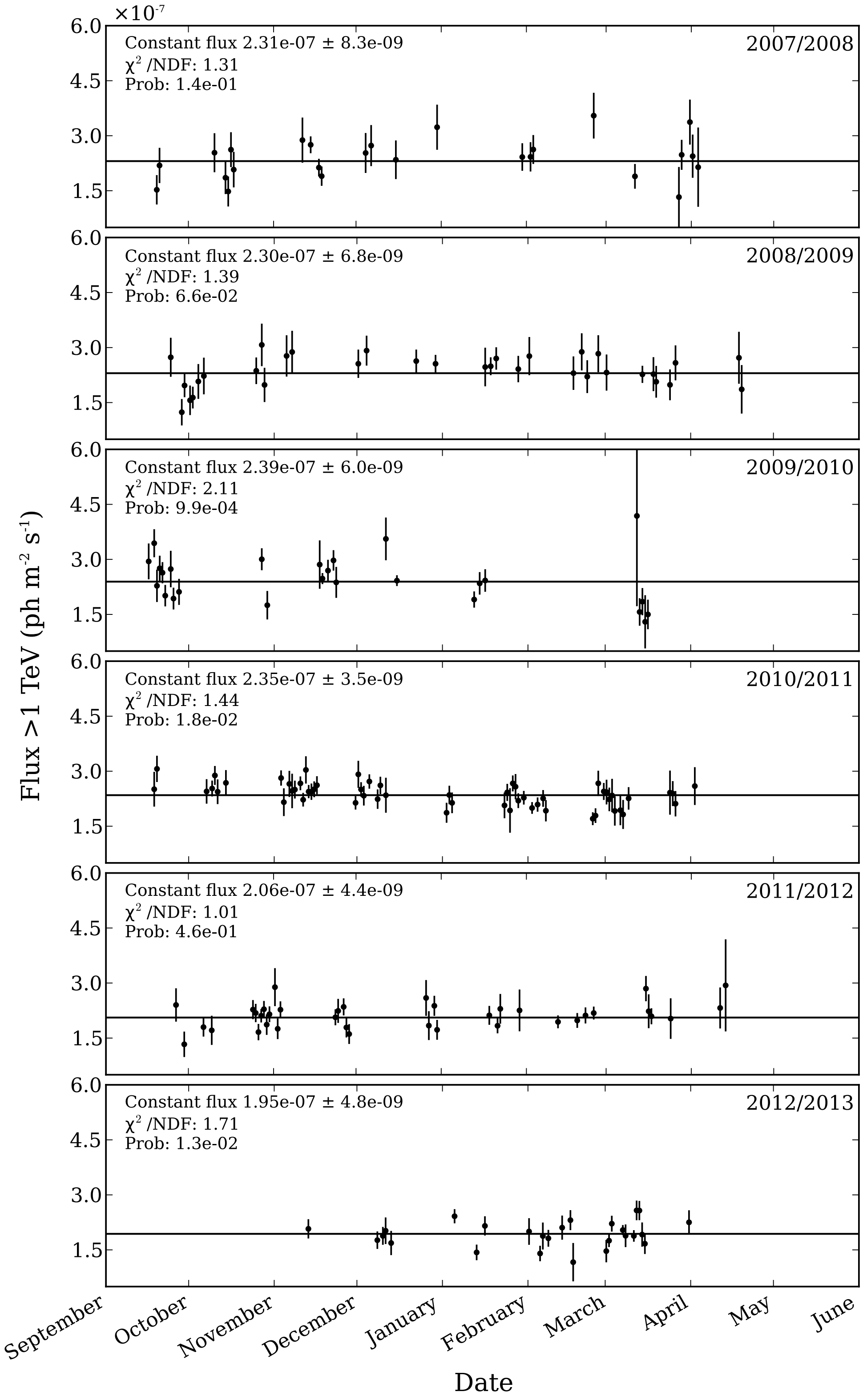

Figure 7.8: VERITAS light curves in nightly bins of the Crab Nebula for each observing season spanning the years 2007−2013. The light curve of each season is fit with a constant flux, the result of which is drawn as the horizontal line on each panel. The fit information for each season is also shown in the respective panels.

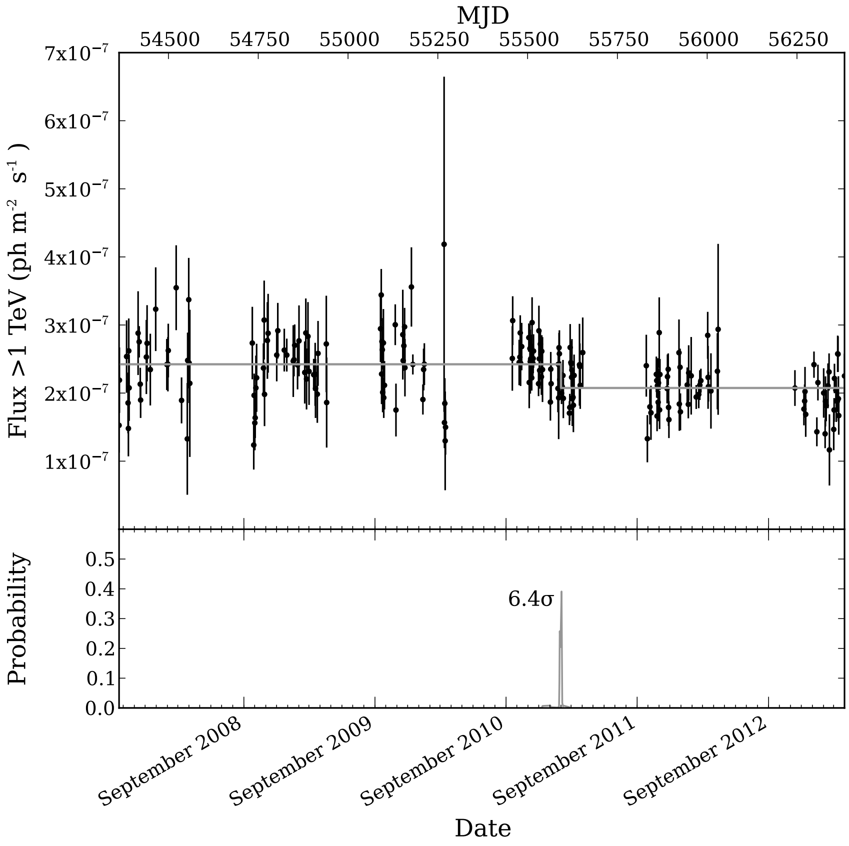

Figure 7.9: Results of the Bayesian block binning of the long-term VERITAS light curve of the Crab Nebula using a false-positive probability of 0.01. The data is best represented by two bins with the change point located at February 2, 2011. The lower panel of this plot shows the probability distribution of the location of the change point. It is seen to be sharply peaked about the chosen location, showing that its placement is robust. The significance of the change point, obtained by comparing the fitness of the block representation with the change point to fitness of the block representation if the change point did not exist, is displayed beside the trace on the lower panel.

7.3 Discussion

The VHE emission of the Crab Nebula from 2000 to 2013 has been searched for short-term variability using data from the Whipple 10 m Telescope and VERITAS. The Whipple data set was first investigated using a sliding window algorithm, testing for variability on timescales similar to the flares observed at lower energies. No evidence for statistically significant flaring activity was found. Monte Carlo simulations indicate that a flare would need to exhibit a 2-fold increase in flux in order to be significantly detected. The sliding window search is insensitive to any lower level of flaring that may be present in the source.

The Bayesian block binning algorithm was then employed to test the same data set for variability.

This constitutes a more sensitive analysis to characterise any variability that may be present in the data. This algorithm does not have a preferred timescale on which to test the data, and as such is not biased towards detecting short-term variability. In agreement with the initial sliding window search, no evidence for significant flaring activity in the emission was found.

To further the search, VERITAS data from 2007 onward was then introduced into the study. The improved sensitivity of VERITAS and more rigorous data analysis chains increase the likelihood of detecting any flaring activity that may be present. The Bayesian block binning algorithm was applied to the data and found that the optimum representation was two blocks, with a change point occurring in February 2011. This representation of the data is not consistent with the type of short-term variability that would be evidence of a flare at VHE energies. Therefore, it is in agreement with the study of the Whipple data, where no evidence for significant flaring activity was found.

This single change point, while statistically significant, is not enough to imply that there is a decline in the baseline VHE emission from the Crab Nebula. Such a claim would be extremely difficult to validate given that the Crab Nebula is used as a calibration source for VHE instruments, including VERITAS. It is of note that preliminary atmospheric studies undertaken, show that the local atmosphere around the VERITAS site may be becoming more unstable in its lower aerosol contents. Current analysis, still in the preliminary stages, indicates that the lower aerosol contents are fluctuating in a random manner that does not appear to follow any seasonal trends.

A recent publication from the H.E.S.S. Collaboration (Hahn et al., 2014) shows the effect of the atmospheric aerosol content at the H.E.S.S. site on the spectral reconstruction of Crab Nebula data taken over 8 years of operation. To achieve this, the “Cherenkov transparency coefficient” T is introduced, which is designed to be as hardware-independent as possible to separate hardware-related effects from those caused by large-scale atmospheric absorption. It is defined as

$$T \equiv \frac{1}{N k_N} \sum_i \frac{R_i^{\frac{1}{1.7}}}{\mu_i g_i} \tag{7.3.1}$$

where N is the number of telescopes, k_N is a scaling factor to ensure the resulting distribution peaks at unity, R_i is the zenith-corrected trigger rate of the i^{th} telescope, μ_i is the muon efficiency of the i^{th} telescope, and g_i is the average pixel gain of the i^{th} telescope. Figure 7.10 shows the impact of the Cherenkov transparency coefficient on the flux normalisation and spectral index of Crab Nebula observations. A very strong T-dependence of the flux normalisation is observed, with lower transparency coefficients yielding lower flux normalisations. If the aerosol content at the VERITAS site is in fact becoming more unstable, the local Cherenkov transparency coefficient

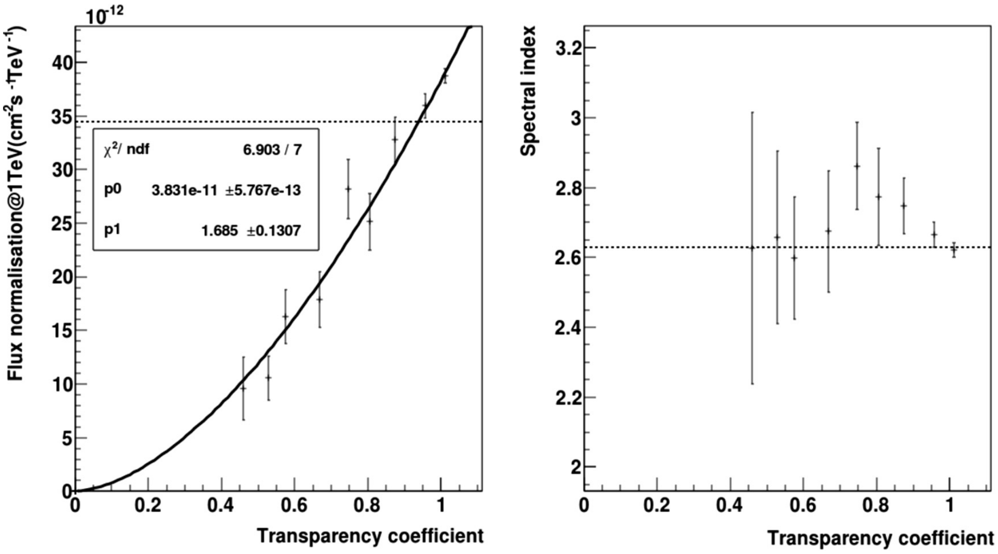

Figure 7.10: Impact of the Cherenkov transparency coefficient on the spectral parameters of the Crab Nebula observed by H.E.S.S. (Hahn et al., 2014). The flux normalisation is found to be strongly dependent on the transparency coefficient, while the spectral index shows no significant dependence.

is similarly increasingly unstable, and could certainly account for the change point observed in February 2011.

The overall results of the analyses presented in this chapter are consistent with that presented in Chapter 6, which found no enhancement of the VHE flux during the March 2013 GeV flare. The data analysed here span 13 years and hundreds of hours of live time on the source. The detection of TeV variability in the Crab Nebula would be a hugely important result for determining the flare mechanism, and would have strong implications for using the nebula as a standard candle of VHE astronomy. The fact that such a detection has not made in this comprehensive data set which covers both archival and data contemporaneous with GeV flares suggests that such a detection is beyond the current generation of IACT telescopes. However, the current instrumentation still plays an important role, as their observations provide a necessary component of any multiwavelength SED and any new theoretical model must also be capable of explaining the behaviour of the VHE emission.

7.4 Bibliography

Aharonian, F., Akhperjanian, A. G., Bazer-Bachi, A. R., et al., 2006; 'Observations of the Crab nebula with HESS'. *Astronomy and Astrophysics*, vol. 457(3):899

Aharonian, F. A., Akhperjanian, A., Barrio, J. A., et al., 2001; 'Evidence for TeV gamma ray emission from Cassiopeia A'. *Astronomy and Astrophysics*, vol. 370:112

Bednarek, W., Idec, W., 2011; 'On the variability of the GeV and multi-TeV gamma-ray emission from the Crab nebula'. *Monthly Notices of the Royal Astronomical Society*, vol. 414(3):2229

Berge, D., Funk, S., Hinton, J., 2007; 'Background modelling in very-high-energy $\{\gamma\}$-ray astronomy'. *Astronomy and Astrophysics*, vol. 466:1219

Biller, S. D., 1996; 'Hypothesis ranking and the context of probabilities in an open-ended search'. *Astroparticle Physics*, vol. 4(3):285

Hahn, J., de los Reyes, R., Bernlöhr, K., et al., 2014; 'Impact of aerosols and adverse atmospheric conditions on the data quality for spectral analysis of the H.E.S.S. telescopes'. *Astroparticle Physics*, vol. 54:25

Reynolds, P. T., Akerlof, C. W., Cawley, M. F., et al., 1993; 'Survey of candidate gamma-ray sources at TeV energies using a high-resolution Cerenkov imaging system - 1988-1991'. *The Astrophysical Journal*, vol. 404:206

Scargle, J. D., Norris, J. P., Jackson, B., et al., 2013; 'STUDIES IN ASTRONOMICAL TIME SERIES ANALYSIS. VI. BAYESIAN BLOCK REPRESENTATIONS'. *The Astrophysical Journal*, vol. 764(2):167

Wilson-Hodge, C. A., Cherry, M. L., Case, G. L., et al., 2011; 'WHEN A STANDARD CANDLE FLICKERS'. *The Astrophysical Journal Letters*, vol. 727(2):L40

Chapter 8

Future prospects and conclusions

The goal of this thesis was to study two interesting VHE sources, both exhibiting IC γ-ray emission despite belonging to radically different source categories. The first, 1ES 1959+650, is a high-frequency peaked BL Lac object - the single most numerous source type in VHE astronomy. The SED was modelled with a SSC + EC model, which was found not to provide a fully accurate representation of the data. Assuming this model for the source regardless, the parameters obtained suggest that the commonly-invoked first-order Fermi acceleration at parallel shocks cannot describe the observed emission. Instead, the source may consist of an inhomogeneous jet with a fast inner spine and slower-moving outer cocoon.

Due to the low statistics, it was not viable to produce time-resolved VHE spectra for the source. However, had it been possible to create VHE spectra corresponding to the differing X-ray states, a clearer picture of the source behaviour would have been obtained. This would perhaps simplify the theoretical interpretation, or at least provide stronger evidence for acceleration mechanisms beyond first-order Fermi acceleration.

The second source studied, the Crab Nebula, is one of the most well-known astrophysical sources. In 1989, it became the first source detected at VHE energies (Weekes et al., 1989). It had been assumed that its emission was constant from X-rays to VHE γ-rays, but this was disproved in 2011 with the discovery of both short-term flares at MeV – GeV energies and a long-term decline at keV energies (Tavani et al., 2011; Abdo et al., 2011; Wilson-Hodge et al., 2011).

In March 2013, the first comprehensive set of VHE observations of the Crab Nebula simultaneous with a synchrotron flare were made. These observations did not detect any enhanced signal from the Nebula, challenging current theoretical models. An extensive analysis of more than a decade of archival VHE observations of the Crab was also performed. The data were searched for evidence of short-term flaring activity, but no significant detections were found. In light of the previous null result, which was obtained in optimum conditions to observe a flare, this is not surprising.

8.1 Future prospects

By 1989, the Whipple 10 m Telescope had already spent two decades observing the VHE γ-ray sky and only one source, the Crab Nebula, was unambiguously detected. Now, in 2014, the field is prospering, with ~ 150 sources detected in total by the various experiments that have contributed to this area of research. It is now known that astrophysical environments such as AGN, or PWNe in our own galaxy, are capable of accelerating particles up to relativistic energies. These particles in turn produce VHE emission which is detectable on the Earth by specially-designed telescopes such as VERITAS.

The Cherenkov Telescope Array

Almost 50 years since the first light of the Whipple 10 m Telescope, the design of imaging atmospheric Cherenkov telescopes is still evolving. The next generation of ground-based γ-ray observatory, the Cherenkov Telescope Array (CTA), aims for an increase in sensitivity of a factor of 10 in the currently accessible energy range (Acharya et al., 2013). It also seeks to extend the energy domain accessible with the IACT technique to well below 100 GeV and up to more than 300 TeV, constituting a vast advancement on what is currently achievable.

These performance goals will be achieved by using a combination of different sized telescopes; large ones for the lowest energies, medium ones for the core energy range, and many small ones to cover the highest energies. The telescopes will be deployed at two sites, one in the northern and one in the southern hemispheres, to provide full sky coverage. Each site will have of an array of telescopes of all three sizes, with a total of 50 − 100 telescopes per site. While construction will certainly still be in progress, it may be possible to begin partial operation of the CTA observatories as early as 2016.

At lower energies, the energy range of CTA will overlap with that of satellite detectors. *Fermi*-LAT observations will complement CTA down to MeV energies, and CTA will have a sensitivity to short-timescale phenomena that will be orders of magnitude better than that of the LAT.

Projects are also underway to develop air shower detectors with much improved sensitivity (e.g., HAWC). These will provide valuable complementary information, but will not be able to compete with the sensitivity of CTA.

The High Altitude Water Cherenkov Gamma-ray Observatory

The High Altitude Water Cherenkov Gamma-ray Observatory (HAWC) is currently under construction ~ 4.1 km above sea level in Mexico. It consists of an array of 300 water Cherenkov detectors spread over 22,000 m^2 (Abeysekara et al., 2012). The observatory is expected to enter full operations in late 2014 (Abeysekara et al., 2013).

It will observe the entire northern sky in the energy range ~ 50 GeV to ~ 100 TeV. While it will be less sensitive than current IACT observatories, it represents a factor of 15 improvement over its predecessor MILAGRO, and its large FoV of $\sim 2\,\Omega$ and near 100% duty cycle will allow for prompt follow-up of VHE γ-ray transient events. This is of particular importance for gamma-ray burst science, in which a fast follow-up is necessary to observe the prompt emission.

8.2 Conclusion

CTA will be key to understanding the VHE regime. Its increased sensitivity over current instruments will make it ideal for more in-depth studies of VHE sources. Sensitive observations of blazars, for example, are critical for characterising the high-energy peak of the SED, and discerning the dominant emission process (leptonic or hadronic). It should be capable of achieving the time-resolved spectra that would have been so useful for the studies of 1ES 1959+650 in this thesis. As models for particle acceleration and γ-ray emission become more complex, precise spectral and temporal measurements are necessary to constrain model parameters. Reliably detecting features such as minimum variability timescales can firmly constrain the size and location of the VHE emitting region. The reduced energy threshold of CTA will also enable the detection of more high-redshift sources, placing stronger constraints on models of the EBL.

Given the outcome of the statistical tests performed on the extended Crab Nebula data set, the significant detection of $\sim 10\%$ flux changes on short timescales appears challenging for current instruments. It is possible that CTA will be able to detect small ($< 10\%$) variations in the Crab Nebula flux on short timescales (hours), or place even stronger constraints on the level of VHE variability of the nebula during the high-energy synchrotron flares.

The next few years are critical for γ-ray astronomy. *Fermi* is approaching the end of its projected lifetime, and while it is anticipated that this will be extended, this is not guaranteed. As of now, there is no viable replacement mission. Therefore, current generation IACTs such as VERITAS must optimise their scientific endeavours while full multiwavelength spectral coverage is assured. In any case, the improved temporal and spectral information that will be available in the VHE regime with the advent of CTA, especially in conjunction with multiwavelength observations, will provide an exciting, deep insight into the high-energy universe.

8.3 Bibliography

Abdo, A. A., Ackermann, M., Ajello, M., et al., 2011; 'Gamma-ray flares from the Crab Nebula.' *Science (New York, N.Y.)*, vol. 331(6018):739

Abeysekara, A., Aguilar, J., Aguilar, S., et al., 2012; 'On the sensitivity of the HAWC observatory to gamma-ray bursts'. *Astroparticle Physics*, vol. 35(10):641

Abeysekara, A. U., Alfaro, R., Alvarez, C., et al., 2013; 'The Design, Calibration and Operation of HAWC: Contributions to ICRC 2013'. In 'Proceedings of the 33rd International Cosmic Ray Conference', Rio de Janeiro, Brazil

Acharya, B., Actis, M., Aghajani, T., et al., 2013; 'Introducing the CTA concept'. *Astroparticle Physics*, vol. 43:3

Tavani, M., Bulgarelli, A., Vittorini, V., et al., 2011; 'Discovery of powerful gamma-ray flares from the Crab Nebula.' *Science (New York, N.Y.)*, vol. 331(6018):736

Weekes, T. C., Cawley, M. F., Fegan, D. J., et al., 1989; 'Observation of TeV gamma rays from the Crab nebula using the atmospheric Cerenkov imaging technique'. *The Astrophysical Journal*, vol. 342:379

Wilson-Hodge, C. A., Cherry, M. L., Case, G. L., et al., 2011; 'WHEN A STANDARD CANDLE FLICKERS'. *The Astrophysical Journal Letters*, vol. 727(2):L40

Appendix A

Appendix

The tables that follow provide a summary of the X-ray observations of 1ES 1959+650 presented in Chapter 5. Observation IDs, start dates, durations, fluxes and spectral indices are provided for both RXTE and *Swift* data. Additionally, the deadtime correction factor is listed for the RXTE observations.

ObsID	Date	Start time	Dur (s)	DCOR	Flux$_{\text{2-10 keV}}$ ($\times 10^{-10}$ ergs cm^{-2} s^{-1})	Index
96387_12_01_00	2011-06-26	07:37:04	1456	1.0186	0.43 ± 0.008	2.61
96387_12_02_00	2011-06-28	08:12:00	2448	1.0184	0.27 ± 0.005	2.59
96387_12_04_00	2011-07-02	07:40:00	2464	1.0172	0.49 ± 0.009	2.65
96387_12_05_00	2011-07-04	08:24:16	2112	1.0169	0.45 ± 0.008	2.59
96387_12_07_00	2011-10-01	03:41:52	528	1.0223	0.91 ± 0.002	2.46
96387_12_08_00	2011-10-02	04:18:08	1072	1.0162	1.02 ± 0.018	2.67
96387_12_09_00	2011-10-16	02:10:56	1104	1.0175	1.20 ± 0.022	2.67
96387_12_11_00	2011-10-20	02:30:40	400	1.0182	1.15 ± 0.020	2.53
96387_12_12_00	2011-10-22	03:04:16	480	1.0181	1.14 ± 0.020	2.54
96387_12_13_00	2011-10-24	01:58:24	848	1.0174	1.44 ± 0.025	2.51
96387_12_14_00	2011-10-26	02:42:24	944	1.0164	1.14 ± 0.021	2.71
96387_12_15_00	2011-10-28	03:02:08	1136	1.0174	1.10 ± 0.019	2.55

Table A.1: Overview of RXTE observations of 1ES 1959+650 used in Chapter 5.

ObsID	Date	Start time	Livetime (s)	$\text{Flux}_{\text{2-10 keV}}$ ($\times 10^{-10}$ ergs cm^{-2} s^{-1})	Index
00035025013	2007-11-16	02:34:49	2163.35	1.01 ± 0.018	2.45
00035025014	2007-11-23	03:00:41	953.55	1.30 ± 0.023	2.23
00035025015	2007-11-23	04:34:41	1026.56	1.59 ± 0.027	2.21
00035025017	2008-10-05	03:31:16	3533.33	1.11 ± 0.019	2.43
00035025018	2008-10-13	00:49:44	843.02	1.42 ± 0.025	2.19
00035025019	2008-10-15	21:50:43	967.20	0.73 ± 0.013	2.45
00035025020	2008-10-16	01:26:16	925.29	0.79 ± 0.014	2.25
00035025021	2008-10-18	07:52:12	720.65	1.03 ± 0.017	2.14
00035025022	2008-10-27	17:11:59	994.86	0.79 ± 0.014	2.24
00035025023	2008-10-28	02:47:50	951.03	0.71 ± 0.013	2.31
00035025024	2008-10-30	14:16:38	1199.98	0.60 ± 0.012	2.38
00035025025	2008-10-31	04:44:53	955.03	0.62 ± 0.011	2.33
00035025026	2009-06-01	13:57:20	1559.53	0.64 ± 0.037	2.30
00035025028	2009-06-14	05:14:47	2976.46	0.88 ± 0.034	2.36
00035025030	2009-06-22	23:52:20	760.35	1.05 ± 0.111	2.40
00035025031	2009-06-25	12:58:26	577.07	0.83 ± 0.139	2.63
00035025032	2009-06-28	00:03:21	1223.67	1.68 ± 0.349	1.83
00035025033	2009-07-01	00:27:16	552.60	0.78 ± 0.083	2.53
00035025035	2009-07-08	07:22:14	458.65	1.14 ± 0.145	2.52
00035025036	2009-07-19	00:44:30	1021.18	0.78 ± 0.067	2.42
00035025037	2009-07-26	22:29:21	381.24	0.66 ± 0.093	2.64
00035025038	2009-08-02	08:19:28	247.78	0.72 ± 0.134	2.35
00035025039	2009-08-09	19:56:49	273.98	0.99 ± 0.167	2.34
00035025040	2009-08-16	14:13:51	1060.49	1.08 ± 0.061	2.29
00035025056	2010-07-27	00:03:21	74.92	0.77 ± 0.037	2.21

Table A.2: Overview of *Swift* observations of 1ES 1959+650 used in Chapter 5.